

Chapter 7

Rare and Semileptonic Decays

Christian W. Bauer, Gustavo Burdman, Aida X. El-Khadra, JoAnne Hewett, Gudrun Hiller, Michael Kirk, Jonathan Lewis, Heather E. Logan, Michael Luke, Ron Poling, Alex Smith, Ben Speakman, Kevin Stenson, Masa Tanaka, Andrzej Ziemiński

7.1 Rare Decays: Theory

7.1.1 Preliminaries

The Flavor-changing-neutral-current (FCNC) transitions, such as $b \rightarrow s$ and $b \rightarrow d$, arise only at the loop level in the Standard Model (SM). These decays provide tests of the detailed structure of the theory at the level of radiative corrections where Glashow-Iliopoulos-Maiani (GIM) cancellations are important, and are sensitive to CKM matrix elements: the flavor structure of a generic $b \rightarrow s$ amplitude T is $T = \sum_i \lambda_i T_i$, where $\lambda_i = V_{ib}V_{is}^*$ and the sum runs over all up-quark flavors $i = u, c, t$. Using CKM unitarity $\sum_i \lambda_i = 0$ and $\lambda_u \ll \lambda_t$ we obtain $T = \lambda_t(T_t - T_c)$.

Furthermore, in many extensions of the Standard Model, loop graphs with new particles (such as charged Higgses or supersymmetric partners) contribute at the same order as the SM contribution. Precision measurements of these rare processes therefore provides a complementary probe of new physics to that of direct collider searches. Finally, these rare decays are subject to both perturbative and non-perturbative QCD effects, which can be studied here.

The most interesting FCNC B decays at the Tevatron are $B \rightarrow X_s \gamma$, $B \rightarrow X_s \ell^+ \ell^-$, $B_{s,d} \rightarrow \ell^+ \ell^-$, and the corresponding exclusive modes for the first two. (A fourth decay, $B \rightarrow X_{s,d} \nu \bar{\nu}$, is theoretically cleaner, but because of the neutrinos in the final state is not likely to be accessible at a hadron collider.) Of these decays, the exclusive modes $B \rightarrow K^{(*)} \ell^+ \ell^-$ are likely to be the most important at the Tevatron in the near future: inclusive $B \rightarrow X_s \gamma$ is difficult to measure at a hadron collider, while the SM branching fraction for $B_s \rightarrow \mu^+ \mu^-$ is at the 10^{-9} level. Furthermore, as we shall discuss, the theoretical prediction for inclusive $B \rightarrow X_s \ell^+ \ell^-$ is poorly behaved in the large q^2 region, where it is easiest to measure. In this section, we focus on tests of the SM via these decays.

C_1	C_2	C_3	C_4	C_5	C_6	C_7^{eff}	C_9	C_{10}
-0.25	+1.11	+0.01	-0.03	+0.01	-0.03	-0.31	+4.34	-4.67

Table 7.1: SM values of the Wilson coefficients at NLO ($C_7^{\text{eff}} \equiv C_7 - C_5/3 - C_6$).

7.1.1.1 The effective Hamiltonian

Radiative corrections to the FCNC decay amplitudes contain terms of order $\alpha_s \ln m_W^2/m_b^2$, which are enhanced by the large logarithm of m_W/m_b and make perturbation theory poorly behaved. To make precision calculations, these terms must be summed to all orders. This is most conveniently performed using an effective field theory and the renormalization group, as discussed in Chapter 1.

The effective field theory for $b \rightarrow s$ transitions is thoroughly summarized in a review article by Buchalla *et al.*, [1]. Here we briefly outline the general features which are universal for the channels discussed in this chapter. The effective Hamiltonian is obtained by integrating out heavy degrees of freedom (the top quark and W^\pm bosons in the SM) from the full theory [2]:

$$\mathcal{H}_{\text{eff}} = -4 \frac{G_F}{\sqrt{2}} V_{ts}^* V_{tb} \sum_{i=1}^{10} C_i(\mu) O_i(\mu) \quad (7.1)$$

where μ is the renormalization scale, and the operators O_i are

$$\begin{aligned} O_1 &= (\bar{s}_{L\alpha} \gamma_\mu b_{L\alpha}) (\bar{c}_{L\beta} \gamma^\mu c_{L\beta}), & O_6 &= (\bar{s}_{L\alpha} \gamma_\mu b_{L\beta}) \sum_{q=u,d,s,c,b} (\bar{q}_{R\beta} \gamma^\mu q_{R\alpha}), \\ O_2 &= (\bar{s}_{L\alpha} \gamma_\mu b_{L\beta}) (\bar{c}_{L\beta} \gamma^\mu c_{L\alpha}), & O_7 &= \frac{e}{16\pi^2} m_b \bar{s}_{L\alpha} \sigma_{\mu\nu} b_{R\alpha} F^{\mu\nu}, \\ O_3 &= (\bar{s}_{L\alpha} \gamma_\mu b_{L\alpha}) \sum_{q=u,d,s,c,b} (\bar{q}_{L\beta} \gamma^\mu q_{L\beta}), & O_8 &= \frac{g}{16\pi^2} m_b \bar{s}_{L\alpha} T_{\alpha\beta}^a \sigma_{\mu\nu} b_{R\beta} G^{a\mu\nu}, \\ O_4 &= (\bar{s}_{L\alpha} \gamma_\mu b_{L\beta}) \sum_{q=u,d,s,c,b} (\bar{q}_{L\beta} \gamma^\mu q_{L\alpha}), & O_9 &= \frac{e^2}{16\pi^2} \bar{s}_{L\alpha} \gamma^\mu b_{L\alpha} \bar{\ell} \gamma_\mu \ell, \\ O_5 &= (\bar{s}_{L\alpha} \gamma_\mu b_{L\alpha}) \sum_{q=u,d,s,c,b} (\bar{q}_{R\beta} \gamma^\mu q_{R\beta}), & O_{10} &= \frac{e^2}{16\pi^2} \bar{s}_{L\alpha} \gamma^\mu b_{L\alpha} \bar{\ell} \gamma_\mu \gamma_5 \ell \end{aligned} \quad (7.2)$$

(note that these operators are not the same as the O_i 's for the $|\Delta B| = 1$ Hamiltonian discussed in Chapter 1). The subscripts L and R denote left and right-handed components, and we have neglected the strange quark mass $m_s \ll m_b$. The coefficient $C_i(m_W)$ are systematically calculable in perturbation theory, and the renormalization group equations are used to lower to renormalization scale to $\mu = m_b$. The renormalization group scaling is a significant effect, enhancing (for example) the $B \rightarrow X_s \gamma$ rate by a factor of ~ 2 . Details on the renormalization scale dependence, the renormalization group equations and analytical formulae can be found in [2]. The SM values at $\mu = 4.8$ GeV of the C_i at NLO are given in Table 7.1.

While C_7^{eff} measures the $bs\gamma$ coupling strength, an analogous correspondence can be made for C_{10} : comparing the charge assignments of lepton- Z -couplings $|(\bar{\ell}\ell Z|_V)/(\bar{\ell}\ell Z|_A)| = |1 - 4\sin^2 \Theta_W| \simeq 0.08$ shows that the Z -penguin contribution to C_9 (V) is suppressed with respect to C_{10} (A) and can be neglected as a first approximation: C_{10} probes the effective $\bar{s}_L Z b_L$ vertex modulo the box contribution [3].

Different FCNC decays are sensitive to different linear combinations of the C_i 's, and so each of the decays of interest provides independent information. The quark-level transition $b \rightarrow s\gamma$ is largely governed by O_7 , while $b \rightarrow s\ell^+\ell^-$ receives dominant contributions from O_7 , O_9 and O_{10} , and $B_s \rightarrow \ell^+\ell^-$ is primarily due to O_{10} . As discussed in the next section, the current measurement of $B \rightarrow X_s\gamma$ is in excellent agreement with theory, but this is only sensitive to the magnitude of the photon penguin C_7^{eff} . In contrast, $b \rightarrow s\ell^+\ell^-$ is sensitive to the sign of this coefficient, as well as to O_9 and O_{10} .

7.1.1.2 Inclusive vs. Exclusive Decays

The Wilson coefficients in Eq. (7.1) can be measured in either exclusive or inclusive decays of b flavored hadrons. The theoretical tools used to study exclusive and inclusive decays are very different. Experimental measurements of exclusive and inclusive decays are also faced with different challenges. Hence, it is convenient to consider them separately.

In inclusive decays one can avoid the theoretical difficulties associated with the physics of hadronization by using quark-hadron duality together with the operator product expansion (OPE) [4]. Quark-hadron duality allows us to relate inclusive decays of B hadrons into hadronic final states to decays into partons (see Section 5.3 of Chapter 1). Using an OPE it can be shown that the B decay is given by the corresponding parton-level decay. There are perturbative and nonperturbative corrections which must be taken into account. The leading nonperturbative corrections to this expression scale like $(\Lambda_{\text{QCD}}/m_b)^2$, which is of order a few percent. There are some caveats, both in the application of the OPE and in the assumption of quark-hadron duality.

The size of the corrections in the OPE typically grow as the final state phase space is restricted. If the phase space is restricted to too small a region the OPE breaks down entirely. This is an important consideration when experimental cuts are taken into account. A familiar example is the endpoint region above the $b \rightarrow c$ kinematic limit of the charged lepton spectrum in semileptonic $b \rightarrow u$ decay, which is important for measuring $|V_{ub}|$. In this region the standard OPE breaks down, and a class of leading twist operators in the OPE must be resummed to all orders. As we will discuss in Section (7.1.2.2), the OPE also breaks down in the high lepton q^2 region of $B \rightarrow X_s\ell^+\ell^-$, but in this region the twist expansion also break down.

The range of validity of quark-hadron duality and the size of the corrections which violate it are unknown, at present. There are theoretical reasons to believe that these corrections are small (and it has been suggested that duality violation is reflected in the asymptotic nature of the OPE) [5]. However, it has also been argued [6] that duality violations are much larger than commonly expected. As the data improve and more inclusive quantities are measured, the comparison between theory and experiment will provide an indication of the size of duality violations.

While theoretically appealing, inclusive rare decays are very difficult to measure, particularly in a hadronic environment. It is likely that they will be constructed by measuring a series of exclusive decays. Hence, it will be much easier to measure exclusive rare decays at the Tevatron.

In theoretical studies of exclusive decays, we must deal with nonperturbative QCD corrections to the quark-level process, as manifest in hadronization effects, for example. Lattice QCD is the only first principles tool for calculations of nonperturbative QCD effects. Unfortunately, results from lattice QCD calculations are incomplete, at present. Furthermore, numerical simulations based on lattice QCD are time consuming and expensive. The prospects for lattice QCD calculations of rare exclusive decays with small and controlled errors are excellent, as discussed in detail in Section 7.1.3.2. At present, however, we have to deal with hadronic uncertainties which result in a loss of sensitivity to the interesting short distance physics. It is therefore important to use a variety of theoretical strategies for calculations of these decays. We include model-independent approaches based on approximate symmetries as well as calculations which use a variety of different models in our discussion of exclusive decays in Section 7.1.3.

7.1.2 Inclusive Decays

7.1.2.1 $B \rightarrow X_s \gamma$

As discussed in Chapter 1, the theoretical description of the inclusive decay $B \rightarrow X_s \gamma$ is particularly clean as it is essentially given by the partonic weak decay $b \rightarrow s \gamma$ with small corrections of order $1/m_b^2$ [4] in the HQET expansion (although as the photon energy cut is raised above ~ 2 GeV the nonperturbative Fermi motion of the b quark becomes a significant effect [8]). Although it is a difficult task for hadron colliders to measure the photon energy spectrum governing the inclusive channel, it is discussed here for completeness.

The radiative decay is a magnetic dipole transition and is thus mediated by the operator O_7 . The corresponding Wilson coefficient $C_7(\mu)$ is evolved to the b -quark scale via the effective Hamiltonian of Eq. (7.1), with the basis for this decay consisting of the first eight operators in the expansion. The perturbative QCD corrections to the coefficients introduce large logarithms of the form $\alpha_s^n(\mu) \log^m(\mu/M_W)$, which are resummed order by order via the RGE. The next-to-leading order logarithmic QCD corrections have been computed and result in a much reduced dependence on the renormalization scale in the branching fraction compared to the leading-order result. The inclusion of the QCD corrections enhance the rate by a factor of ~ 2 , yielding agreement with the present experimental observation.

The higher-order QCD calculation to NLO precision involves several steps, requiring corrections to both the Wilson coefficients and the matrix element of O_7 in order to ensure a scheme independent result. For C_7 , the NLO computation entails the calculation of the $\mathcal{O}(\alpha_s)$ terms in the matching conditions [10], and the renormalization group evolution of $C_7(\mu)$ must be computed using the $\mathcal{O}(\alpha_s^2)$ anomalous dimension matrix [9]. For the matrix element, this includes the QCD bremsstrahlung corrections [11] $b \rightarrow s \gamma + g$, and the NLO virtual corrections [12]. Summing these contributions to the matrix element and expanding them around $\mu = m_b$, one arrives at the decay amplitude

$$\mathcal{M}(b \rightarrow s \gamma) = -\frac{4G_F V_{tb} V_{ts}^*}{\sqrt{2}} D \langle s \gamma | O_7(m_b) | b \rangle_{tree}, \quad (7.3)$$

with

$$D = C_7(\mu) + \frac{\alpha_s(m_b)}{4\pi} \left(C_i^{(0)eff}(\mu) \gamma_{i7}^{(0)} \log \frac{m_b}{\mu} + C_i^{(0)eff} r_i \right). \quad (7.4)$$

Here, the quantities $\gamma_{i7}^{(0)}$ are the entries of the effective leading order anomalous dimension matrix, the r_i are computed in [12], and the index i sums over the operator basis. The first term in Eq. (7.4), $C_7(\mu)$, must be computed at NLO precision, whereas it is consistent to use the leading order values of the other coefficients. The NLO expression for $C_7(\mu)$ is too complicated to present here, however, for completeness, we give the leading order result,

$$C_7^{(0)eff} = \eta^{16/23} C_7(M_W) + \frac{8}{3} \left(\eta^{14/23} - \eta^{16/23} \right) C_8(M_W) + C_2(M_W) \sum_{i=1}^8 h_i \eta^{a_i}, \quad (7.5)$$

where $\eta \equiv \alpha_s(M_W)/\alpha_s(\mu)$ and h_i, a_i are known numerical coefficients [1]. The form of this result will be relevant for our discussion of new physics contributions to $B \rightarrow X_s \gamma$, and clearly demonstrates the mixing between O_7 and the chromomagnetic dipole operator as well as the four quark operator.

There are also long-distance effects arising from emission of a gluon from a charm loop which are only suppressed by powers $\Lambda_{\text{QCD}} m_b/m_c^2$. The effects of these operators has been estimated to be small, contributing to the rate at the few percent level [13].

After employing an explicit lower cut on the photon energy in the gluon bremsstrahlung correction, the partial width is given by

$$\Gamma(B \rightarrow X_s \gamma) = \Gamma(b \rightarrow s \gamma) + \Gamma(b \rightarrow s \gamma + g)^{E_\gamma > (1-\delta)E_\gamma^{max}}, \quad (7.6)$$

where $E_\gamma^{max} = m_b/2$, and δ is a parameter defined by the condition that E_γ be above the experimental threshold. In addition, the 2-loop electroweak corrections have been computed [14] and are found to reduce the rate by $\sim 3.6\%$. The resulting branching fraction is then obtained by scaling the partial width for $B \rightarrow X_s \gamma$ to that for B semileptonic decay as the uncertainties due to the values of the CKM matrix elements and the m_b^5 dependence of the widths cancel in the ratio. The Standard Model prediction for the branching fraction is then found to be ¹

$$B(B \rightarrow X_s \gamma) = (3.28 \pm 0.30) \times 10^{-4}. \quad (7.7)$$

This is in good agreement with the observations by CLEO and ALEPH [16] which yield $B = (3.15 \pm 0.35 \pm 0.41) \times 10^{-4}$ and $B = (3.38 \pm 0.74 \pm 0.85) \times 10^{-4}$, respectively, with the 95% C.L. bound of $2 \times 10^{-4} < B(B \rightarrow X_s \gamma) < 4.5 \times 10^{-4}$. The inclusive decays are measured by analyzing the high energy region of the photon energy spectrum. A good theoretical description of the spectral shape is thus essential in order to perform a fit to the spectrum and extrapolate to the total decay rate. Higher order analyses of the spectrum within HQET have been performed in Ref. [17,18], where it is found that the shape of the spectrum is dominated by QCD dynamics and is insensitive to the presence of new physics. Measurement of the spectral moments of the photon energy distribution can also be used to determine the HQET parameters $\bar{\Lambda}$ and λ_1 with small theoretical uncertainty [19].

¹Ref. [15] argues that the running charm quark mass rather than the pole mass should be used in the two loop matrix element; this results in a slightly higher central value $(3.73 \pm 0.30) \times 10^{-4}$.

The CKM suppressed mode, $B \rightarrow X_d \gamma$, is computed in similar fashion with the substitution $s \rightarrow d$ in the above formulae and in the complete set of operators. There is also a slight modification of the 4-quark operators O_1 and O_2 to include the contributions from $b \rightarrow u$ [20] transitions. The NLO predicted branching fraction spans the range $6.0 \times 10^{-6} \leq B(B \rightarrow X_d \gamma) \leq 2.6 \times 10^{-5}$ with the main uncertainty arising from the imprecisely determined values of the CKM elements. This CKM suppressed channel populates the high energy region of the photon energy spectrum and hence $B \rightarrow X_s \gamma$ constitutes the main background source. Observation thus requires a veto of strange hadrons in the hadronic X_d system.

7.1.2.2 $B \rightarrow X_s \ell^+ \ell^-$

The decay $B \rightarrow X_s \ell^+ \ell^-$ is suppressed relative to $B \rightarrow X_s \gamma$ by an additional factor of the electromagnetic coupling constant $\alpha \simeq 1/137$, and has not yet been observed. The SM prediction for the branching fraction is

$$B(B \rightarrow X_s e^+ e^-) = (8.4 \pm 2.3) \cdot 10^{-6}, \quad B(B \rightarrow X_s \mu^+ \mu^-) = (5.7 \pm 1.2) \cdot 10^{-6} \quad (7.8)$$

which may be compared with the current experimental 90% C.L. upper bounds of $5.7 \cdot 10^{-5}$ and $5.8 \cdot 10^{-5}$ [64] respectively. Unlike $B \rightarrow X_s \gamma$, which is only sensitive to the magnitude of C_7^{eff} , this decay has the appeal of being sensitive to the signs and magnitudes of the Wilson coefficients C_7^{eff} , C_9 and C_{10} , which can all be affected by physics beyond the standard model. To extract the magnitudes and phases of all three Wilson coefficients, several different measurements must be performed. It has been shown in [21,22] that information from the dilepton invariant mass spectrum and the differential forward-backward asymmetry is sufficient to extract these parameters.

The decay amplitude

Since over most of phase space the differential rate is well approximated by the parton model, we first consider the parton level results. From the effective Hamiltonian (7.1) one easily obtains the parton level decay amplitude

$$\begin{aligned} \mathcal{A}(b \rightarrow s \ell^+ \ell^-) = & \frac{G_F \alpha}{\sqrt{2} \pi} V_{ts}^* V_{tb} \left[(C_9^{\text{eff}} - C_{10}) (\bar{s} \gamma_\mu L b) (\bar{\ell} \gamma^\mu L \ell) \right. \\ & + (C_9^{\text{eff}} + C_{10}) (\bar{s} \gamma_\mu L b) (\bar{\ell} \gamma^\mu R \ell) \\ & \left. - 2C_7^{\text{eff}} \left(\bar{s} i \sigma_{\mu\nu} \frac{q^\nu}{q^2} (m_s L + m_b R) b \right) (\bar{\ell} \gamma^\mu \ell) \right]. \quad (7.9) \end{aligned}$$

where C_7^{eff} is defined in Eq. (7.5). The additional operators O_9 and O_{10} receive contributions only from penguin and box diagrams in the matching and are therefore of order α . The coefficient C_9 contains a term proportional to $\alpha \log(\mu/m_W)$ at one loop, and so logarithms of the form $\alpha_s^{n+1} \log^n(m_b/m_W)$ must be summed to obtain leading logarithmic accuracy. Thus, the one loop matrix element of O_9 is required as well as the two loop running of C_9 . This amounts to the identification $C_9^{\text{eff}} \equiv C_9^{\text{eff}}(\hat{s})$, where

$$C_9^{\text{eff}}(\hat{s}) = C_9 \eta(\hat{s}) + Y(\hat{s}). \quad (7.10)$$

The one-loop matrix elements of the four-Fermi operators are represented by the function $Y(\hat{s})$, which in the NDR scheme is given by [2,23]

$$\begin{aligned} Y(\hat{s}) = & g(\hat{m}_c, \hat{s}) (3 C_1 + C_2 + 3 C_3 + C_4 + 3 C_5 + C_6) \\ & - \frac{1}{2} g(1, \hat{s}) (4 C_3 + 4 C_4 + 3 C_5 + C_6) - \frac{1}{2} g(0, \hat{s}) (C_3 + 3 C_4) \\ & + \frac{2}{9} (3 C_3 + C_4 + 3 C_5 + C_6), \end{aligned} \quad (7.11)$$

where

$$\begin{aligned} g(z, \hat{s}) = & -\frac{8}{9} \ln\left(\frac{m_b}{\mu}\right) - \frac{8}{9} \ln z + \frac{8}{27} + \frac{4}{9} y - \frac{2}{9} (2+y) \sqrt{|1-y|} \\ & \times \left[\Theta(1-y) \left(\ln \frac{1+\sqrt{1-y}}{1-\sqrt{1-y}} - i\pi \right) + \Theta(y-1) 2 \arctan \frac{1}{\sqrt{y-1}} \right], \end{aligned} \quad (7.12)$$

$$g(0, \hat{s}) = \frac{8}{27} - \frac{8}{9} \ln\left(\frac{m_b}{\mu}\right) - \frac{4}{9} \ln \hat{s} + \frac{4}{9} i\pi, \quad (7.13)$$

with $y = 4z^2/\hat{s}$. The one loop matrix element of O_9 as a function of the dilepton invariant mass is written as

$$\eta(\hat{s}) = 1 + \frac{\alpha_s(\mu)}{\pi} \omega(\hat{s}), \quad (7.14)$$

where

$$\begin{aligned} \omega(\hat{s}) = & -\frac{2}{9} \pi^2 - \frac{4}{3} \text{Li}_2(\hat{s}) - \frac{2}{3} \ln \hat{s} \ln(1-\hat{s}) - \frac{5+4\hat{s}}{3(1+2\hat{s})} \ln(1-\hat{s}) \\ & - \frac{2\hat{s}(1+\hat{s})(1-2\hat{s})}{3(1-\hat{s})^2(1+2\hat{s})} \ln \hat{s} + \frac{5+9\hat{s}-6\hat{s}^2}{6(1-\hat{s})(1+2\hat{s})} \end{aligned} \quad (7.15)$$

and we have neglected the strange quark mass.

It is convenient to normalize the rate of $b \rightarrow s\ell^+\ell^-$ to that for semileptonic $b \rightarrow c\ell\bar{\nu}$ decay

$$d\mathcal{B}(B \rightarrow X_s \ell^+ \ell^-) = \mathcal{B}_{sl} \frac{d\Gamma(B \rightarrow X_s \ell^+ \ell^-)}{\Gamma(B \rightarrow X_c \ell \nu_\ell)}. \quad (7.16)$$

This introduces the normalization constant

$$\mathcal{B}_0 = \mathcal{B}_{sl} \frac{3\alpha^2}{16\pi^2} \frac{|V_{ts}^* V_{tb}|^2}{|V_{cb}|^2} \frac{1}{f(\hat{m}_c) + [\alpha_s(m_b)/\pi] A_0(\hat{m}_c)}. \quad (7.17)$$

In this expression $f(\hat{m}_c)$ is the well known phase space factor for the parton decay rate $b \rightarrow c\ell\bar{\nu}$

$$f(\hat{m}_c) = 1 - 8\hat{m}_c^2 + 8\hat{m}_c^6 - \hat{m}_c^8 - 24\hat{m}_c^4 \log \hat{m}_c, \quad (7.18)$$

and $A_0(\hat{m}_c)$ is the $\mathcal{O}(\alpha_s)$ QCD correction to the semileptonic $b \rightarrow c$ decay rate [24].

Parton model differential decay rate and forward-backward asymmetry

The forward-backward asymmetry in inclusive $b \rightarrow s\ell^+\ell^-$ has been studied in detail [21]. From the amplitude of the decay $b \rightarrow s\ell^+\ell^-$ (7.9) the dilepton invariant mass distribution in the parton model can easily be calculated

$$\begin{aligned} \frac{d\mathcal{B}}{d\hat{s}} = \frac{4}{3} \mathcal{B}_0 \left[(1 - \hat{s})^2 (1 + \hat{s}) \left(|C_9^{\text{eff}}|^2 + C_{10}^2 \right) \right. \\ \left. + 2(1 - \hat{s})^2 (2 + \hat{s}) \frac{|C_7^{\text{eff}}|^2}{\hat{s}} + 6(1 - \hat{s})^2 \text{Re} \left(C_9^{\text{eff}} \right) C_7^{\text{eff}} \right]. \end{aligned} \quad (7.19)$$

A plot of this distribution is shown by the solid line in Figure 7.1. The divergence at $\hat{s} = 0$ is due to the intermediate photon going on shell and is a well known feature of this decay. In this limit the differential decay rate reduces to the $B \rightarrow s\gamma$ rate with an on-shell photon in the final state, convoluted with the fragmentation function which describes the probability for the photon to fragment into a lepton pair.

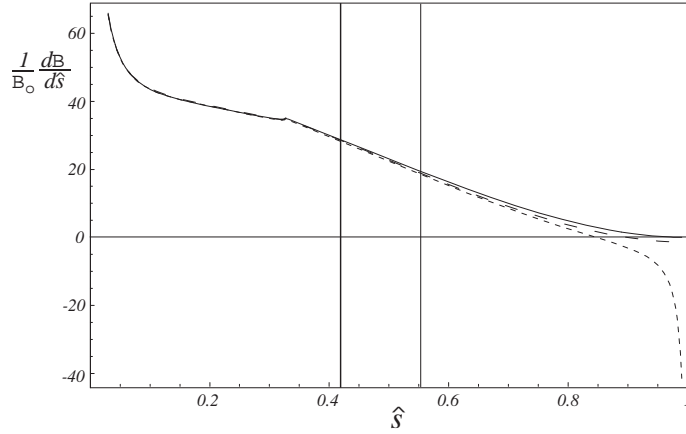


Figure 7.1: The differential decay spectrum $\frac{1}{\mathcal{B}_0} \frac{d\mathcal{B}}{d\hat{s}}$ for the decay $B \rightarrow X_s \ell^+ \ell^-$. The solid line shows the free quark prediction, the long-dashed line includes the $\mathcal{O}(\Lambda/m_b^2)$ corrections and the short-dashed line contains all corrections up to $\mathcal{O}(\Lambda/m_b^3)$.

The differential forward-backward asymmetry is defined by

$$\frac{d\mathcal{A}}{d\hat{s}} = \int_0^1 dz \frac{d\mathcal{B}}{dx d\hat{s}} - \int_{-1}^0 dx \frac{d\mathcal{B}}{dx d\hat{s}} \quad (7.20)$$

where

$$x = \cos\theta = \frac{\hat{u}}{\hat{u}(\hat{s}, \hat{m}_s)} \quad (7.21)$$

parameterizes the angle between the b quark and the ℓ^+ in the dilepton CM frame. An experimentally more useful quantity is the normalized FB asymmetry defined by

$$\frac{d\bar{\mathcal{A}}}{d\hat{s}} = \frac{d\mathcal{A}}{d\hat{s}} \bigg/ \frac{d\mathcal{B}}{d\hat{s}}. \quad (7.22)$$

In the parton model the differential forward-backward asymmetry is given by

$$\frac{d\bar{A}}{d\hat{s}} = -4\mathcal{B}_0(1-\hat{s})^2 \left[\hat{s} \operatorname{Re} \left(C_9^{\text{eff}}(\hat{s}) \right) C_{10} + 2C_{10}C_7^{\text{eff}} \right], \quad (7.23)$$

which is shown by the solid line in Figure 7.2.

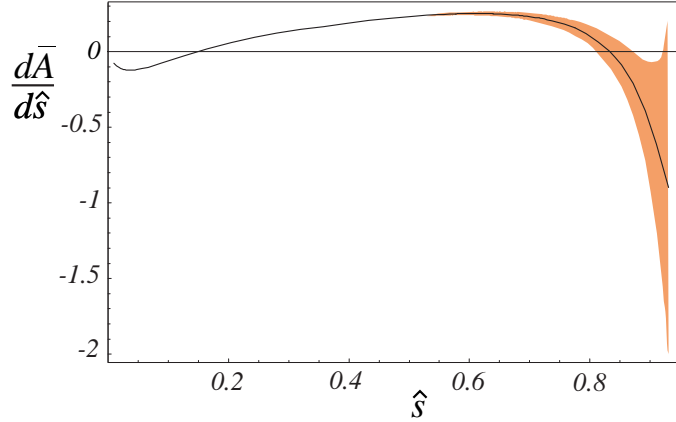


Figure 7.2: The normalized forward backward asymmetry. The three curves show the mean value and the 1σ uncertainty of the forward backward asymmetry.

Charmonium resonances

Both the dilepton invariant mass spectrum and the differential forward-backward asymmetry contain a cusp at the threshold of $c\bar{c}$ pair production. For such values of \hat{s} long distance contributions from tree level processes $B \rightarrow B^{(*)}\psi^{(\prime)}$, followed by $\psi^{(\prime)} \rightarrow \ell^+\ell^-$, are important, which can not be calculated perturbatively. The location of the first two $c\bar{c}$ resonances are indicated in Figs. 7.1 and 7.2 by the two vertical lines.

Since the $c\bar{c}$ resonance contributions cannot be calculated model independently, suitable cuts on the dilepton invariant mass are conventionally applied to eliminate these resonance contributions. Such cuts naturally divide the available phase space into two separate regions: a low \hat{s} region for $s \leq M_\psi^2 - \delta$ and a high \hat{s} region for $s \geq M_{\psi'}^2 + \delta'$, where $\delta^{(\prime)}$ depends on the exact values of the experimental cuts. The region of phase space below the ψ resonance is contaminated by background from sequential B decays. This background can only be suppressed if the inclusive process is measured by summing over a large number of individually reconstructed final states. In the region above the ψ' resonance, there is almost no background from other B decays, making the measurement much easier. It is the latter region of phase space that is accessible to experiments at the Tevatron.

Power corrections to the dilepton invariant mass spectrum and the forward-backward asymmetry

Nonperturbative physics can be parameterized by matrix elements of higher dimensional operators. This is done by performing an OPE as described in Chapter 1. The leading

corrections arise at order $\mathcal{O}(\Lambda_{QCD}/m_b)^2$ and can be parameterized by the matrix elements of two dimension five operators. Both matrix elements, λ_1 and λ_2 have been measured, albeit with large uncertainties for λ_1 . At order $\mathcal{O}(\Lambda_{QCD}/m_b)^3$ there are seven operators contributing, with none of the matrix elements known. Calculating the contributions from these dimension six operators therefore do not improve the theoretical accuracy, but can be used to investigate the convergence of the OPE and estimate theoretical uncertainties. The contributions of the dimension five operators to the differential decay rate and the forward backward asymmetry were calculated in Ref. [25] and the calculation including all power corrections up to order Λ_{QCD}^3/m_b^3 is presented in Ref. [26].

The effects of these corrections on the differential decay rate are shown in Figure 7.1 by the long and short dashed lines, respectively. It is obvious from Figure 7.1 that the effect of higher dimensional operators is negligible below the ψ resonance, whereas it is large in the large \hat{s} region. This can also be seen by calculating the branching ratio with an upper cut on the dilepton invariant mass 100 MeV below m_ψ , $\hat{s} = 0.35$. Including a cut $\hat{s} > 0.01$ to eliminate the fragmentation divergence at low q^2 the expansion in $1/m_b$ yields

$$\int_{0.01}^{0.35} d\hat{s} \frac{d\mathcal{B}}{d\hat{s}} = 22.0 \left[1 + 0.5 \frac{\lambda_1}{m_b^2} + 1.2 \left(\frac{\lambda_2}{m_b^2} - \frac{\rho_2}{m_b^3} \right) - 3.7 \frac{\rho_1}{m_b^3} \right] \quad (7.24)$$

where the ρ_i 's and f_1 are unknown matrix elements of order Λ_{QCD}^3 , and we have neglected contributions of a comparable size coming from T-products, which may be absorbed into a redefinition of λ_1 and λ_2 . All numerical coefficients are of order unity and the OPE is therefore converging well. In the region above the resonances the situation looks quite different. Imposing a lower cut 100 MeV above the ψ' resonance, $\hat{s} = 0.59$, the partially integrated branching ratio is

$$\int_{0.59}^1 d\hat{s} \frac{d\mathcal{B}}{d\hat{s}} = 3.8 \left[1 + 0.5 \frac{\lambda_1}{m_b^2} - 35.4 \left(\frac{\lambda_2}{m_b^2} - \frac{\rho_2}{m_b^3} \right) + 161.8 \frac{\rho_1}{m_b^3} + 147.4 \frac{f_1}{m_b^3} \right]. \quad (7.25)$$

From this expression it is clear that the convergence of the OPE is very poor and the branching ratio above the ψ' resonance can not be calculated well.

Higher dimensional operators can also be included for the forward-backward asymmetry. This leads to

$$\begin{aligned} \frac{d\mathcal{A}}{d\hat{s}} = & C_7^{\text{eff}} C_{10} \left[-8(1-\hat{s})^2 - \frac{4(3+2\hat{s}+3\hat{s}^2)\lambda_1}{3m_b^2} + \frac{4(7+10\hat{s}-9\hat{s}^2)\lambda_2}{m_b^2} \right. \\ & \left. + \frac{4(5+2\hat{s}+\hat{s}^2)\rho_1}{3m_b^3} - \frac{4(7+10\hat{s}-9\hat{s}^2)\rho_2}{m_b^3} \right] \\ & + C_9^{\text{eff}}(\hat{s}) C_{10} \left[-4\hat{s}(1-\hat{s})^2 - \frac{2\hat{s}(3+2\hat{s}+3\hat{s}^2)\lambda_1}{3m_b^2} + \frac{2\hat{s}(9+14\hat{s}-15\hat{s}^2)\lambda_2}{m_b^2} \right. \\ & \left. - \frac{2\hat{s}(1+2\hat{s}+5\hat{s}^2)\rho_1}{3m_b^3} - \frac{2\hat{s}(1+6\hat{s}-15\hat{s}^2)\rho_2}{m_b^3} \right] \end{aligned} \quad (7.26)$$

It is clear from this expression that the third order terms do not have abnormally large coefficients, and therefore introduce only small variations relative to the second order expressions. The normalized forward-backward asymmetry, however, inherits the poor behavior

of the differential branching ratio in the endpoint region $\hat{s} \rightarrow 1$. The normalized asymmetry is shown in Figure 7.2, with the shaded region representing the uncertainties due to $(\Lambda_{QCD}/m_b)^3$ terms. From this Figure it is clear that the nonperturbative uncertainties on the differential asymmetry are small below the ψ resonance, whereas they are large above the ψ' .

7.1.3 Exclusive Decays

The Wilson coefficients defined in Section 7.1.1.1 contain the short distance information that allows us to test the one loop structure of the standard model. The exclusive decays we will consider in this section can be used to determine these coefficients. However, these decays also depend on the hadronic matrix elements of the operators in Eqs. (7.2), which describe the transition from the initial state b flavored hadron to the final state hadron. These hadronic matrix elements are dominated by nonperturbative QCD effects. They are calculable in principle from lattice QCD, the only *ab initio* framework available for quantitative calculations of nonperturbative QCD.

At present, lattice QCD calculations of these processes are incomplete. This results in important uncertainties in theoretical predictions of exclusive rare decays, with a corresponding loss of sensitivity to the interesting short distance physics. We therefore need a variety of other theoretical tools at our disposal. These include model independent approaches based on approximate symmetries, such as heavy quark and chiral symmetry, and model-dependent approaches based on phenomenologically motivated models. While not rigorous, model calculations can serve to guide lattice calculations and provide a simple framework for studying these processes.

The rest of this section is organized as follows. After introducing the matrix elements and form factor parameterizations in Section 7.1.3.1, we discuss results and prospects from lattice QCD in Section 7.1.3.2. Rare semileptonic decays are discussed in Section 7.1.3.3 which describes results and constraints from model independent approaches first, followed by a summary of model-dependent results. Section 7.1.3.4 gives a discussion of the status of theoretical predictions for exclusive radiative decays. Finally, Section 7.1.3.5 discusses results for $B_{s,d} \rightarrow l^+l^-$ decays.

7.1.3.1 Hadronic Matrix Elements and Form Factors

The hadronic matrix elements can be parametrized in terms of form factors which are functions of the momentum transfer between the initial and final state hadrons.

For the $B \rightarrow K \ell^+ \ell^-$ decay the hadronic matrix elements of the operators O_7 , O_9 and O_{10} (which were defined in Eqs. (7.2)) are parametrized as

$$\langle K(k) | \bar{s} \sigma_{\mu\nu} q^\nu b | B(p) \rangle = i \frac{f_T}{m_B + m_K} \left\{ (p+k)_\mu q^2 - q_\mu (m_B^2 - m_K^2) \right\}, \quad (7.27)$$

$$\langle K(k) | \bar{s} \gamma_\mu b | B(p) \rangle = f_+ (p+k)_\mu + f_- q_\mu, \quad (7.28)$$

with $f_T(q^2)$ and $f_{\pm}(q^2)$ unknown functions of $q^2 = (p - k)^2 = m_{\ell^+\ell^-}^2$. In the $SU(3)$ limit f_{\pm} in (7.28) are the same as the form factors entering in the semileptonic decay $B \rightarrow \pi\ell\nu$.

For the vector meson mode, $B \rightarrow K^*\ell^+\ell^-$, we have the ‘‘semileptonic’’ matrix element

$$\begin{aligned} \langle K^*(k, \epsilon) | \bar{s}_L \gamma_\mu b_L | B(p) \rangle = \frac{1}{2} \left\{ i g \epsilon_{\mu\nu\alpha\beta} \epsilon^{*\nu} (p+k)^\alpha (p-k)^\beta - f \epsilon_\mu^* \right. \\ \left. - a_+ (\epsilon^* \cdot p) (p+k)_\mu - a_- (\epsilon^* \cdot p) (p-k)_\mu \right\}, \end{aligned} \quad (7.29)$$

where ϵ_μ is the K^* polarization four-vector. The form factors defined in (7.29) can be identified, in the $SU(3)$ limit, with those appearing in the semileptonic transition $B \rightarrow \rho\ell\nu$. The matrix element of the penguin operator takes the form

$$\begin{aligned} \langle K^*(k, \epsilon) | \bar{s}_L \sigma_{\mu\nu} q^\nu b_R | B(p) \rangle = i \epsilon_{\mu\nu\alpha\beta} \epsilon^{*\nu} p^\alpha k^\beta 2T_1 \\ + T_2 \left\{ \epsilon_\mu^* (m_B^2 - m_{K^*}^2) - (\epsilon \cdot p) (p+k)_\mu \right\} \\ + T_3 (\epsilon \cdot p) \left\{ q_\mu - \frac{q^2}{m_B^2 - m_{K^*}^2} (p+k)_\mu \right\}, \end{aligned} \quad (7.30)$$

Radiative decays receive a contribution from the local operator O_7 – also called the magnetic dipole operator – and its associated Wilson coefficient. This is also sometimes called the short distance contribution, since another contribution comes from non-local operators. These non-local operators are due to (i) the process $B \rightarrow VV^*$ with the subsequent conversion of the neutral vector meson V^* to a real photon, and (ii) weak annihilation and W exchange diagrams with subsequent γ radiation. Contributions from non-local operators are sometimes also called long distance contributions.

The hadronic matrix element of the magnetic dipole operator for the $B \rightarrow V\gamma$ decay, where V represents a vector meson, is generally written in terms of three form factors, with

$$\begin{aligned} \langle V(p, \epsilon) | \bar{s} \sigma_{\mu\nu} q^\nu (1 + \gamma_5) b | B(p_B) \rangle = 2i \epsilon_{\mu\nu\rho\sigma} \epsilon^{*\nu} p_B^\rho p^\sigma T_1(q^2) \\ + \left[\epsilon_\mu^* (m_B^2 - m_V^2) - (\epsilon^* \cdot q) (p_B + p)_\mu \right] T_2(q^2) \\ + (\epsilon^* \cdot q) \left[q_\mu - \frac{q^2}{m_B^2 - m_V^2} (p_B + p)_\mu \right] T_3(q^2), \end{aligned} \quad (7.31)$$

where ϵ^* represents the polarization vector of the vector meson, and q corresponds to the momentum of the outgoing photon. This simplifies for the case of an on-shell photon, where the coefficient of T_3 vanishes and $T_2(0) = -iT_1(0)$. Hence in the physical cases of interest here, the decay width can be expressed in terms of a single form factor,

$$\Gamma(B \rightarrow V + \gamma) = \frac{\alpha G_F^2}{32\pi^4} |V_{tb} V_{ts}^*|^2 (m_b^2 + m_s^2) m_B^3 \left(1 - \frac{m_V^2}{m_B^2} \right)^3 |C_7^{(0)eff}(m_b)|^2 |T_1^{B \rightarrow V}(q^2 = 0)|^2, \quad (7.32)$$

and the branching fraction is computed by scaling to the semileptonic rate as usual.

7.1.3.2 Lattice QCD

Lattice QCD methods are well suited for theoretical calculations of the hadronic matrix elements (and form factors) which describe rare decays. However, because of the lack of experimental information on rare semileptonic decays (such as $B \rightarrow K\ell^+\ell^-$), they have not been studied on the lattice to date. Results from lattice calculations of rare radiative decays do exist, and are discussed in more detail in Section 7.1.3.4.

The hadronic matrix elements which describe rare semileptonic decays (as shown in Eqs. (7.28–7.30)) are similar to the matrix elements for semileptonic decays, such as $B \rightarrow \pi\ell\bar{\nu}$. These have been studied extensively using lattice methods. We can use the existing results from lattice calculations of $B \rightarrow \pi\ell\bar{\nu}$ to discuss the prospects for lattice calculations of rare decays, like $B \rightarrow K^{(*)}\ell^+\ell^-$.

Current lattice calculations of the $B \rightarrow \pi\ell\bar{\nu}$ form factors are accurate to about 15–20% [27]. It would be relatively straightforward to perform a lattice QCD calculation of the form factors for $B \rightarrow K\ell^+\ell^-$ with a similar accuracy using current technology. The quoted uncertainty includes all systematic errors except for the quenched approximation – unquenched results do not yet exist for these decays. From unquenched calculations of other quantities, we can estimate the expected size of the effect to be in the range of 10–15%. Apart from the quenched approximation, the most important errors in lattice QCD calculations are due to statistics (from the Monte-Carlo integration), the chiral extrapolation, the lattice spacing, and perturbation theory (see Section 5.3 of Chapter 1 for a detailed discussion of how these errors arise).

Lattice QCD calculations are in principle improvable to arbitrary precision. In practice, the accuracy of lattice calculations depends on the computational effort and available technology. Numerical simulations based on lattice QCD are time consuming and computationally expensive. In the following, we shall discuss the prospects for reducing the total uncertainty in lattice QCD calculations to a few percent. We assume that there will be reasonable growth in the computational resources available for these lattice QCD calculations.

Improving the statistical and chiral extrapolation errors is straightforward; it just requires more computer time. This is within reach of the computational resources which should become available to lattice QCD calculations within the next few years.

Lattice spacing errors can be reduced by explicitly reducing the lattice spacing ($a \rightarrow 0$) used in the calculations. However, the computational cost of a lattice calculation scales like $1/a^{6-10}$. In general, lattice spacing errors are proportional to terms which grow like $(a\Lambda)^n$ where Λ is the typical momentum scale of the process in question. Typical lattice spacings used in numerical simulations are in the range $0.05 \text{ fm} \lesssim a \lesssim 0.2 \text{ fm}$, so that $a\Lambda \ll 1$ for momenta of order Λ_{QCD} . The power n (and hence the size of lattice spacing errors) depends on the discretization used in the calculation. With the (improved) lattice actions currently in use, $n = 2$. With highly improved lattice actions we can increase the power to $n = 4$. The situation is a bit more complicated in the presence of heavy quarks. However, as discussed in detail in Section 1.5.3, the lattice spacing errors associated with heavy quarks can be as easily controlled as the errors associated with the light degrees of freedom. In summary, we can keep lattice spacing errors under control at the few percent

(or less) level, by using highly improved actions in simulations at relatively coarse lattice spacings. The big advantage of this strategy is its low computational cost. It is therefore also the best strategy for realistic unquenched calculations.

There is a further restriction for semileptonic decays which arises from the need to control lattice spacing errors. The hadronic matrix elements (and form factors) for semileptonic decays are functions of the daughter recoil momentum. Since lattice spacing errors increase with increasing recoil momentum, the momentum range accessible to lattice QCD calculations is limited. At present, in order to keep lattice errors under control, most calculations impose an upper momentum cut of

$$\mathbf{p}_{\text{recoil}} < 1 \text{ GeV}. \quad (7.33)$$

For decays like $B \rightarrow D\ell\bar{\nu}$ this is not a problem, as the allowed recoil range is also small. However, for decays of B mesons into light hadrons we can obtain the matrix elements and form factors only over part of the allowed range. In particular, the high recoil region, $\mathbf{p}_{\text{recoil}} \propto m_B/2$, which corresponds to q^2 small or near zero, is not directly accessible to lattice QCD calculations.

A remedy used in early calculations is to extrapolate the form factors from the high q^2 region to low q^2 assuming a functional form for the shape of the form factors. This procedure introduces a model dependent systematic error into the calculation which can't be quantified. This was an acceptable compromise for early lattice calculations intended to establish the method. However, it is certainly undesirable for first principles calculations designed to test the standard model.

If there is significant overlap between the recoil momentum ranges accessible in lattice QCD calculations and experimental measurements, then we can avoid model dependent extrapolations and limit the comparison between theory and experiment to the common recoil momentum range. Indeed, this appears to be the case for $B \rightarrow \pi\ell\bar{\nu}$, and will most likely also be true for rare semileptonic decays such as $B \rightarrow K\ell^+\ell^-$. However, as discussed in the following section, the high recoil region is of particular phenomenological interest in $B \rightarrow K^{(*)}\ell^+\ell^-$ decays.

It is possible to increase the recoil momentum range accessible to lattice calculations by using highly improved actions, especially in combination with asymmetric lattices [28]. However, lattice calculations of radiative decays such as $B \rightarrow K^*\gamma$ remain problematic. With a real photon, the two body decay takes place at maximum recoil or $q^2 = 0$. If we want to avoid model-dependent extrapolations, we will need to develop better techniques for dealing with this high recoil physics.

7.1.3.3 $B \rightarrow K^*\ell^+\ell^-$ and $B \rightarrow K\ell^+\ell^-$

In the following, we review results for calculations of the form factors in Eqs. (7.28–7.30) from different theoretical approaches. The prospects for lattice QCD results were already discussed in the previous section. We first present the constraints derived from heavy quark symmetry (HQS), followed by results from SU(3) symmetry and finally from the large energy limit (LEL).

We then review results obtained from calculations using phenomenological models. A vast variety of models are available for these calculations. Here, we present the relevant features of current models. Although predictions from different models still disagree with each other, the situation has greatly improved since the experimental observation of exclusive B decays to light hadrons.

Predictions from HQET

As discussed in Chapter 1, the Dirac structure of b quarks simplifies in the Heavy Quark Limit, $m_b \gg \Lambda_{\text{QCD}}$, allowing relations between different form factors to be derived. For example, in the rest frame of the heavy quark, $v^\mu = (1, \vec{0})$, the heavy quark field obeys $\gamma_0 h_0 = h_0$, and so

$$\bar{h}_b i \sigma_{0i} h_b = \bar{h}_b \gamma_i h_b, \quad \bar{h}_b i \sigma_{0i} \gamma_5 h_b = -\bar{h}_b \gamma_i \gamma_5 h_b. \quad (7.34)$$

By making use of (7.34) we can now obtain relations among the form factors in (7.27) and (7.28). They are [29]

$$f_T(q^2) = -\frac{m_B + m_K}{2m_B} (f_+(q^2) - f_-(q^2)), \quad (7.35)$$

$$T_1(q^2) = \frac{f(q^2) - 2(q \cdot p)g(q^2)}{2m_B}, \quad (7.36)$$

$$T_2(q^2) = T_1(q^2) - \frac{f(q^2) - 2(m_B^2 + k \cdot p)g(q^2)}{2m_B} \left(\frac{q^2}{m_B^2 - m_{K^*}^2} \right), \quad (7.37)$$

$$T_3(q^2) = \frac{m_B^2 - m_{K^*}^2}{2m_B} \{a_+(q^2) - a_-(q^2) + 2g(q^2)\}. \quad (7.38)$$

In terms of the symmetries of the HQET, Eqs. (7.35–7.38) are a result of the Heavy Quark *Spin* Symmetry (HQSS) that arises in the heavy quark limit due to the decoupling of the spin of the heavy quark [30]. This is a very good symmetry when considering B decays, a measure of which is for instance the quantity

$$\frac{m_{B^*} - m_B}{m_B} \simeq 0.009 \sim \left(\frac{0.45}{4.8} \right)^2 \quad (7.39)$$

which is in agreement with the HQET prediction of $O(\Lambda_{\text{QCD}}^2/m_b^2)$. Thus the relations (7.35–7.38), which are valid over the entire physical region [31], will receive only small corrections. They allow us to express all the hadronic matrix elements entering in $B \rightarrow K^{(*)} \ell^+ \ell^-$ processes, in terms of the “semileptonic” form factors f , g and a_\pm .

Furthermore, there is an additional $SU(2)_F$ flavor symmetry in the heavy quark limit, leading to relations among form factors occurring in the decays of charm and bottom hadrons [29,30]. For instance in $H \rightarrow \pi \ell \nu$ one obtains

$$(f_+ - f_-)^{B \rightarrow \pi} = C_{BD} \sqrt{\frac{m_B}{m_D}} (f_+ - f_-)^{D \rightarrow \pi}, \quad (7.40)$$

$$(f_+ + f_-)^{B \rightarrow \pi} = C_{BD} \sqrt{\frac{m_D}{m_B}} (f_+ + f_-)^{D \rightarrow \pi}, \quad (7.41)$$

where $C_{BD} = (\alpha_s(m_B)/\alpha_s(m_D))^{-6/25}$ is a leading logarithmic QCD correction to the heavy quark currents [32]. Similar scaling relations are obtained for $H \rightarrow \rho\ell\nu$,

$$f^{B \rightarrow \rho} = C_{BD} \sqrt{\frac{m_B}{m_D}} f^{D \rightarrow \rho}, \quad (7.42)$$

$$g^{B \rightarrow \rho} = C_{BD} \sqrt{\frac{m_D}{m_B}} g^{D \rightarrow \rho}, \quad (7.43)$$

$$(a_+ - a_-)^{B \rightarrow \rho} = C_{BD} \sqrt{\frac{m_D}{m_B}} (a_+ - a_-)^{D \rightarrow \rho}. \quad (7.44)$$

In the above relations the form factors must be evaluated at the same value of the hadronic energy recoil $v \cdot k$, not the same value of q^2 . The semileptonic D decays have a maximum recoil energy of about 1 GeV, whereas B decays go up to $\simeq m_B/2$. Thus the use of data from D decays requires an extrapolation from the low to the high recoil regions of phase space, for which the $v \cdot k$ dependence of the form factors must be assumed. In addition, the relations (7.40-7.44) are valid in the leading order in the HQET and will receive corrections of the order of $\bar{\Lambda}/2m_c \simeq 0.15$, with $\bar{\Lambda}$ the effective mass of the light degrees of freedom. Then, the corrections to the flavor symmetry are likely to be larger than those to the spin symmetry. For instance, in the $H \rightarrow \pi\ell\nu$, corrections as large as 20% – 30% are possible [33]. On the other hand, it was shown in Ref. [34] that the $B \rightarrow K^*\gamma$ rate can be well reproduced by using both the spin and the flavor symmetries in HQET to relate the $D \rightarrow K^*\ell\nu$ form factors to $T_1(0)$ determining the radiative branching fraction, with the additional assumption of a monopole q^2 dependence for the form factors f and g all the way from $q^2 = 16.5 \text{ GeV}^2$ to $q^2 = 0$.

Other Theoretical Approaches

SU(3):

A necessary ingredient in the application of the HQSS relations (7.35-7.38) to predictions for $B \rightarrow K^{(*)}\ell^+\ell^-$ making use of the semileptonic form factors in $B \rightarrow (\pi\rho)\ell\nu$ is the assumption of well-behaved $SU(3)$ symmetry relations. Intuitively, and since the form factors are determined by the strong interactions, we expect that at very high recoil energies $SU(3)$ is a very good approximation. For rare B decays, where most of the events occur in this region of phase space, we should be confident that $SU(3)$ corrections are small. However, it is difficult to make a quantitative statement about the size of the $SU(3)$ breaking in a completely model independent way. For instance, in the constituent quark model picture, a relevant quantity parameterizing $SU(3)$ breaking could be

$$\delta_3 \equiv \frac{\tilde{m}_s - \tilde{m}_d}{E_h}, \quad (7.45)$$

where \tilde{m}_q are constituent quark masses and E_h is the recoil energy of the hadron. Thus, for standard values of the strange and down constituents masses this suggests an $SU(3)$ breaking below 10% in most of phase space. On the other hand, the deviations from 1 of the double ratio $F^{(B \rightarrow \rho)}/F^{(B \rightarrow K^*)}/F^{(D \rightarrow \rho)}/F^{(D \rightarrow K^*)}$, with F some arbitrary form factor,

were estimated in Ref. [35] by calculating the effects of chiral loops. The effect was found to be smaller than 3% and, although there could be contributions from higher orders, adds credibility to the use of $SU(3)$ relations.

The short distance structure of the B_s meson decays $B_s \rightarrow (\eta^{(\prime)}, \phi)\ell^+\ell^-$ is the same as that of $B \rightarrow K^{(*)}\ell^+\ell^-$. In the $SU(3)$ limit the branching ratios should be the same. Thus, although departures from the $SU(3)$ predictions could be as large as 20 – 30%, our understanding of the B modes gives us a very good starting point for the B_s decays.

Large Energy Limit (LEL):

In addition the symmetries of the heavy quark limit, additional simplifications occur for exclusive decays in which the recoil energy of the light meson is large, the so-called Large Energy Limit (LEL) [18,36–45]. In this limit, interactions of the light quark with soft or hard collinear gluons do not change its helicity, giving rise to additional symmetries, and corresponding additional relations between form factors. These were first noted in [37], based on symmetries of the "large energy effective theory" (LEET) [36]. (Although LEET is not a well-defined effective theory, these relations remain true in the LEL [18,39, 41].) In addition to the heavy quark symmetry relations in Eqs. (7.35–7.38), the additional symmetries of the LEL gives new relations among the form factors defined in Eqs. (7.27–7.29).

The main result of the LEL which is important for our discussion here, is the fact that all of the form factors in $H \rightarrow (P, V)\ell^+\ell^-$ can be expressed by a total of *three* functions of the heavy mass M and the recoil energy E . For example, the $H \rightarrow P\ell^+\ell^-$ form factors can be written as [37]

$$\begin{aligned} f_+(q^2) &= \xi(M, E), \\ f_-(q^2) &= -\xi(M, E), \\ f_T(q^2) &= \left(1 + \frac{m_P}{M}\right) \xi(M, E), \end{aligned} \quad (7.46)$$

where $\xi(M, E)$ is an unknown function of M and E . Simple inspection shows that the previously derived HQSS relation Eq.(7.35) is satisfied. For the vector meson final state, the form factors obey

$$\begin{aligned} g(q^2) &= \frac{1}{M} \xi_{\perp}, \\ f(q^2) &= -2E \xi_{\perp}, \\ a_+(q^2) &= \frac{1}{M} \left\{ \xi_{\perp} - \frac{m_V}{E} \xi_{\parallel} \right\}, \\ a_-(q^2) &= \frac{1}{M} \left\{ -\xi_{\perp} + \frac{m_V}{E} \xi_{\parallel} \right\}, \end{aligned} \quad (7.47)$$

where $\xi_{\perp}(M, E)$ and $\xi_{\parallel}(M, E)$ refer to the transverse and longitudinal polarizations, respectively.

Additionally, there will be expressions for the "penguin" form factors $T_i(q^2)$, $i = 1, 2, 3$, in terms of ξ_{\perp} and ξ_{\parallel} , which satisfy the HQSS relations in Eqs. (7.36–7.38). The power of

the predictions in Eqs. (7.46–7.47) will become apparent later when computing observables in $B \rightarrow K^{(*)}\ell^+\ell^-$ decays. Let us now only note in passing one example: the ratio of the vector form factor $g(q^2)$ to the axial-vector form factor $f(q^2)$

$$R_V \equiv \frac{g(q^2)}{f(q^2)} \simeq -\frac{1}{2E_{K^*}m_B}, \quad (7.48)$$

only depends on kinematical variables and is unaffected by hadronic uncertainties. This ratio determines, for instance the ratio of the two transverse polarizations in $B \rightarrow (K^*, \rho)$ decays.

Corrections to the LEL relations arise from (i) radiative corrections to the heavy light vertex, (ii) hard gluon exchange with the spectator quark and (iii) nonperturbative corrections which scale like Λ_{QCD}/E_h . $E_h \sim O(m_b)$ is the recoil energy of the light hadronic state. The leading contribution to (i) was calculated in Refs. [40,41], while (ii) was calculated in Ref. [40]. An effective field theory formulation of the LEL appears to be much more complicated than HQET, but there has been much recent work in this direction [18,39,41]. Such a formulation should allow the nonperturbative corrections (iii) to be parametrized, but thus far this has not been done. The theory of exclusive decays in the LEL is currently a very active field, and much additional theoretical work on this subject is to be expected in the future, in particular clarifying the size of the corrections to the limit.

The various LEL relations may be experimentally tested: for example, an experimental measurement of the ratio of the transverse polarizations Γ_+/Γ_- in the semileptonic decay $B \rightarrow \rho\ell\nu$ will provide a test of the relation (7.48). In addition, the relation (7.48), together with the experimental data on $b \rightarrow s\gamma$ decays, has been used to put constraints on the form-factors entering the $B \rightarrow K^*$ matrix element at $q^2 = 0$. This can be seen in Figure 7.3, from which we can fit the vector and axial-vector form-factors giving $V(0) = 0.39 \pm 0.06$ and $A_1(0) = 0.29 \pm 0.02$. Here,

$$V \equiv -(m_B + m_{K^*})g, \quad A_1 \equiv \frac{f}{m_B + m_{K^*}}, \quad (7.49)$$

Model Calculations

The model independent statements described above are not enough to specify all the hadronic matrix elements needed in the decays of interest. Furthermore, lattice QCD calculations of the rare decay form factors are incomplete, at present.

Model calculations are much easier. On the one hand, they tend to be based on uncontrolled approximations. This leads to uncertainties which are difficult (if not impossible) to estimate. On the other hand, models can provide very useful parameterizations of the physics and may help us understand the region of validity of some of those assumptions.

In heavy-to-light transitions, such as $B \rightarrow K^{(*)}\ell^+\ell^-$ and $B \rightarrow (\pi\rho)\ell\nu$, the rate receives most of its contributions from the large recoil region where $E_h > 1$ GeV. We therefore expect those models that incorporate – in one way or another – our understanding of the

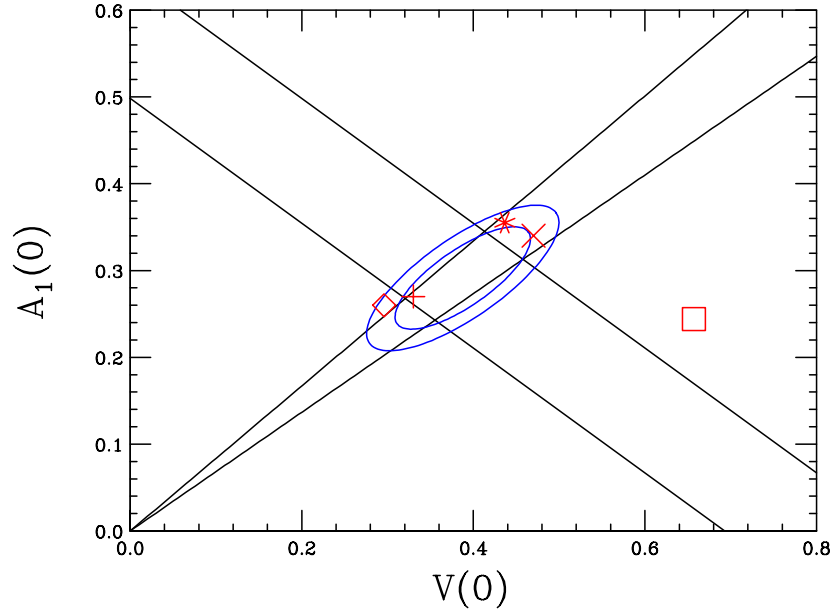


Figure 7.3: Constraints on the semileptonic form-factors $V(0)$ and $A_1(0)$ from $B \rightarrow K^*\gamma$ data plus HQSS (thicker band) together with the relation from the LEL (cone). The ellipses correspond to 68% and 90% confidence level intervals. Central values of model predictions are also shown and correspond to BSW [46] (vertical cross), ISGW2 [50] (diamond), MS [51] (star), LCSR [42] (diagonal cross) and LW [34] (square), respectively.

hadronization of a light quark with relatively large energies to be best suited for these processes. For example, calculations in the light-cone, performed at $q^2 < 0$, and matched at $q^2 = 0$ with the physical region [46,47], as well as light-cone sum rule (LCSR) calculations [48] will give the correct asymptotic behavior of the form factors in QCD as one takes $q^2 \rightarrow -\infty$. Relativistic quark models such as Refs. [49,52,53], include all relativistic effects from the start, instead of treating them as corrections. An important aspect of the transition form factors in these decays, is that their q^2 -dependence may not be trivial. The widely used assumption of monopole behavior

$$F(q^2) = \frac{F(0)}{1 - q^2/M_*^2}, \quad (7.50)$$

where $F(q^2)$ is a given form factor and M_* is the mass of a nearby resonance, may receive large corrections in heavy-to-light transitions. This is not the case in D and $B \rightarrow D^{(*)}\ell\nu$ decays, where the energy release is small compared to the mass gap to heavier resonances, and the nearest (or single) pole approximation is good. In $B \rightarrow$ light transitions the form factors are sensitive to the influence of additional resonances at high recoil. In fact, a sum rule for the resonance contributions can be derived [54] once the asymptotic behavior in the $q^2 \rightarrow -\infty$ limit, which is known in QCD, is imposed. This leads to a suppression of the monopole behavior in favor of a mixed q^2 dependence in agreement with QCD predictions in the appropriate limit. This also agrees with results from LCSR calculations.

In summary, the phenomenological models we consider, capture at least some of the

important physics (especially at high recoil). Until reliable lattice QCD results come on line, we can combine the model results with model independent results from HQET and LEL, as well as bounds on form factors from dispersion relations [55]. All of this taken together results in rather constrained form factors. Another strategy for reducing theoretical uncertainties, is the identification of observables which are insensitive to differences in the model predictions.

The issue with $c\bar{c}$ resonances, cuts

Rare decays receive a contribution from diagrams which contain $q\bar{q}$ loops. The $q\bar{q}$ loops can hadronize into vector mesons before decaying electromagnetically. The contribution of $c\bar{c}$ loops at q^2 values near the resonance masses, $q^2 \sim m_V^2$, where $V = J/\psi, \psi', \psi'' \dots$ is an important background to rare decays. It contributes via $B \rightarrow K, K^*V \rightarrow K, K^*\ell^+\ell^-$. Of the six charmonium resonances [56], the dominant ones, $J/\psi(3097)$ and $\psi'(3686)$, divide the spectra naturally into three regions: a low q^2 -region below the J/ψ , a mid q^2 -region between the J/ψ and the ψ' , and a high q^2 -region above the ψ' . This is shown in Figure 7.4. The resonance regions can be included into the calculation by the parameterization given in [57] which is based on dispersion relations and experimental data on $e^+e^- \rightarrow$ hadrons. For a discussion of other approaches [35,58] see Refs. [3,59]. All methods result in a modification of the function Y in C_9^{eff} and rely on factorization.

Kinematic cuts in q^2 are required to allow a reliable extraction of the short distance coefficients from experimental measurements. Figures 7.4 and 7.5 show the difference between the differential decay rate for $B \rightarrow K, K^*\mu^+\mu^-$ with and without inclusion of the resonant $c\bar{c}$ states. The lower curves only include non-resonant (or pure short distance) contributions, while the upper curves also include the contribution from resonant $c\bar{c}$ states (according to Ref. [57]). It is clear from these figures that the low q^2 -region is the preferred region for comparing theory and experiment, because this region i) receives the largest contribution to the rate and ii) is not affected by higher $c\bar{c}$ resonances.

Branching ratios and invariant dilepton mass distributions

Table 7.2 lists the non-resonant branching ratios for the various $B \rightarrow K, K^*\ell^+\ell^-$ channels in the standard model². The kinematic range of the dilepton mass is $4m_\ell^2 \leq q^2 < (m_B - m_{(K,K^*)})^2$. The $B \rightarrow K^*\ell^+\ell^-$ decays receive a contribution from the photon pole, $|C_7^{\text{eff}}|^2/q^2$. The rate for $B \rightarrow K^*e^+e^-$ is enhanced compared to the rate for the corresponding decay into muons, because of the greater sensitivity to the photon pole in the decay into electrons. (The photon pole is absent for decays into pseudoscalar K mesons, see Figure 7.4).

The dilepton invariant mass distributions for the $B \rightarrow K, K^*\mu^+\mu^-$ decays are shown in Figures 7.4 and 7.5, respectively. Imposing the cuts $0.25 \text{ GeV}^2 \leq q^2 < 8.0 \text{ GeV}^2$ (low q^2 region), and including the charmonium resonances according to Ref. [57] we obtain the following partially integrated standard model branching ratios: $\Delta\mathcal{B}_H$ for $B \rightarrow H\mu^+\mu^-$:

²More stringent experimental bounds have recently been published by CLEO [63].

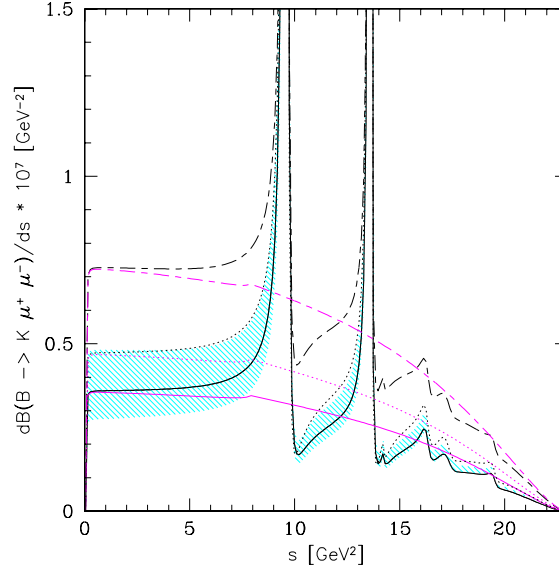


Figure 7.4: The dilepton invariant mass distribution in $B \rightarrow K\mu^+\mu^-$ decays, using the form factors from LCSR. Resonant $c\bar{c}$ states are parametrized as in Ref. [57]. The solid line represents the SM and the shaded area depicts the form-factor related uncertainties. The dotted line corresponds to the SUGRA model with $R_7 = -1.2$, $R_9 = 1.03$ and $R_{10} = 1$. The long-short dashed lines correspond to an allowed point in the parameter space of the MIA-SUSY model, given by $R_7 = -0.83$, $R_9 = 0.92$ and $R_{10} = 1.61$. The corresponding pure short-distance spectra are shown in the lower part of the plot. Figure taken from Ref. [42].

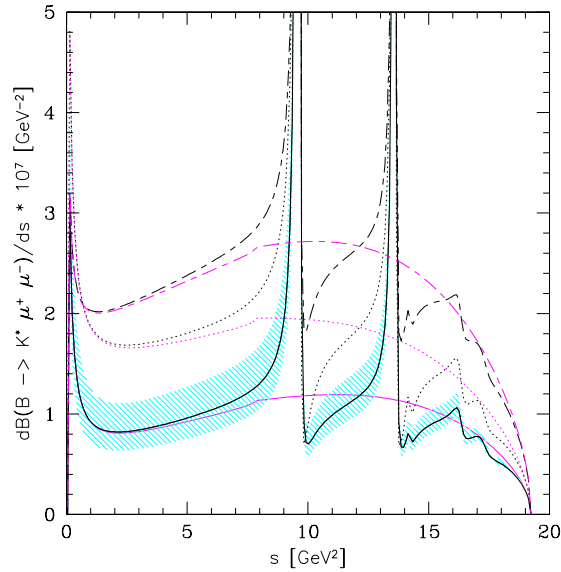


Figure 7.5: The dilepton invariant mass distribution in $B \rightarrow K^*\mu^+\mu^-$ decays. Legends are the same as in Figure 7.4. Figure taken from Ref. [42].

mode	SM branching ratio	data	Exp. reference
$b \rightarrow se^+e^-$	$8.4 \pm 2.3 \times 10^{-6}$	$< 10.1 \times 10^{-6}$	BELLE [60]
$b \rightarrow s\mu^+\mu^-$	$5.7 \pm 1.2 \times 10^{-6}$	$< 19.1 \times 10^{-6}$	BELLE [60]
$B \rightarrow Ke^+e^-$	$5.7 \pm 2.0 \times 10^{-7}$	$(0.48_{-0.24-0.11}^{+0.32+0.09}) \times 10^{-6}$	BELLE [61]
$B \rightarrow K\mu^+\mu^-$	$5.7 \pm 2.0 \times 10^{-7}$	$(0.99_{-0.32-0.14}^{+0.40+0.13}) \times 10^{-6}$	BELLE [61]
$B \rightarrow K\ell^+\ell^-$	$5.7 \pm 2.0 \times 10^{-7}$	$(0.75_{-0.21}^{+0.25} \pm 0.09) \times 10^{-6}$	BELLE [61]
$B \rightarrow K\ell^+\ell^-$	$5.7 \pm 2.0 \times 10^{-7}$	$< 0.6 \times 10^{-6}$	BABAR [62]
$B \rightarrow K^*e^+e^-$	$2.3 \pm 0.8 \times 10^{-6}$	$< 5.1 \times 10^{-6}$	BELLE [60]
$B \rightarrow K^*\mu^+\mu^-$	$1.9 \pm 0.7 \times 10^{-6}$	$< 3.0 \times 10^{-6}$	BELLE [60]

Table 7.2: Current status of rare semileptonic B decays. SM branching ratios are taken from [25,42], and upper bounds are given at 90% C.L.

$\Delta\mathcal{B}_K = 2.90 \times 10^{-7}$ and $\Delta\mathcal{B}_{K^*} = 7.67 \times 10^{-7}$. The theoretical uncertainty in these branching fractions has been estimated to be $\pm 30\%$ [42].

For comparison, in a generic non-standard model scenario, choosing $C_7^{\text{eff}} = -C_7^{\text{eff}}|_{SM}$ and C_9, C_{10} equal to their standard model values, we obtain $\Delta\mathcal{B}_K = 3.63 \times 10^{-7}$ and $\Delta\mathcal{B}_{K^*} = 13.09 \times 10^{-7}$. The enhancement results from constructive interference of C_7^{eff} with C_9 .

The Forward-Backward Asymmetry $A_{FB}(q^2)$

As discussed in Sec. 7.1.2.2, the forward-backward asymmetry of the leptons in inclusive $b \rightarrow s\ell^+\ell^-$ provides a means of measuring the Wilson coefficients C_7, C_9 and C_{10} . The latter two may be sensitive to different aspects of the physics at short distances and disentangling their contributions, as well as the sign of C_7 , will result in additional constraints on New Physics.

In this section we discuss the forward-backward asymmetry for exclusive decays. In addition to the branching ratios and the decay distributions, exclusive decays to vector mesons carry angular information sensitive to the short distance physics. Here we are concerned with the potential for cleanly extracting short distance physics from the asymmetry in exclusive modes, such as $B \rightarrow K^*\ell^+\ell^-$, $B_s \rightarrow \phi\ell^+\ell^-$, etc. In principle, one might expect that theoretical predictions for exclusive modes are much more uncertain than predictions for inclusive decays due to the presence of hadronic form factors. However, as we will discuss, the LEL relations (7.46-7.47) allow for a clean determination of the Wilson coefficient C_9^{eff} in terms of C_7^{eff} , through a measurement of the position of the zero of $A_{FB}(q^2)$.

The angular distribution in $B \rightarrow K^*\ell^+\ell^-$ is given by

$$\frac{d^2\Gamma}{dq^2 d\cos\theta} = \frac{G_F^2 \alpha^2 |V_{tb}^* V_{ts}|^2}{768\pi^5 m_B^2} \mathbf{k}q^2 \left\{ (1 + \cos\theta)^2 [|H_+^L|^2 + |H_-^R|^2] \right. \\ \left. + (1 - \cos\theta)^2 [|H_-^L|^2 + |H_+^R|^2] + 2 \sin^2\theta |H_0|^2 \right\}, \quad (7.51)$$

where \mathbf{k} is the K^* spatial momentum, and θ is the angle between the ℓ^+ and the B meson in the dilepton center-of-mass frame. The transverse helicity amplitudes in terms of the form factors take the form [65]

$$H_\alpha^L = \left[C_7 \frac{m_b(m_B - E_{K^*} + \eta_\alpha \mathbf{k})}{q^2} + \frac{C_9 - C_{10}}{2} \right] (f + \eta_\alpha 2m_B \mathbf{k}g), \quad (7.52a)$$

$$H_\alpha^R = \left[C_7 \frac{m_b(m_B - E_{K^*} + \eta_\alpha \mathbf{k})}{q^2} + \frac{C_9 + C_{10}}{2} \right] (f + \eta_\alpha 2m_B \mathbf{k}g), \quad (7.52b)$$

where $\alpha = +, -$, $\eta_\alpha = (1, -1)$, and E_{K^*} is the K^* energy in the B rest frame. The index α in Eqs. (7.52) refers to the $+, -$ polarizations of the K^* , and the L, R subscripts refer to left and right-handed leptons. The longitudinal helicity amplitude is described by

$$H_0^L = \frac{m_B^2}{m_{K^*} \sqrt{q^2}} \left\{ C_7 \frac{m_b}{q^2 m_B} \left\{ f [E_{K^*} (m_B - E_{K^*}) - \mathbf{k}^2] + 2g m_B \mathbf{k}^2 (m_B - 2E_{K^*}) \right\} \right. \\ \left. + \frac{(C_9 - C_{10})}{2} \left[2\mathbf{k}^2 a_+ - \frac{E_{K^*}}{m_B} f \right] \right\}, \quad (7.53)$$

and H_0^R is given by replacing $(C_9 - C_{10})/2$ with $(C_9 + C_{10})/2$ in Eq. (7.53).

The forward-backward asymmetry for leptons as a function of the dilepton mass squared $m_{\ell\ell}^2 = q^2$ is now defined as

$$A_{FB}(q^2) = \frac{\int_0^1 \frac{d^2\Gamma}{dx dq^2} dx - \int_{-1}^0 \frac{d^2\Gamma}{dx dq^2} dx}{\frac{d\Gamma}{dq^2}}, \quad (7.54)$$

where $x \equiv \cos \theta$. We can write A_{FB} in terms of the helicity amplitudes defined in Eqs. (7.52) and (7.53):³

$$A_{FB}(q^2) = \frac{3}{4} \frac{|H_-^L|^2 + |H_+^R|^2 - |H_+^L|^2 - |H_-^R|^2}{|H_-^L|^2 + |H_+^R|^2 + |H_+^L|^2 + |H_-^R|^2 + |H_0^L|^2 + |H_0^R|^2}. \quad (7.55)$$

As it can be seen from Eqs. (7.52) and (7.55), the asymmetry is proportional to the Wilson coefficient C_{10} and vanishes with it. Furthermore, it is proportional to a combination of C_9^{eff} and C_7^{eff} such that it has a zero in the physical region if the following condition is satisfied [38]

$$\text{Re}[C_9^{\text{eff}}] = -\frac{m_b}{q_0^2} C_7^{\text{eff}} \left\{ \frac{T_1}{g} + (m_B^2 - m_{K^*}^2) \frac{T_2}{f} \right\}, \quad (7.56)$$

where q_0^2 is the position of the zero of A_{FB} and all q^2 -dependent quantities are evaluated at q_0^2 . This relation depends on the form factors T_1 and T_2 ; however, it was noted in Ref. [38] that the location of the zero of the asymmetry was approximately constant in a variety of form-factor models, as shown in Figure 7.6. This is a consequence of helicity conservation of the K^* in the large energy limit in these models, arising from the relativistic treatment of quark spin.

³The sign of $A_{FB}(q^2)$ defined in this way will change when considering \bar{B}^0 or B^- decays.

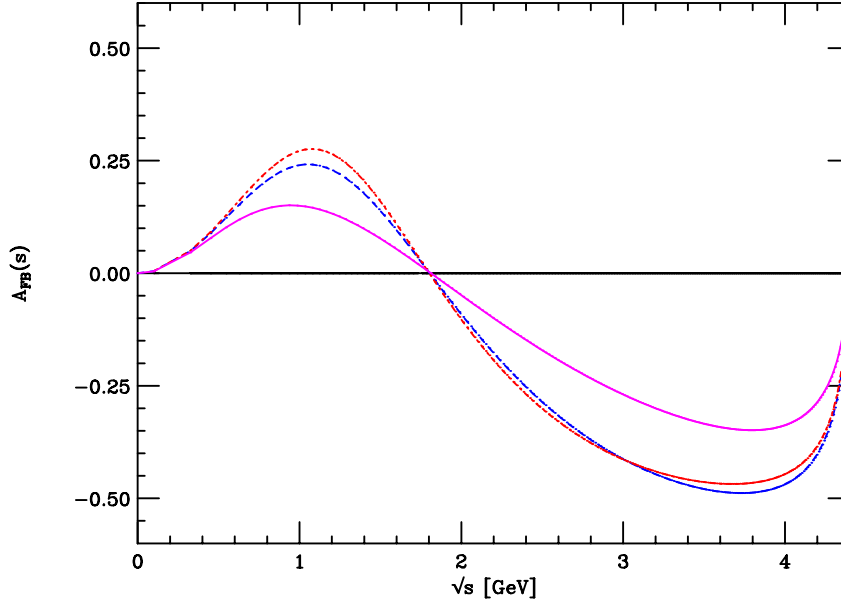


Figure 7.6: The non-resonant forward-backward asymmetry of leptons A_{FB} defined in (7.54), for $B \rightarrow K^* e^+ e^-$ as a function of the dilepton mass s , from Ref. [38]. The asymmetry is computed by making use of the semileptonic form factors from the BSW* model of Ref. [46] (solid line), the light-cone QCD sum rule calculation of Ref. [48] (dashed line) and the relativistic quark model of Ref. [49] (dot-dashed line).

The model independence of the location of the zero in the asymmetry was shown to be a consequence of the large energy limit of QCD in Ref. [42]. After we apply the HQSS and LEL relations (7.47) to (7.56) we find

$$\text{Re}[C_9^{\text{eff}}] = -\frac{2m_B m_b}{q_0^2} C_7^{\text{eff}} + \dots \quad (7.57)$$

where we have neglected the mass of the K^* , which is formally subleading.

Radiative corrections to the location of the asymmetry zero (7.57) were calculated in [40,41,44] and are at the few percent level. Ref. [44] finds the location of the zero in the SM to be

$$q_0^2 = 4.2 \pm 0.6 \text{ GeV}^2 \quad (7.58)$$

where the largest uncertainty comes from the scale dependence of the Wilson coefficients and the estimate of formally subleading $O(m_{K^*}^2/m_B^2)$ terms.

We conclude that the measurement of the zero of the forward-backward asymmetry for leptons in $B \rightarrow K^* \ell^+ \ell^-$ constitutes a test of the short distance structure of the Wilson coefficients C_9 and C_7 through Eq. (7.57). It should be stressed that there are unknown nonperturbative corrections to the relation (7.57) which formally scale as Λ_{QCD}/E_H , but whose size is unknown. Thus, experimental tests of LEL relations will be important in establishing the reliability and accuracy of this approach.

The Forward-Backward CP Asymmetry

The forward-backward CP asymmetry (A_{FB}^{CP}) has been proposed in Ref. [3] as an observable to probe non-standard CP violation in FCNC Z-penguins. It is defined from the forward-backward asymmetry of the previous subsection as

$$A_{FB}^{CP}(s) = \frac{A_{FB}^{(\bar{B})}(s) + A_{FB}^{(B)}(s)}{A_{FB}^{(\bar{B})}(s) - A_{FB}^{(B)}(s)}. \quad (7.59)$$

This definition isolates the phase of C_{10} and the effect scales in units of the phase of C_9^{eff} , which has a CP conserving phase encoded in the function Y from the 4-Fermi operators $A_{FB}^{CP}(s) \sim (\text{Im } C_{10}/\text{Re } C_{10})(\text{Im } C_9^{\text{eff}}/\text{Re } C_9^{\text{eff}})$, see Ref. [3] for details. Using the high q^2 integration region above the ψ' (only here $\text{Im } C_9^{\text{eff}}$ is sizeable) $14.5\text{GeV}^2 \leq q^2 < (m_B - m_{K^*})^2$ yields $\Delta A_{FB}^{CP} = (0.03 \pm 0.01) \times \text{Im } C_{10}/\text{Re } C_{10}$. Despite the substantial uncertainties related with higher ψ'' resonances, the forward-backward CP asymmetry is a unique probe of the flavor sector, since the SM background due to CKM phases is very small $< 10^{-3}$ and ΔA_{FB}^{CP} can be sizeable in case of large CP violating phases of C_{10} .

CP asymmetries in the rate

We define a direct CP violating asymmetry distribution between the dilepton mass spectra in $\bar{B} \rightarrow \bar{H}\ell^+\ell^-$ decays and the CP conjugate process $B \rightarrow H\ell^+\ell^-$ as [69]⁴

$$A_H^{CP}(s) = \frac{\frac{d\Gamma_{\bar{H}}^{\bar{B}}}{ds} - \frac{d\Gamma_H^B}{ds}}{\frac{d\Gamma_{\bar{H}}^{\bar{B}}}{ds} + \frac{d\Gamma_H^B}{ds}} \quad (7.60)$$

Here H can be a pseudoscalar or vector final state meson, for example, K or K^* . For a non-zero A_H^{CP} in the SM we have to reintroduce the CKM suppressed piece $\lambda_u(T_u - T_c)$ (see Section 7.1.1) into the amplitude, e.g. [66]. In addition to the charmonium background discussed in Section 7.1.3.3 now intermediate $u\bar{u}$ resonances ρ, ω have to be taken into account [67]. To reduce the related uncertainties one uses kinematical cuts $q^2 \gtrsim m_\rho^2, m_\omega^2$ analogous to the $c\bar{c}$ sector.

Unlike the radiative modes induced by $b \rightarrow s\gamma$ where $A_\gamma^{CP} \sim \alpha_s$ [68], the CP asymmetry in $b \rightarrow s\ell^+\ell^-$ transitions starts at the lowest order: the SM contribution to A_H^{CP} stems from interference between the weak phase and the CP conserving imaginary part of C_9^{eff} . Both lead to very small values of A_H^{CP} in the SM: as in any $b \rightarrow s$ transition CKM structure dictates $A^{CP} \sim \text{Im}(\lambda_u/\lambda_t) = \lambda^2\eta < 2\%$, where λ, η are Wolfenstein parameters. The second suppression comes from the strong phase $\text{Im } Y(q^2) \ll C_9$, which holds everywhere except at $q^2 \sim m_V^2$. Integrating $A_H^{CP}(s)$ over the low q^2 -region $1.4\text{GeV}^2 \leq q^2 < 8.4\text{GeV}^2$ yields $A_{K, K^*}^{CP} \simeq 0.1\%$ in the SM [69], comparable with the findings for the inclusive $B \rightarrow X_s\ell^+\ell^-$

⁴An alternative definition is $A_H^{CP'}(s) = \left(\frac{d\Gamma_{\bar{H}}^{\bar{B}}}{ds} - \frac{d\Gamma_H^B}{ds}\right)/(\Gamma_{\bar{H}}^{\bar{B}} + \Gamma_H^B)$ [66,70].

decays $(a_{CP})_s = -0.19_{-0.19}^{+0.17}\%$ [66], which uses different cuts ($1\text{GeV}^2 \leq q^2 < 6\text{GeV}^2$) and a slightly different CP asymmetry (sign and normalization), see footnote 4 and Ref. [66] for details.

Supersymmetric effects in the CP asymmetry in exclusive $B \rightarrow K, K^* \ell^+ \ell^-$ decays have been studied in Refs. [69,70]. The presence of non-SM CP phases can change the sign and magnitude of A_H^{CP} : In the low q^2 -region, $1.4\text{GeV}^2 \leq q^2 < 8.4\text{GeV}^2$, the integrated asymmetry is still not large $|A_{K,K^*}^{CP}| \lesssim 1\%$ [69], but can exceed the SM asymmetry.

7.1.3.4 $B \rightarrow K^* \gamma$ and Related Decays

Exclusive radiative decays are experimentally relatively easily accessible, since their final states can be completely reconstructed. The study of these decays is well motivated as they can provide information on the ratio of CKM elements V_{td}/V_{ts} , and assist in the reduction of the theoretical error on the determination of V_{ub} from $B \rightarrow \rho \ell \nu$. In addition they are sensitive to loop effects of new interactions which may result in CP violating effects in the charge asymmetry of $B \rightarrow K^* \gamma$. Unfortunately, these transitions are also sensitive to theoretical uncertainties of two different origins. First, there is the uncertainty due to the poorly known hadronic matrix elements of the short distance operators which contribute to the rate. The second uncertainty is due to long distance contributions (see the discussion in Section 7.1.3.1). More theoretical effort is needed in this area. At present, CLEO has observed two channels [71], with the branching fractions, $B(B^0 \rightarrow K^{*0} \gamma) = (4.55_{-0.68}^{+0.72} \pm 0.34) \times 10^{-5}$, $B(B^+ \rightarrow K^{*+} \gamma) = (3.76_{-0.83}^{+0.89} \pm 0.28) \times 10^{-5}$, and $B(B \rightarrow K_2^*(1430) \gamma) = (1.66_{-0.53}^{+0.59} \pm 0.13) \times 10^{-5}$.

As shown in Section 7.1.3.1, the short distance contribution to radiative decays depends on only one form factor, $T_1(q^2 = 0)$. This form factor has been calculated from a wide variety of theoretical approaches. A sampling of some more recent results [72] is given in Table 7.3 for the case of $B \rightarrow K^* \gamma$. The LCSR results listed there are in good agreement with the CLEO data. However, Table 7.3 also shows that there are significant differences among the theoretical predictions of the form factor $T_1^{B \rightarrow K^*}(q^2 = 0)$, and the related ratio of rates for exclusive to inclusive decays, R_{K^*} .

We note that the lattice results shown in Table 7.3 do not contain a complete analysis of all systematic errors. The calculations date back to 1994 and 1995, a time when improved actions and heavy quark methods were just being established. The results were obtained in the quenched approximation. Both calculations use pole dominance to extrapolate the form factors from the high q^2 region (where it was calculated) to the physical $q^2 = 0$ point. Both calculations are performed at heavy quark masses below the b quark mass, and they both rely on heavy quark extrapolations to obtain results for the B meson decay.

Estimates for the rates of decays into higher K^* resonances are cataloged in Ref. [73]. In the case of the $K_2^*(1430)$ mode, the CLEO data appears to favor the model of Veseli and Olsson, which predicts $B(B \rightarrow K_2^*(1430) \gamma) = (1.73 \pm 0.80) \times 10^{-5}$. We note that theoretical predictions do not yet exist for the decay $B_s \rightarrow \phi \gamma$, which is not accessible to the B factories.

Ref.	$T_1^{B \rightarrow K^*}(0)$	$\frac{T_1^{B \rightarrow K^*}(0)}{T_1^{B \rightarrow \rho}(0)}$	$B(B \rightarrow K^* \gamma)(\times 10^{-5})$	R_{K^*}
LCSR	0.32 ± 0.05	1.32 ± 0.1	4.8 ± 1.5	0.16 ± 0.05
LCSR	0.31 ± 0.04	1.14 ± 0.02	4.45 ± 1.13	0.16 ± 0.05
LCSR	0.38 ± 0.06	1.33 ± 0.13	--	0.20 ± 0.06
LQCD	$0.10 \pm 0.01 \pm 0.3$	--	--	$0.060 \pm 0.012 \pm 0.034$
LQCD	$0.16^{+0.02}_{-0.01}$	--	--	$0.16^{+0.04}_{-0.03}$

Table 7.3: Form-factor predictions from Ref. [72]. LCSR denotes calculations based on light-cone sum rules, and LQCD denotes calculations based on lattice QCD.

We can determine the ratio of CKM elements, V_{td}/V_{ts} from the ratio of exclusive decay rates,

$$\frac{\Gamma(B \rightarrow \rho \gamma)}{\Gamma(B \rightarrow K^* \gamma)} = \Phi \frac{|T_1^{B \rightarrow \rho}(0)|^2}{|T_1^{B \rightarrow K^*}(0)|^2} \frac{|V_{td}|^2}{|V_{ts}|^2}. \quad (7.61)$$

Φ is a phase space factor. The ratio of form factors in Eq. (7.61), $T_1^{B \rightarrow \rho}(0)/T_1^{B \rightarrow K^*}(0)$, is mostly sensitive to SU(3) breaking effects. Since other theoretical uncertainties are likely to cancel, the ratio may be more accurately calculated than the form factors themselves.

Eq. (7.61) assumes that the decay rates are dominated by contributions from the short distance operator. This is the case for $B \rightarrow K^* \gamma$, where long distance effects have been estimated to be no more than $\simeq 5\%$ [74,75], and where the theoretical estimates of R_{K^*} are tend to be consistent with experiment. However, the long distance contributions to $B \rightarrow \rho \gamma$ can be large [75,76] and can potentially destroy the validity of Eq. (7.61), since they have a different CKM dependence. These contributions arise from (i) the decay $B \rightarrow \rho V^*$ (which is due to the contributions of internal c - and u -quark loops) with the subsequent conversion of the neutral vector meson V^* to a photon, (ii) weak annihilation and W exchange diagrams with subsequent γ radiation, and (iii) final state interactions. If these these effects are included, the resulting theoretical error in determinations of V_{td} from Eq. (7.61) has been estimated to be $\sim 35\%$ [75].

Finally, we consider the radiative baryon decay, $\Lambda_b \rightarrow \Lambda \gamma$. This decay is well suited for the hadron collider environment, and has an estimated Standard Model branching ratio of $B(\Lambda_b \rightarrow \Lambda \gamma) \sim 5 \times 10^{-5}$ [77,78]. Like the corresponding decays of B mesons, the underlying quark transition is $b \rightarrow s \gamma$ and described by the short distance effective Hamiltonian in Eq. (7.1). However, the spin 1/2 baryons makes more degrees of freedom accessible to experiments. In particular, one can probe the $V - A$ structure of the Standard Model and search for contributions of non-standard helicity in the FCNC dipole operator.

Measurement of final state polarization in $\Lambda_b \rightarrow (\Lambda \rightarrow \pi p) \gamma$ decays has been recently discussed in [78] along with asymmetries related to initial Λ_b polarization. This work corrected the expression for the Λ polarization asymmetry of the original work [77]. (The older calculation was not in agreement with existing calculations of general spin correlations for baryon \rightarrow baryon-vector decays). Note that the Λ asymmetry observable is theoretically simple, since the amplitude into an on-shell photon involves only one form factor, which

drops out in the asymmetry [78]. The relevant single form factor can be extracted from $\Lambda_c \rightarrow \Lambda \ell \bar{\nu}_\ell$ decays using heavy quark spin and flavor symmetry [77] and can be used for an estimate of the new physics reach [78]. In addition, the long distance effects due to vector-meson dominance and weak annihilation diagrams are estimated to be small [77]. Hence, $\Lambda_b \rightarrow \Lambda \gamma$ decays is dominated by short distance physics and is particularly clean, theoretically. It offers unique opportunities to test the helicity structure of the underlying theory, but also to study CP violation [78] by comparing decays of the Λ_b and its conjugate $\bar{\Lambda}_b$.

7.1.3.5 $B_{s,d} \rightarrow \ell^+ \ell^-$

The decay $B_q \rightarrow \ell^+ \ell^-$, where $q = d$ or s and $\ell = e, \mu$ or τ , proceeds through loop diagrams and is of fourth order in the weak coupling. In the SM, the dominant contributions to this decay come from the W box and Z penguin diagrams shown in Figure 7.7. Because the

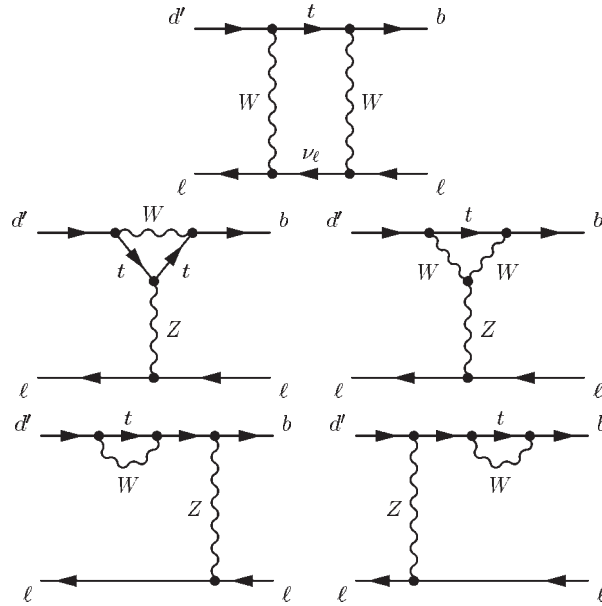


Figure 7.7: Dominant SM diagrams for $B_{s,d} \rightarrow \ell^+ \ell^-$.

contributions with a top quark in the loop are dominant, at low energies of order m_b the decay can be described by a local $\bar{b}q\bar{\ell}\ell$ coupling via the effective Hamiltonian,

$$\mathcal{H}_{\text{eff}} = -4 \frac{G_F}{\sqrt{2}} V_{tq}^* V_{tb} [C_{10} O_{10} + C_S O_S + C_P O_P], \quad (7.62)$$

where O_{10} is given in Eq. 7.2 and the other two operators are

$$O_S = -\frac{e^2}{16\pi^2} \bar{q}_{L\alpha} b_{R\alpha} \bar{\ell}\ell, \quad O_P = -\frac{e^2}{16\pi^2} \bar{q}_{L\alpha} b_{R\alpha} \bar{\ell}\gamma_5 \ell, \quad (7.63)$$

where we have neglected contributions proportional to the q mass. The vector leptonic operator $\bar{\ell}\gamma^\mu \ell$ does not contribute for on-shell leptons because it gives zero when contracted with the B_q momentum.

The diagrams in Figure 7.7 were calculated in [79] and contribute only to the Wilson coefficient C_{10} . There is no contribution from a photonic penguin because of the photon's purely vector coupling to leptons. There are also contributions to the Wilson coefficient C_S from a SM Higgs penguin [80] and to the Wilson coefficient C_P from the would-be neutral Goldstone boson penguin [81], but these contributions to the amplitude are suppressed by a factor of m_b^2/M_W^2 relative to the dominant contributions and can be ignored. We keep C_S and C_P here for completeness because they can be significant in some extensions of the SM. A recent review may be found in [82].

The Wilson coefficients are evaluated at the high scale $\sim \mathcal{O}(M_W)$ and then run down to the low scale $\sim \mathcal{O}(m_B)$, where the hadronic matrix elements of the operators are evaluated. This running in general leads to QCD corrections enhanced by large logarithms of the ratio of scales, which must be resummed. The operator O_{10} has zero anomalous dimension because it is a $(V - A)$ quark current, which is conserved in the limit of vanishing quark masses. Thus the renormalization group evolution of C_{10} is trivial. The operators O_S and O_P have the same form as a quark mass term and thus have the anomalous dimension of a quark mass. In the SM and many extensions, C_S and C_P are proportional to m_b . Thus the running of these Wilson coefficients is properly taken into account by replacing $m_b(M_W)$ with $m_b(m_B)$ in C_S and C_P .

Evaluating the hadronic matrix elements, the resulting branching ratio is

$$\begin{aligned} \mathcal{B}(B_q \rightarrow \ell^+ \ell^-) &= \frac{G_F^2 \alpha^2 m_{B_q}^3 \tau_{B_q} f_{B_q}^2}{64\pi^3} |V_{tb}^* V_{tq}|^2 \sqrt{1 - \frac{4m_\ell^2}{m_{B_q}^2}} \\ &\times \left[\left(1 - \frac{4m_\ell^2}{m_{B_q}^2} \right) \left| \frac{m_{B_q}}{m_b + m_q} C_S \right|^2 + \left| \frac{2m_\ell}{m_{B_q}} C_{10} - \frac{m_{B_q}}{m_b + m_q} C_P \right|^2 \right], \end{aligned} \quad (7.64)$$

where τ_{B_q} is the B_q lifetime, f_{B_q} is the B_q decay constant normalized according to $f_\pi = 132$ MeV, and we retain the Wilson coefficients C_S and C_P for completeness.

The SM decay amplitude is given by the Wilson coefficient [79]

$$C_{10} = -Y(x_t)/\sin^2 \theta_W, \quad (7.65)$$

where $x_t = m_t^2(m_t)/M_W^2 = 4.27 \pm 0.26$ with m_t evaluated in the $\overline{\text{MS}}$ scheme at $\mu = m_t$ (giving $m_t(m_t) = 166$ GeV). The function $Y(x_t)$ is given by $Y(x_t) = Y_0(x_t) + \frac{\alpha_s}{4\pi} Y_1(x_t)$ at NLO. At LO [79],

$$Y_0(x_t) = \frac{x_t}{8} \left[\frac{x_t - 4}{x_t - 1} + \frac{3x_t}{(x_t - 1)^2} \log x_t \right] = 0.972 \left[\frac{m_t(m_t)}{166 \text{ GeV}} \right]^{1.55}, \quad (7.66)$$

where we have taken the central value of x_t and parameterized the remaining m_t dependence.

As explained above, the operator O_A has zero anomalous dimension and so the QCD running of the Wilson coefficient from the electroweak scale to the B_q mass scale is trivial. Nontrivial QCD corrections first arise at NLO and require the calculation of two-loop diagrams [83,84]. The result of the two-loop calculation in the $\overline{\text{MS}}$ scheme is [84]

	B_d	B_s
$\tau^+\tau^-$	$3.4_{-2.0}^{+2.7} \times 10^{-8}$	$9.2_{-1.8}^{+1.9} \times 10^{-7}$
$\mu^+\mu^-$	$1.6_{-0.9}^{+1.3} \times 10^{-10}$	$4.3_{-0.8}^{+0.9} \times 10^{-9}$
e^+e^-	$3.8_{-2.2}^{+3.0} \times 10^{-15}$	$1.0 \pm 0.2 \times 10^{-13}$

Table 7.4: SM branching ratios for B_d and B_s into $\tau^+\tau^-$, $\mu^+\mu^-$ and e^+e^- . The difference in the relative size of the errors in the B_d and B_s branching ratios is due primarily to the difference in the relative size of the errors in V_{td} and V_{ts} .

$$\begin{aligned}
Y_1(x) = & \frac{x^3 + 2x}{(x-1)^2} \text{Li}_2(1-x) + \frac{x^4 - x^3 + 14x^2 - 2x}{2(x-1)^3} \log^2 x \\
& + \frac{-x^4 - x^3 - 10x^2 + 4x}{(x-1)^3} \log x + \frac{4x^3 + 16x^2 + 4x}{3(x-1)^2} \\
& + \left[\frac{2x^2 - 4x}{(x-1)} + \frac{-x^3 + 7x^2}{(x-1)^2} + \frac{-6x^2}{(x-1)^3} \log x \right] \log \left(\frac{\mu^2}{M_W^2} \right). \quad (7.67)
\end{aligned}$$

Here μ is the renormalization scale at which the top quark mass is renormalized. Numerically, $Y_1(x_t) = 2.65$, and the NLO contributions give (taking the central value of x_t) $Y(x_t) = 1.026 \times Y_0(x_t) = 0.997$.

The SM predictions for the branching fractions are given in Table 7.4, where parameter and hadronic uncertainties have been taken into account.⁵

The uncertainties in the branching ratios are due primarily to the uncertainties in $|V_{td}|$, $|V_{ts}|$, and f_{B_q} . An additional uncertainty in the branching ratios due to scheme dependence in the definition of $\sin^2 \theta_W$ is not taken into account; we estimate it to be about 8%.

7.1.4 Expectations for Physics Beyond the Standard Model

Supersymmetry

It is customary to define ratios of Wilson coefficients renormalized at a scale $\mu = m_b$

$$R_i \equiv \frac{C_i}{C_{iSM}} \quad (7.68)$$

parameterizing possible enhancement/decrease w.r.t. the SM Wilson coefficients. Analytical expressions of the MSSM C_i are given in [89], [90].

⁵We use the following parameters: $\alpha = 1/128$ (at M_Z), $s_W^2 = 1 - M_W^2/M_Z^2 = 0.2222$, $\bar{m}_t(m_t) = 166 \pm 5$ GeV, $m_{B_d} = 5279.4$ MeV, $m_{B_s} = 5369.6$ MeV, $\tau_{B_d} = 1.548 \pm 0.032$ ps, $\tau_{B_s} = 1.493 \pm 0.062$ ps, $|V_{tb}| = 0.999$, $|V_{td}| = 0.009 \pm 0.003$, $|V_{ts}| = 0.039 \pm 0.002$, $f_{B_d} = 208 \pm 10 \pm 11$ MeV, and $f_{B_s} = 250 \pm 10 \pm 13_{-0}^{+8}$ MeV. All numbers are taken from the PDG [86] except for f_{B_d} and f_{B_s} which are taken from Ref. [87]. For f_{B_d} and f_{B_s} the statistical and systematic errors are listed separately, and the third error for f_{B_s} comes from the uncertainty in the strange quark mass.

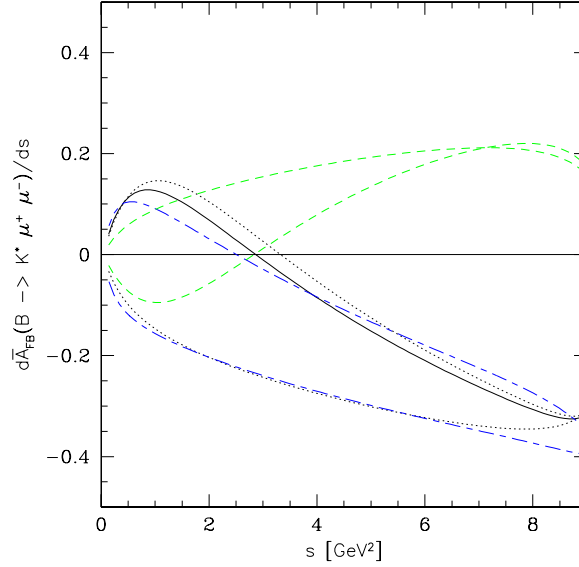


Figure 7.8: The forward-backward asymmetry in $B_d \rightarrow K^{*0} \mu \mu$ decay as a function of $s = M_{\mu\mu}^2$ predicted with the Standard Model (solid line), the SUGRA (dotted), and MIA-SUSY (long-short dashed line) [42].

Supersymmetric effects on R_7, R_9, R_{10} are studied in three scenarios [42], respecting bounds on $b \rightarrow s\gamma$ and direct searches: an effective SUSY model based on minimal flavor violation (MFV) [91], [93], where there are no extra sources of flavor violation besides the ones present already in the Yukawa couplings of the SM, a (minimal and/or relaxed) supergravity (SUGRA) scenario with universal initial conditions at the GUT scale [92] which is effectively MFV like, and a model with generic squark off-diagonal entries parametrized by the mass insertion approximation (MIA) [94].

To summarize: In MFV and SUGRA only very small deviations from the SM in $C_{9,10}$ are possible: $R_9, R_{10} \sim 1$, while C_7^{eff} can vary a lot. However, imposing the $b \rightarrow s\gamma$ constraint on the modulus we get $0.8 < |R_7| < 1.2$ allowing roughly for two solutions: $R_7 \sim 1$ (SM like sign) and $R_7 \sim -1$. Note that the opposite-of-the-SM-sign for C_7^{eff} is only possible for large $\tan\beta$ [42], [92]. Effects of non SM valued R_i in SUGRA and MIA-SUSY on the invariant mass spectra in $B \rightarrow K, K^* \mu^+ \mu^-$ decays are shown in Figure 7.4 and Figure 7.5, respectively. Figure 7.8 shows a comparison of the forward-backward asymmetry in the standard model with SUGRA and MIA-SUSY models.

The MIA-SUSY scenario is one example of a model with non-standard FCNC Z-couplings [3]. Here drastic effects are possible in C_{10} [94], which at present is best constraint by $|C_{10}| < 10$ [3,42] or equivalently $|R_{10}| < 2-3$, namely

- An enhanced $|C_{10}|$, which results in enhanced branching ratios $\mathcal{B}(b \rightarrow s\ell^+\ell^-)$
- $\text{sign}(C_{10}) = -\text{sign}(C_{10}^{\text{SM}})$ causing a sign flip in the forward-backward asymmetry (see Section 7.1.3.3). This is not measurable in the rate, which is proportional to $\supset |C_{10}|^2$.

- A non zero forward-backward-CP asymmetry [3], if C_{10} has a $\mathcal{O}(1)$ phase (see Section 7.1.3.3).

All of these effects are currently not excluded, but none of them can be saturated in a MFV scenario with family universal initial conditions.

Let us put this quite strong statement into a broader context. SUSY as a realistic extension of the SM has to be broken, which is supposed to happen at energies much higher than the weak scale. Experiments in b -physics now have the power to probe the flavor structure of SUSY breaking, i.e. to discriminate between scenarios which are MFV like, and those who are not. The popular models of SUGRA, gauge mediation GMSB, anomaly mediation AMSB and the non-supersymmetric 2HDM are all MFV, but in a general MSSM this does not have to be the case. One example which is non-MFV is given in e.g. [96]. We compile some powerful observables and experimental signatures, which could decide this. MFV is ruled out, if

- $\sin 2\beta$ is small [97]
- $a_{CP}^{Dir}(B \rightarrow X_s \ell^+ \ell^-) > \mathcal{O}(1)\%$ for low dilepton mass
- $A_{FB}(B \rightarrow K^* \ell^+ \ell^-)$ flips sign
- $A_{FB}^{CP}(B \rightarrow K^* \ell^+ \ell^-)$ is significant
- there a large 'wrong' (opposite to the SM ones) helicity contributions found e.g. in $b \rightarrow s\gamma$

Finally, at large $\tan \beta$ there can be large supersymmetric contributions to the scalar operators C_S and C_P (see Sec. 7.1.3.5) leading to large enhancements of $\mathcal{B}(B_{s,d} \rightarrow \ell^+ \ell^-)$ by orders of magnitude [98].

Anomalous Triple Gauge Boson Couplings

The Triple Gauge Boson Couplings (TGC) are an important feature of the gauge sector of the SM. In principle, they may be affected by new physics coming from a scale Λ where this may be, for instance, the scale at which the dynamics responsible for electroweak symmetry breaking becomes apparent. Imposing CP conservation, the most general form of the WWN ($N = \gamma, Z$) couplings can be written as [99]

$$\begin{aligned} \mathcal{L}_{WWN} = g_{WWN} \left\{ i\kappa_N W_\mu^\dagger W_\nu N^{\mu\nu} + ig_1^N \left(W_{\mu\nu}^\dagger W^\mu N^\nu - W_{\mu\nu} W^{\dagger\mu} N^\nu \right) \right. \\ \left. + g_5^V \epsilon^{\mu\nu\rho\sigma} (W_\mu^\dagger \partial_\rho W_\nu - W_\mu \partial_\rho W_\nu^\dagger) N_\sigma + i \frac{\lambda_N}{M_W^2} W_{\mu\nu}^\dagger W_\lambda^\nu N^{\nu\lambda} \right\}, \end{aligned} \quad (7.69)$$

with the conventional choices being $g_{WW\gamma} = -e$ and $g_{WWZ} = -g \cos \theta$. Deviations from the SM values for the TGC are constrained directly from LEP II [100] and Tevatron [101] measurements of gauge boson production. On the other hand, FCNC decay processes at

low energies, such as loop-induced B and K decays, probe these vertices indirectly. The effects of anomalous TGC in rare B decays have been extensively studied in the literature. For instance, the effects of the dimension four anomalous $WW\gamma$ coupling $\Delta\kappa_\gamma$ in $b \rightarrow s\gamma$ transitions were first considered in [102], whereas this plus the dimension six coupling λ_γ were studied in [103,104]. These plus the corresponding CP violating couplings and their effects in the $b \rightarrow s\gamma$ branching fractions were also considered in [105]. Finally, the anomalous WWZ couplings and their effects in $b \rightarrow s\mu^+\mu^-$ were studied in Ref. [107]. In Ref. [108] the effects in $b \rightarrow s\ell^+\ell^-$ are correlated with those in $K \rightarrow \pi\nu\bar{\nu}$ decays. There it is shown that 50% deviations in these branching fractions are possible. This remains the case even after we consider the latest results from LEP II [100]. For instance, from the two-parameter fits in Ref. [100] with $\Delta\kappa_\gamma$ and Δg_1^Z , the 95% C.L. bound for Δg_1^Z is $[-0.08, 0.025]$. The largest contributions come from Δg_1^Z . This sensitivity stems from the fact that the effects induced by Δg_1^Z in rare B and K decays are logarithmically sensitive to the high energy scale Λ [108]. In addition, this kind of values for Δg_1^Z would induce an enhancement of ϵ'/ϵ [109].

Since Δg_1^Z affects almost exclusively the Wilson coefficient C_{10} , it will not change the position of the zero of the forward-backward asymmetry in $B \rightarrow K^*\ell^+\ell^-$. However, the overall value of A_{FB} will be affected.

Finally, we comment on the CP violating anomalous TGC. The main effect there comes from the dimension-four γW^+W^- coefficient $\tilde{\kappa}$. This is bound from $b \rightarrow s\gamma$ to be in the interval $(-0.60, 0.60)$. For instance, this bound translates into [108] $A_{CP}(B^\pm \rightarrow K^\pm\ell^+\ell^-) < 1\%$.

Anomalous Couplings of Fermions to SM Gauge Bosons

The new physics above the energy scale Λ may also modify the effective interactions of the SM fermions to the electroweak gauge bosons. In principle, this also has a parallel in low energy QCD, as it is pointed out in Ref. [110], where symmetry alone is not enough to determine the axial coupling of nucleons to pions. In fact, the departure of this coupling from unity is a non-universal effect, only determined by the full theory of QCD. Thus, in Ref. [110] it is suggested that in addition to the effects in the EWSB sector of the theory, it is possible that the interactions of fermions with the NGBs are affected by the new dynamics above Λ , resulting in anomalous interactions with the electroweak gauge bosons. This is particularly interesting if fermion masses are dynamically generated, as is the case with the nucleon mass. Interestingly, the proximity of the top quark mass to the electroweak scale $v = 246$ GeV, hints the possibility the top mass might be a dynamically generated “constituent” mass. Thus, it is of particular interest to study the couplings of third generation quarks to electroweak gauge bosons.

The anomalous couplings of third generation quarks to the W and the Z can come from dimension-four and dimension-five operators. The indirect effects of the dimension-four operators have been considered in relation to electroweak observables in Ref. [110,111], as well as the $b \rightarrow s\gamma$ transitions [112]. The constraints on dimension-five operators from electroweak physics have been studied in Ref. [113]. In Ref. [114] the effects of all dimension-

four and dimension-five operators in B FCNC transitions such as $b \rightarrow s\gamma$ and $b \rightarrow sl^+\ell^-$ were considered.

Dimension-four Operators:

In a very general parameterization, the dimension-four anomalous couplings of third generation quarks can be written in terms of the usual physical fields as,

$$\begin{aligned} \mathcal{L}_4 = & -\frac{g}{\sqrt{2}} \left[C_L (\bar{t}_L \gamma_\mu b_L) + C_R (\bar{t}_R \gamma_\mu b_R) \right] W^{+\mu} \\ & -\frac{g}{2c_W} \left[N_L^t (\bar{t}_L \gamma_\mu t_L) + N_R^t (\bar{t}_R \gamma_\mu t_R) \right] Z^\mu + \text{h.c.}, \end{aligned} \quad (7.70)$$

where s_W (c_W) is the sine (cosine) of the weak mixing angle, θ_W . The dimension-four operators defined in Eq. (7.70) induce new contributions to the $b \rightarrow s\gamma$ and $b \rightarrow sZ$ loops as well as the box diagram. They appear in the effective Hamiltonian formulation as shifts of the Wilson coefficients $C_7(M_W)$, $C_9(M_W)$ and $C_{10}(M_W)$.

The measured $b \rightarrow s\gamma$ branching ratio imposes a stringent bound on C_R as its contribution to C_7 is enhanced by the factor m_t/m_b . This has been discussed in the literature [112], where the obtained bounds on C_R : $-0.05 < C_R < 0.01$. In principle, this appears to make C_R unnaturally small if it were to be generated by some strong dynamics at the scale Λ . However, it is possible to generate such value for C_R in a large variety of generic strongly coupled theories. For instance, the pseudo-Nambu-Goldstone Bosons (pNGBs) of Extended Technicolor (ETC) that result from the breaking of the various fermion chiral symmetries, generate at one loop a small C_R proportional to m_b [114]:

$$C_R \simeq \frac{1}{4\pi} \frac{m_b m_t}{f_\pi^2} \log \left(\frac{m_\pi^2}{m_t^2} \right). \quad (7.71)$$

This is well within experimental bounds in all ETC incarnations, and it is even smaller in modern ETC theories such as Topcolor-assisted Technicolor [115], where the top quark mass entering in (7.71) is only a few GeV. Thus, here the fact that C_R is small reflects its origin in the explicit ETC-breaking of chiral symmetry responsible for m_b . Another hint of this, is the fact that in general C_R contributes to the renormalization of the b -quark line with a term which does not vanish with m_b :

$$\Sigma(m_b) = \frac{g^2}{32\pi^2} C_R m_t (x - 4) \log \left(\frac{\Lambda^2}{M_W^2} \right). \quad (7.72)$$

Thus if we take into account the potential role of chiral symmetry in suppressing C_R and we rescale this coefficient by defining \hat{C}_R as

$$C_R = \frac{m_b}{\sqrt{2}v} \hat{C}_R, \quad (7.73)$$

(where $v = 246$ GeV), the rescaled bounds on \hat{C}_R are $\mathcal{O}(1)$, leaving the possibility that natural values of this coefficient may still lead to deviations in these decay modes.

On the other hand, the effect in $b \rightarrow sl^+\ell^-$ is dominated by the coefficients C_L , N_L^t and N_R^t . In principle, these coefficients are constrained by electroweak precision measurements,

most notably $\epsilon_1 = \Delta\rho = \alpha T$ and R_b [111]. Once these constraints are taken into account, the effects in FCNC B decays [114] are below 15%.

Dimension-five Operators:

Although in principle dimension-five operators -which involve two gauge bosons or one gauge boson and one derivative- are suppressed by the new physics scale Λ , it is possible that they may have important effects in $b \rightarrow s\ell^+\ell^-$ decays. In Ref. [114] all 17 independent operators are considered. Even after the constraints from electroweak precision measurements and $b \rightarrow s\gamma$ are included 50% to 75% deviations in the branching ratios are possible.

New Physics in the Higgs Sector

The sector responsible for Electroweak Symmetry Breaking (EWSB) is the least understood aspect of the SM. The simplest picture, where one Higgs doublet gives rise to M_W and M_Z , and its Yukawa couplings to fermions give them their masses, is likely to be an effective picture only valid at low energies. Besides the extension of the Higgs sector necessary in supersymmetric theories, it is possible to imagine various more exotic scalar sectors. The simplest extension to a two-Higgs doublet sector results in three possible realizations. In the first one only one doublet gives masses to the fermions (Model I). Another possibility is that each doublet is responsible for giving masses for either the up or the down type fermions (Model II). Both these models avoid tree-level FCNCs in the scalar sector [116]. Model II is also the Higgs sector of the MSSM. Finally, the more general possibility (Model III) allows for such FCNC interactions to take place [117]. The presence of the additional scalar states will in general contribute to FCNC processes. In the case of Models I and II, this happens through the one-loop contributions of charged scalars. These have been studied extensively in the literature [118]. For instance, $b \rightarrow s\gamma$ constrains the mass of the charged Higgs in Model II to be roughly $m_{H^\pm} > 300$ GeV, almost independently of the values $\tan\beta$ [91]. For $m_{H^\pm} > 300$ GeV and large $\tan\beta$, $\mathcal{B}(B_{s,d} \rightarrow \ell^+\ell^-)$ can vary by a factor of two from its SM value in Model II [120]. The phenomenology of Model III has been studied in Ref. [119]. Experimental measurements in $b \rightarrow s\ell^+\ell^-$ modes such as $B \rightarrow K^{(*)}\ell^+\ell^-$ and $B_s \rightarrow \ell^+\ell^-$ are going to have an important impact on the parameter space of these models.

Strong Dynamics

If strong dynamics were responsible for the breaking of the electroweak symmetry at the TeV scale, there could be remnant effects at the weak scale. These could manifest as small deviations in the SM model couplings. In this case, the EWSB sector of the SM can be described by an effective Lagrangian [121] where the leading order corresponds to the SM and higher order corrections come in through higher dimensional operators, and are therefore suppressed by the scale $\Lambda \simeq \mathcal{O}(\infty)$ TeV. Among the possible effects relevant for FCNC B decays are the anomalous triple gauge boson couplings discussed in Section 7.1.4 and the anomalous couplings of fermions to SM gauge bosons of Section 7.1.4. Additionally, corrections to the Nambu-Goldstone boson (NGB) propagators lead, at next to leading order in $\mathcal{L}_{\text{eff.}}$, to non-standard four fermion operators [122]. These are constrained by measurements of $Z \rightarrow b\bar{b}$ and $B^0 - \bar{B}^0$ mixing. They also contribute at one-loop to

$b \rightarrow s$ as well as $s \rightarrow d$ transitions which were studied in Ref. [123]. Their contribution to $b \rightarrow s\gamma$ is negligible since it only starts at two loops. However, the $b \rightarrow s\ell^+\ell^-$ processes receive potentially large deviations, which are correlated with similar deviations in $K^{(+,0)} \rightarrow \pi^{(+,0)}\nu\bar{\nu}$.

Finally, many specific scenarios of strong dynamics in the EWSB sector have relatively light scalar states some of which may contribute to FCNC through loops, or even in some cases at tree level. To a large extent, the phenomenology relevant to $b \rightarrow s\ell^+\ell^-$ decay modes is similar to that of multi-Higgs models. Model-dependent specifics can be seen in Ref. [124] for extended technicolor and in Ref. [125] the topcolor flavor signals were extensively studied. In most cases the power of $b \rightarrow s\gamma$ to constrain the masses and couplings of these scalar states is limited due to the possibility of cancellations. Modes such as $B \rightarrow K^*\ell^+\ell^-$ will be much more constraining.

7.2 Rare Decays: Experiment

7.2.1 Rare Decays at D0

We have investigated D0 options to study several rare B-decay processes in Run II:

- $B_d^0 \rightarrow K^{*0}\mu^+\mu^-$ decay followed by $K^{*0} \rightarrow K^\pm\pi^\mp$, with the expected combined branching ratio of $0.67 \times 1.5 \times 10^{-6}$.
- inclusive $b \rightarrow s\mu^+\mu^-$ decay with the expected SM branching ratio of 6×10^{-6} .
- exclusive $B_s^0 \rightarrow \mu^+\mu^-$ decay, with the expected SM branching ratio of 4×10^{-9} .

With its extended muon coverage and excellent muon identification, D0 can easily trigger on the semileptonic decay of B mesons into muons. In particular, we expect that the dimuon trigger, with an effective transverse momentum (p_T) threshold for individual muons of 1.5-2 GeV/c in the pseudorapidity range $|\eta^\mu| < 1.6$, will run unrescaled even at the highest luminosities. Thanks to the installation of the central and forward preshowerers in Run II, D0 will also be able to trigger on low p_T dielectrons. However, because of the limited bandwidth available at the level one (10 kHz) and level two (1 kHz) of the current trigger system, the rate of low threshold lepton triggers could become unacceptable. We are protecting ourselves against this possibility by adding a level 2 trigger preprocessor using the data from the Silicon Vertex Detector (SMT). The processor will allow to trigger on events containing tracks with large impact parameters in the transversal plane, coming from the decay of B/D mesons.

Various trigger combinations and kinematic cuts have been considered to optimize selection of the rare decay processes. The expected numbers of events are quoted for an integrated luminosity of $2 fb^{-1}$ and the B meson production cross section normalized to $\sigma(B_d^0) = 3.2\mu b$ for $p_T^B > 6$ GeV, $|y(B)| < 1$. The combined trigger efficiency for the proposed dimuon and the single muon trigger is 55% for events with two muons with $p_T^\mu > 1.5$

GeV/c, $|\eta^\mu| < 1.6$, and $p_T^{\mu\mu} > 5$ GeV/c. We have verified that, with these kinematic cuts, trigger efficiency is independent of the dimuon mass.

We found in our Run I analysis [129] that for the inclusive $B \rightarrow X_s \mu^+ \mu^-$ decay it would be necessary to restrict the search to a limited dimuon mass range of (3.9-4.4) GeV, representing $\approx 7\%$ of the decays [130], in order to avoid the sequential decays $B \rightarrow D + \mu + X_1$; $D \rightarrow \mu + X_2$ and J/ψ and $\psi(2s)$ resonances. However, even in this limited dimuon mass window, we expect only 1000 signal events compared to 100,000 $Q\bar{Q} \rightarrow \mu^- \mu^+ + X$ physics background events, with muons originating from two different b quarks. Some additional kinematic cuts on the event topology and multivertex searches could improve the signal to background ratio, however, it does not seem worth the effort. There is only a limited interest in measuring the small and least theoretically known part of the dimuon mass spectrum.

The process $B_s^0 \rightarrow \mu^+ \mu^-$ is also rather hopeless to measure, unless the branching ratio is boosted by some additional, non SM contributions, like Higgs doublet exchanges. We expected fewer than 5 recorded $B_s^0 \rightarrow \mu^+ \mu^-$ events in 2 fb^{-1} of data.

On the other hand, D0 has a fair chance to make a competitive measurement of the $B_d^0 \rightarrow K^{*0} \mu^+ \mu^-$ decay, including the rate, and the decay asymmetry dependence on the dimuon mass. We have generated relevant Monte Carlo events combining the ISAJET production information with the predicted decay distributions, taken from Ref. [141]. A simple analysis of the Monte Carlo events was based on the CDF experiences from their attempt to isolate this channel in the Run I data [132,140]. Details of the investigations are described in the next sections.

7.2.1.1 Monte-Carlo Samples

This study is based on various Monte-Carlo samples generated with the ISAJET program at $\sqrt{s} = 2$ TeV, with events selected by the presence of two muons in the final state. Only a small sample of events has been processed through the current D0 event simulator, D0RECO and the current Level 1 trigger simulator. For the remaining events, the detector response was simulated using an older version of the muon trigger simulator.

The physics background is primarily due to $Q\bar{Q} \rightarrow \mu\mu X$ events, where Q stands for a c or b quark. A large sample of such events was generated with the NLO-QCD ISAJET version 7.22 in FOUR bins of p_T^b : (2–3) GeV/c, (3–5) GeV/c, (5–10) GeV/c, and (5–80) GeV/c. Only 80K events with 2 muons satisfying the acceptance cuts $p_T^\mu > 1.5$ GeV/c and $|\eta^\mu| < 2$ were kept for Geanting. We compared the p_T^b differential spectrum for all events, $d\sigma^b/dp_T^b$, to the MNR [131] prediction and renormalized the ISAJET weights to match the MNR p_T^b and p_T^c spectra. In addition, the absolute normalization of this sample was done using the CDF measurement of $b \rightarrow J/\psi$ production cross section at 1.8 TeV [133], extrapolated to the c.m. energy of 2 TeV (cross section increased by 25%). A smaller sample of $Q\bar{Q} \rightarrow \mu\mu X$, again in the p_T^b ranges from 2 GeV/c to 80 GeV/c, was generated with ISAJET 7.37 to confirm previous results.

The expected dimuon mass distribution due to $Q\bar{Q}$ production is shown in Fig. 7.9 for events with both muons satisfying the conditions $p_T^\mu > 1.5$ GeV/c and $|\eta^\mu| < 1.6$. The dimuon mass spectrum for muons originating from different b quarks is relatively flat

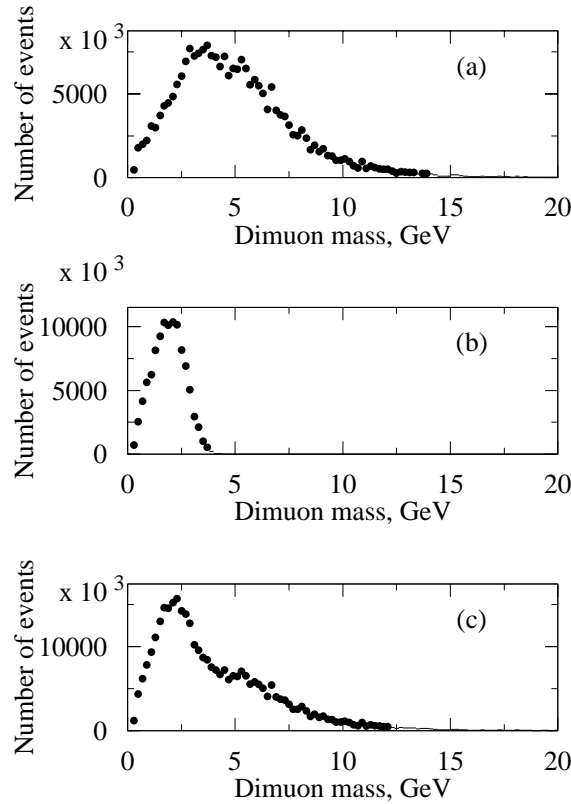


Figure 7.9: Expected number of dimuon events in $2 fb^{-1}$ of data, due to $Q\bar{Q}$ production, as a function of the dimuon mass for muons with $p_T^{\mu\mu} > 2.0$ GeV/ c , $p_T^\mu > 1.5$ GeV/ c and $|\eta^\mu| < 1.6$: (a) muons from different b quarks, (b) sequential b quark decays, and (c) total. Trigger and reconstruction efficiencies are not included. Events were generated with ISAJET V7.22 and normalized to the MNR differential p_T^Q distributions with the absolute normalization based on the measured $b \rightarrow J/\psi + X$ cross section.

between 2 GeV and 7 GeV, where the dominant process is the gluon splitting into $b\bar{b}$ pairs (Fig. 7.9 (a)). The mass spectrum resulting from sequential $b \rightarrow c \rightarrow s$ quark decays has a maximum around $m_{\mu\mu} = 2$ GeV and does not extend beyond the $m_{\mu\mu} = 4$ GeV (Fig. 7.9 (b)).

The signal samples of events were generated with ISAJET 7.37, using the leading order only and a single p_T^b bin between 2 and 80 GeV/ c . ISAJET decays B_d^0 mesons into $K^*\mu^+\mu^-$ system according to the three-body phase space. Therefore ISAJET events had to be weighted to match expected decay spectra, as calculated in Ref. [141]. The event weight depends on two observables: the dimuon mass and the energy of the negative muon in the B_d^0 rest frame. We have verified that the distributions of weighted Monte Carlo events are consistent with predictions of Ref. [141]. The expected non-resonant dimuon mass distributions for the $B_d^0 \rightarrow K^{*0}\mu^+\mu^-$ process from phase space and those predicted by the theory are shown in Fig. 7.10 (a). The predicted asymmetry plot is shown in Fig. 7.10 (b).

The primary vertex position was generated at $(0,0,z_0)$, with z_0 following a Gaussian

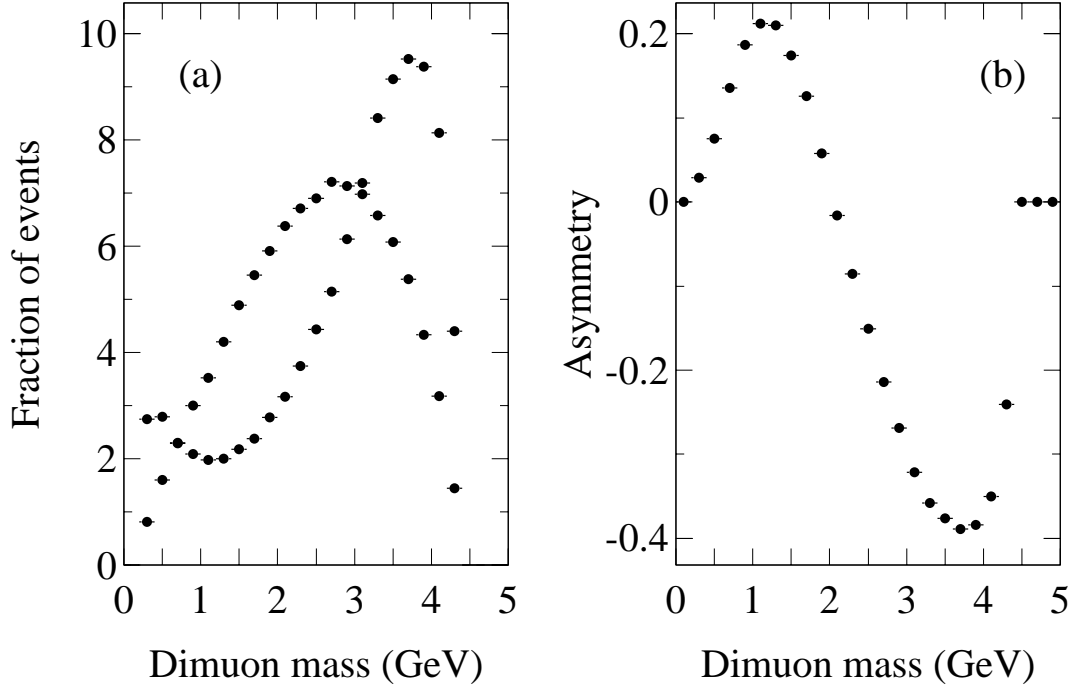


Figure 7.10: Comparison of the expected non-resonant dimuon mass distributions for the $B_d^0 \rightarrow K^{*0} \mu^+ \mu^-$ process from phase space and predicted by theory (a). Predicted asymmetry as a function of dimuon mass (b).

distribution with a width of 25 cm.

The combined single muon/dimuon trigger rates at the instantaneous luminosity of $2 \cdot 10^{32} \text{ cm}^{-2} \text{ s}^{-1}$ due to dimuons from the genuine $Q\bar{Q}$ signal are ≈ 13 Hz (≈ 4 Hz for $p_T^{\mu\mu} > 5$ GeV/c). The 13 Hz combines contributions from: $c\bar{c}$ pair production (2.5 Hz), $b\bar{b}$ pair production (9.5 Hz) and $b \rightarrow J/\psi + X$ decays (1.0 Hz). A requirement of $p_T^{\mu\mu} > 2$ GeV/c reduces the rate to 9 Hz (see Chapter 4.5.2).

It turns out that there is little trigger efficiency dependence on the dimuon mass for events selected with kinematic cuts used in this analysis. This is illustrated in Fig. 7.11, where we plot results of our investigations from early 1998. Therefore, muon/dimuon trigger efficiencies for the inclusive $b \rightarrow J/\psi$ production, discussed in Chapter 4.5.3 apply to the entire $B_d^0 \rightarrow K^{*0} \mu^+ \mu^-$ sample and the trigger does not significantly distort the dimuon spectrum once the kinematic cuts are introduced.

7.2.1.2 The Exclusive Channel $B_d^0 \rightarrow K^{*0} \mu^+ \mu^-$

In this section we summarize results for the process $B_d^0 \rightarrow K^{*0} \mu^+ \mu^-$ with $K^{*0} \rightarrow \pi^\pm K^\mp$. Expected numbers of events were obtained under the following assumptions:

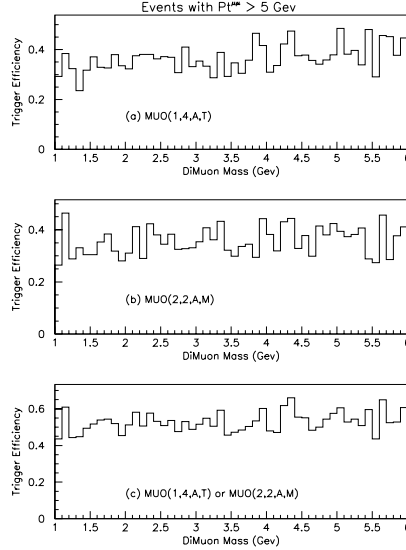


Figure 7.11: Trigger rate dependence on the dimuon mass for events preselected with kinematic cuts $|\eta^\mu| < 1.6$, $p_T^\mu > 1.5$ GeV/c and $p_T^{\mu\mu} > 5$ GeV/c. These results were obtained with the Sep. 97 version of the muon trigger simulator.

- integrated luminosity of $2 fb^{-1}$
- production cross section normalized to $\sigma(B_d^0) = 3.2\mu b$ for $p_T^B > 6$ GeV, $|y(B)| < 1$. This assumption results in the predicted number of produced B_d^0 or \bar{B}_d^0 equal to 1.4×10^{11} , the same number as obtained assuming $\sigma_{b\bar{b}} = 100\mu b$ and $B(\bar{b} \rightarrow B^0) = 0.35$ (see also Tables 6.4 and 7.8).
- B_d decay branching ratio $B(B_d^0 \rightarrow K^{*0} \mu^+ \mu^-) = 1.5 \times 10^{-6}$ and $B(K^{*0} \rightarrow \pi^\pm K^\mp) = 0.67$.
- two muons with $p_T^\mu > 1.5$ GeV/c and $|\eta^\mu| < 1.6$
- dimuon pair transverse momentum $p_T^{\mu\mu} > 5.0$ GeV/c.
- Level 1 trigger efficiencies for a combined trigger L1MU(2,2,A,M) and L1MU(1,4,A,T) as discussed in Chapter 4.5.3 (Table 4.1). Level 2 and Level 3 trigger efficiencies are unknown at the time of this writing and are set to 1.0.
- track reconstruction efficiency of 95% per track (81% per event).

Analysis cuts included:

- primary - secondary vertex separation in the transverse plane of $400 \mu m$
- charged particles from the $K^{*0} \rightarrow \pi^\pm K^\mp$ decay with transverse momenta: $p_T^{\pi(K)} > 0.5$ GeV/c and $|\eta^{\pi(K)}| < 1.6$

$p_T^{\mu\mu} >$	5.0 GeV/c	5.0 GeV/c
$p_T^\mu >$	1.5 GeV/c	3.0 GeV/c
Muon (dimuon) kinematic acceptance, ϵ_μ	0.052	0.014
Level 1 trigger efficiency, ϵ_{Lev1}	0.55	0.67
Level 2 & 3 trigger efficiency, ϵ_{Lev23}	1.00	1.00
Number of recorded events	4000	1350
$\epsilon_{analysis}$	0.17	0.22
ϵ_{reco}	0.81	0.81
Number of reco. events prior to the IP cuts	550	250
IP signif. > 2 for at least 3 tracks	490	220
IP signif. > 2 for all 4 tracks	310	130

Table 7.5: Expected numbers of events for the $B_d^0 \rightarrow K^{*0} \mu^+ \mu^-$ process with different analysis cuts.

- K^{*0} transverse momentum > 2 GeV/c
- dimuon invariant mass outside the J/ψ ((3.05 – 3.15) GeV) or $\psi(2s)$ ((3.62 – 3.76) GeV) mass windows.
- isolation $I > 0.6$, where I is the transverse momentum of the B candidate divided by the scalar sum of transverse momenta of the B and all other tracks. CDF has established efficiency for this cut as 0.92 ± 0.06 [140].
- the transverse plane impact parameter significance > 2 requirement for either three out of four tracks or all four tracks from the $B_d^0 \rightarrow K^{*0} \mu^+ \mu^-$ decay.

Table 7.5 lists expected event rates for various kinematic cuts. The inclusion of the $B_d^0 \rightarrow e^+ e^- K^*$ decay mode could result in a 50% increase in the number of observed events.

As an illustration, the dimuon mass distribution for the reconstructed sample of 630 events is shown in Fig. 7.12(a). The minima in the distribution are due to the removal of the J/ψ and $\psi(2s)$ mass bands. A corresponding plot, assuming a 1:1 signal to background ratio, is shown in Fig. 7.12 (c). The background was distributed according to the three body phase space and its rate estimate is based on the CDF extrapolations from their run I experience. An independent MCFAST Monte Carlo background evaluation has not yet been completed.

We conclude that the number of expected events, combined with relatively modest background level, will enable D0 to establish the signal and to measure its $q^2 = m_{\mu\mu}^2$ dependence. However, the numbers quoted in Table 7.5 represent an optimistic scenario, based on the D0 nominal trigger and track reconstruction efficiencies. A reduction in the per track reconstruction efficiency from 95% to 88% (a value used by CDF) and an inclusion of a Level 2&3 trigger efficiency of 50% (the STT preprocessor - see Chapter 4.5.4) would drop the number of expected events listed in Table 7.5 by a factor of three. The clue to a

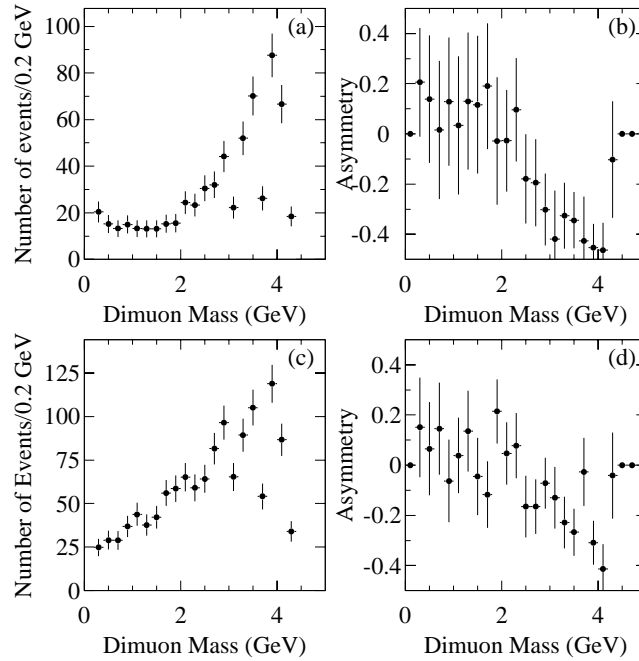


Figure 7.12: (a) Dimuon mass distribution in decay $B_d^0 \rightarrow K^{*0} \mu^+ \mu^-$, and (c) assuming 1:1 signal to background ratio. (b) Predicted asymmetry signal as function of dimuon mass, and (d) assuming the background level as in (c).

successful measurement of the $B_d^0 \rightarrow K^{*0} \mu^+ \mu^-$ process with the D0 detector is our claimed ability to trigger on low mass dimuons over large rapidity range.

The $B_d^0 \rightarrow K^{*0} \mu^+ \mu^-$ process is expected to exhibit an asymmetry in the $\cos\theta$ distribution, where θ is the μ^+ decay angle between the direction of the B_d and the direction of μ^+ in the rest frame of the $\mu^+ \mu^-$ rest frame. This asymmetry manifests itself as a difference in the energy distributions of μ^+ and μ^- in the B_d rest frame, at a given dimuon mass. The asymmetry is expected to vary with the dimuon mass from approximately 0.2 at small masses to -0.4 around 3.5 GeV. The sign reversal of the asymmetry occurs at the dimuon mass of ≈ 2 GeV and turns out to be relatively model independent.

The predicted asymmetry signal as a function of the dimuon mass for the same sample of events is shown in Fig. 7.12(b). A related plot, assuming a 1:1 signal to background ratio, is shown in Fig. 7.12 (d). The observed asymmetries, corrected for the assumed background contribution are 0.13 ± 0.13 and -0.31 ± 0.06 for $m_{\mu\mu} < 2$ GeV and $m_{\mu\mu} > 2$ GeV, respectively.

7.2.1.3 The Inclusive Decay $B \rightarrow X_s \ell^+ \ell^-$

This process, although theoretically the most interesting to measure, is very difficult to separate experimentally in hadronic collisions. The expected $\mu^+ \mu^-$ spectrum due to the heavy quark production is shown in Fig. 7.13 (onia states are removed). The muons are

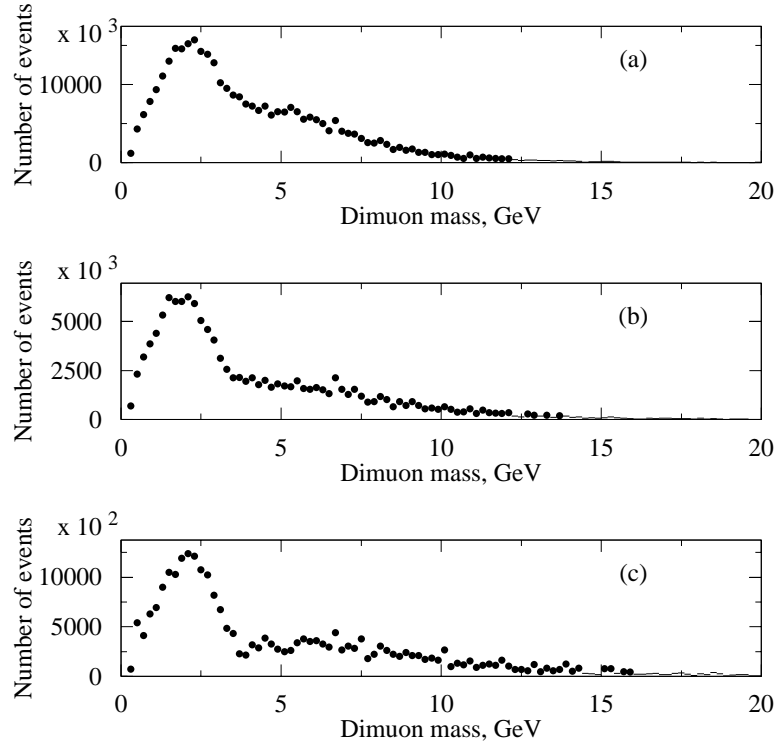


Figure 7.13: Expected dimuon mass distributions due to the non-resonant $Q\bar{Q}$ production. Both muons are required to have $p_T^\mu > 1.5$ GeV/c (3.0 GeV/c in (c)) and $|\eta^\mu| < 1.6$ and the dimuon p_T must be greater than: (a) 2 GeV/c, (b,c) 5 GeV/c. Trigger and reconstruction efficiencies are not included. Events were generated with ISAJET V7.22 and normalized to the MNR differential p_T^Q distributions with an absolute normalization based on the measured $b \rightarrow J/\psi + X$ cross section.

selected with transverse momenta greater than 1.5 GeV/c and $|\eta^\mu| < 1.6$. The mass region below 3.9 GeV is dominated by the sequential b-quark decays, for which one of the muon tracks originates from the B hadron vertex, whereas the other from the charm decay vertex. At larger masses muon pairs are produced predominantly by semi leptonic decays of b and \bar{b} quarks with the $b\bar{b}$ pair resulting from a gluon splitting. Therefore the muon tracks are expected to point to two different vertices.

The expected dimuon mass spectrum for the $B \rightarrow X_s \mu^+ \mu^-$ process smeared by the expected experimental resolution is shown in Fig. 7.14. The dimuon mass range (3.9 - 4.4) GeV represents only 7% of the spectrum (expected number of events is 30 % larger for $(3.8 < m(\mu\mu) < 4.4)$ GeV). The dominant $Q\bar{Q}$ physics background could be slightly reduced by increasing the required transverse momentum of the muon pair, as shown in Fig. 7.13. Imposing kinematic cuts similar to those described for the $B_d^0 \rightarrow K^{*0} \mu^+ \mu^-$ analysis leads to the expected number of events listed in the Table 7.6. The numbers are quoted for the assumed branching ratio for the $B \rightarrow X_s \mu^+ \mu^-$ decay of 6×10^{-6} .

The signal is overwhelmed by the physics background, with a 1:1000 ratio. The back-

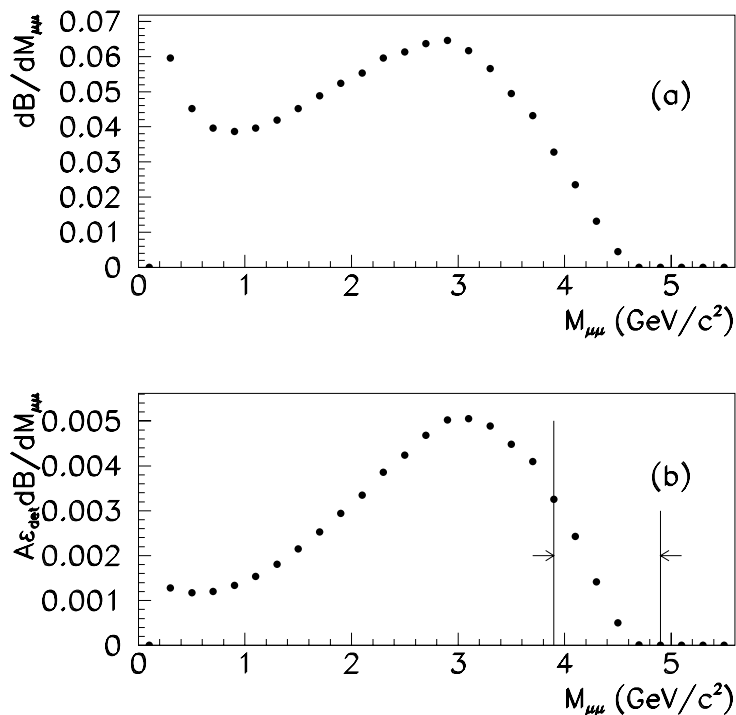


Figure 7.14: The calculated differential branching fraction for the decay $B \rightarrow X_s \mu^+ \mu^-$, as a function of $m_{\mu\mu}$. (b) the same differential branching fraction modified by the response of the D0 detector. The arrows indicate the search window used in this analysis.

$p_T^{\mu\mu}$	$> 2.0 \text{ GeV}/c$	$> 5.0 \text{ GeV}/c$	$> 5.0 \text{ GeV}/c$
p_T^μ	$> 1.5 \text{ GeV}/c$	$> 1.5 \text{ GeV}/c$	$> 3.0 \text{ GeV}/c$
Trigg. effic. (%)	32	55	67
Recorded	2300	1750	1000
Vtx separation cut of $400 \mu\text{m}$	1200	1050	650
$b\bar{b}$ Bkgd (no analysis cuts)	1,900,000	400,000	100,000

Table 7.6: Expected number of recorded $B \rightarrow X_s \mu^+ \mu^-$ events in the mass window $3.9 < m_{\mu\mu} < 4.4 \text{ GeV}$ with different analysis cuts.

$p_T^{\mu\mu}$	$> 2.0 \text{ GeV}/c$	$> 5.0 \text{ GeV}/c$	$> 5.0 \text{ GeV}/c$
p_T^μ	$> 1.5 \text{ GeV}/c$	$> 1.5 \text{ GeV}/c$	$> 3.0 \text{ GeV}/c$
Signal events after cuts	6	3	1.5

Table 7.7: Expected number of $B_s^0 \rightarrow \mu^+\mu^-$ events.

ground estimates are based on the ISAJET 7.37 version. The earlier ISAJET versions, like V7.22, predict the background level twice as large. Additional cuts on the event topology and a requirement of a common muon vertex will reduce the background by factors 3-10, not sufficient to establish the $B \rightarrow X_s \mu^+ \mu^-$ signal.

7.2.1.4 The Exclusive Channel $B_s^0 \rightarrow \mu^+ \mu^-$

The expected number of events for the $B_s^0 \rightarrow \mu^+ \mu^-$ mode is summarized in Table 7.7. We assume that B_s mesons are produced with a rate equal to 40% of that for B_d mesons [138]. The quoted numbers are for the $B_s^0 \rightarrow \mu^+ \mu^-$ branching ratio of 4×10^{-9} . The analysis cuts include: (i) the B_s isolation cut, $I > 0.6$, (ii) the requirement that the transverse decay length in the B_s rest frame exceeds $100 \mu\text{m}$, and an impact parameter significance for each muon track greater than 2. A 95% reconstruction efficiency per track is also assumed.

With the expected number of events there are limited chances to measure this branching ratio, unless its actual value is significantly boosted up by some non-SM processes. The background rates have not yet been estimated.

7.2.2 Rare Decays at CDF

In Run 1I CDF expects to collect a large enough b sample to observe rare b decays with branching ratios of order 10^{-6} , including $b \rightarrow s\gamma$ (radiative) decays and $b \rightarrow s\mu\mu$ decays. In this section, we describe the prospects for CDF in Run 1I for measurements in several channels: $B_{d,s} \rightarrow K^{*0}\gamma$, $\Lambda_b \rightarrow \Lambda\gamma$, $B_d \rightarrow K^{*0}\mu\mu$, and $B_{d,s} \rightarrow \mu\mu$. We will discuss trigger selections for these channels and estimates signal yields. We also study the potential to measure the forward-backward asymmetry A_{FB} in the $B_d \rightarrow K^{*0}\mu\mu$ decays and show some ideas to extract the zero position of A_{FB} as a function of $M_{\mu\mu}$.

7.2.2.1 Radiative B Meson Decays

BaBar and Belle are expected to observe approximately 20 $B \rightarrow K^*\gamma$ decays per 1 fb^{-1} of $\Upsilon(4S)$ data. Each experiment plans to obtain or order 100 fb^{-1} within 3 years ($1000 B \rightarrow K^*\gamma$). However, these projections are recently getting much better, and each experiment may obtain several 100 fb^{-1} of data by 2004. Our goal is to implement a trigger to collect of order $1000 B \rightarrow K^*\gamma$ events during Run 1I. Our studies of radiative decays of B_s and Λ_b are unique to the Tevatron.

In Run 1, CDF included a dedicated trigger for radiative b decays, searching for a photon associated with a nearby pair of tracks [135]. In this trigger, we required two energetic oppositely-charged tracks, each with $p_T > 2$ GeV/ c , in the vicinity of the photon. We collected 22.3 pb^{-1} of data in Run 1B with $E_T(\gamma) > 10$ GeV, and 6.6 pb^{-1} in Run 1C with $E_T(\gamma) > 6$ GeV and obtained upper limits on the branching fractions for B_d and B_s radiative decays to be 1.6×10^{-4} and 2.5×10^{-4} , respectively. Another search for radiative b decays used photon conversions. One of the conversion electrons was triggered with an 8 GeV threshold [136,137]. The two methods had similar acceptance after all cuts, but because it relied on tracking information to reconstruct the photon, the conversion method had superior B -mass resolution and a more straightforward analysis procedure. Also, the conversion method has a ready normalization in the kinematically similar $B^0 \rightarrow J/\psi K^{*0}$, $J/\psi \rightarrow e^+e^-$ mode.

In order to trigger on radiative B meson decays, we can take advantage of the long lifetime of b hadrons and use the SVT track processor to find charged-particle tracks significantly displaced from the beamline. We will use the same trigger selection as for semileptonic decays discussed in Section 7.5.1, requiring a 4 GeV electron associated with a track of $p_T > 2$ GeV/ c found by the SVT to have an impact parameter d_0 greater than $120 \mu\text{m}$. Furthermore, we require the angle between the electron and track to be less than 90° and the transverse mass to be less than $5 \text{ GeV}/c^2$. Because of the lower electron threshold, after kinematic cuts made in the Run I analysis to purify the sample, this trigger selection has about a factor of 3 greater acceptance for radiative decays than the inclusive 8 GeV electron requirement that was used in Run I but with a substantially lower trigger rate. The rate for the same-side electron plus displaced track selection is expected to be 9 Hz at a luminosity of $10^{32} \text{ cm}^{-2} \text{ s}^{-1}$.

An estimate of the signal yield for $B_d \rightarrow K^{*0}\gamma$ is obtained by scaling the Run 1 analysis results with the ratio of the acceptances between Run 1 and Run 1I. The Run 1 analysis yield can be described as [137],

$$N(\text{Run I}) = \frac{Br(B_d \rightarrow K^{*0}\gamma)}{(4.36 \pm 1.13) \times 10^{-5}}. \quad (7.74)$$

The expected signal yield of the Run 1 analysis was 1.03 ± 0.17 events with $Br(B_d \rightarrow K^{*0}\gamma) = 4.5 \times 10^{-5}$. To calculate the acceptance ratio between Run 1 and Run 1I, we require all the tracks (e^+ , e^- , K^+ , and π^-) to have $p_T > 400$ MeV/ c and to pass through the full tracking volume to ensure high resolution and reconstruction efficiency. We also require the same offline selection cuts as the Run 1 analysis ($ct(B) > 100 \mu\text{m}$ and $|d_0(K, \pi)| > 4.5\sigma = 100 \mu\text{m}$). We correct for the improved SVX acceptance in Run II and the relative efficiencies of the Run I and Run II track processors, and we assume the SVT tracking efficiency to be 0.88 per track. We also assume the photon conversion probability before the central drift-chamber tracking volume to be 6% in Run 1 and 8% in Run 1I. Other efficiencies are assumed to cancel in the ratio. For the $B_s \rightarrow K^{*0}\gamma$ channel, we expect the branching fraction to be scaled by $|V_{td}|^2/|V_{ts}|^2 \sim 0.16$ relative to $Br(B_d \rightarrow K^{*0}\gamma)$, and the ratio of the production rates for B_s and B_d mesons is $f_s/f_d = 0.426 \pm 0.07$ [138]. Thus the expected yield is

$$N(B_s \rightarrow K^{*0}\gamma) \sim \frac{f_s |V_{td}|^2}{f_d |V_{ts}|^2} N(B_d \rightarrow K^{*0}\gamma) \sim 0.07 \times N(B_d \rightarrow K^{*0}\gamma). \quad (7.75)$$

For the same-side 4 GeV electron plus displaced track selection, we expect the following signal yields after all cuts:

$$N(B_d \rightarrow K^{*0}\gamma) = (170 \pm 40) \times \frac{\int \mathcal{L} \text{ (fb}^{-1}\text{)}}{2 \text{ fb}^{-1}} \times \frac{Br(B_d \rightarrow K^{*0}\gamma)}{4.5 \times 10^{-5}} \quad (7.76)$$

$$N(B_s \rightarrow K^{*0}\gamma) = (12 \pm 4) \times \frac{\int \mathcal{L} \text{ (fb}^{-1}\text{)}}{2 \text{ fb}^{-1}} \times \frac{Br(B_d \rightarrow K^{*0}\gamma)}{4.5 \times 10^{-5}}. \quad (7.77)$$

Note that lowering the electron threshold to 3 GeV would increase the acceptance by about 50% but would lead to significantly higher trigger rates.

7.2.2.2 Radiative b Baryon Decays

Since the Λ baryon has a long lifetime ($c\tau = 8$ cm), most of the Λ decays from $\Lambda_b \rightarrow \Lambda\gamma \rightarrow p\pi ee$ events are expected to be outside of the SVX fiducial volume, so there would be a low probability for the proton from the Λ to be reconstructed by the SVT. A way to trigger on this channel is to find an electron from the conversion and find a displaced track that originates from the opposite b quark. This electron plus opposite-side displaced track selection is also described in detail in Section 7.5.1. We would require an electron with a 4 GeV threshold and a displaced track found by the SVT with $p_T > 2$ GeV/ c and $d_0 > 120 \mu\text{m}$ with a large opening angle between the two ($\Delta\phi > 90^\circ$) and transverse mass $M_T > 5$ GeV/ c^2 such that the electron and track not come from the decay of a single b hadron.

The expected yield for the Run I $\Lambda_b \rightarrow \Lambda\gamma$ search can be summarized in terms of the acceptance as [139],

$$N(\text{Run I}) = \frac{Br(\Lambda_b \rightarrow \Lambda\gamma)}{(2.80 \pm 0.95) \times 10^{-4}}. \quad (7.78)$$

Thus the expected signal events of the Run I analysis is 0.16 ± 0.06 events with $Br(\Lambda_b \rightarrow \Lambda\gamma) = 4.5 \times 10^{-5}$. To calculate the acceptance ratio between Run I and Run II, we require all the tracks (e^+ , e^- , p , and π^-) to have $p_T > 400$ MeV/ c and pass through the full tracking volume.

In the Run I analysis, we required $p_T(\Lambda) > 4$ GeV/ c for the Λ decays reconstructed without SVX tracks and $p_T(\Lambda) > 2$ GeV/ c with $|d_0(\Lambda)| > 70 \mu\text{m}$ for those reconstructed with SVX tracks. For the Run II estimate, the Λ is required to decay before the ISL (Radius < 20 cm) to improve signal purity. This allows us to lower the $p_T(\Lambda)$ threshold to 2 GeV/ c . The opposite-side SVT track required to be in the tracking fiducial with $p_T > 2$ GeV/ c and $120 \mu\text{m} < |d_0| < 2$ mm. The signal yield with the opposite-side 4 GeV electron plus displaced-track trigger is found to be

$$N(\text{Run II}) = (5.0 \pm 2.1) \times \frac{\int \mathcal{L} \text{ (fb}^{-1}\text{)}}{2 \text{ fb}^{-1}} \times \frac{Br(\Lambda_b \rightarrow \Lambda\gamma)}{4.5 \times 10^{-5}}. \quad (7.79)$$

7.2.2.3 $B_d \rightarrow K^{*0} \mu \mu$ Decays

Because the trigger rate for dimuon events peaks at low $\mu\mu$ mass, to trigger on $J/\psi \rightarrow \mu^+ \mu^-$ decays at high luminosity, CDF expects to impose a cut on transverse mass $2 < M_T < 4 \text{ GeV}/c^2$ for J/ψ selections. However, the low-mass region is needed in the study of $B_d \rightarrow K^{*0} \mu \mu$ decays. Since the looser dimuon transverse mass window cut ($M_T < 5 \text{ GeV}/c^2$) for rare decays increases the Level 2 trigger rate by about factor of 4, we need further background reductions. We plan two complementary trigger options:

- Improving muon purity by requiring one of the trigger muons to be found in the outer (CMP) muon chambers
- Requiring there to be a track of $2.0 \text{ GeV}/c$ found to be displaced by the SVT with $|d_0| > 120 \mu\text{m}$.

In the second case, the SVT-selected track can be one of the two muons or a hadron track. We expect the combined trigger rate for the two selections to be about 10 Hz at a luminosity of $10^{32} \text{ cm}^{-2} \text{ s}^{-1}$.

The signal yield is obtained by using the same procedure as the radiative decays. The expected yield of the Run 1 analysis can be described as [140]

$$N(\text{Run I}) = \frac{Br(B_d \rightarrow K^{*0} \mu \mu)}{(1.65 \pm 0.33) \times 10^{-6}}, \quad (7.80)$$

and the expected signal events of the Run 1 analysis is 0.91 ± 0.18 events with $Br(B_d \rightarrow K^{*0} \mu \mu) = 1.5 \times 10^{-6}$. To calculate the acceptance ratio between Run 1 and Run 1I, we make the kinematic and geometric fiducial cuts as with the radiative decays. We also require the same offline selection cut as Run 1 analysis ($L_{XY}(B) > 400 \mu\text{m}$ and $|d_0(\mu, K, \pi)| > 2\sigma \simeq 50 \mu\text{m}$). We correct for the increased acceptance of the muon triggers in Run II. For the dimuon + SVT trigger, we assume the SVT tracking efficiency to be 0.88 per track. Any other efficiencies are assumed to be canceled in the ratio. Thus for an assumed branching ratio of 1.5×10^{-6} , in 2 fb^{-1} CDF expects to observe 44 ± 9 events with the tight muon selection and 36 ± 7 events with the dimuon plus SVT selection for a combined yield of 61 ± 12 events.

Forward-Backward Asymmetry

The Forward-Backward asymmetry in the $B_d \rightarrow \mu \mu K^{*0}$ decay is defined as

$$A_{FB} = \frac{N(\cos \Theta > 0) - N(\cos \Theta < 0)}{N(\cos \Theta > 0) + N(\cos \Theta < 0)} = \frac{N_F - N_B}{N_F + N_B} \quad (7.81)$$

where Θ is the angle between the direction of the B_d and the direction of the μ^+ in the rest frame of the $\mu^+ \mu^-$ system. Note that the definition for the B_d meson is the same as that for the \bar{B}_d meson so flavor tagging is not necessary to measure A_{FB} . In general A_{FB} depends on the decay kinematics. Standard Model calculations predict the distribution of

A_{FB} as a function of the dimuon mass to cross the zero around $\sqrt{s} = M_{\mu\mu} = 2 \text{ GeV}/c$. As discussed in Section 7.1.3.3, the A_{FB} distribution strongly depends on the $B \rightarrow K^*$ form factor; however, the zero position (M_0) is stable under various form-factor parameterizations. Figure 7.8 compares the A_{FB} distributions predicted by the Standard Model with several SUSY models. Some new physics models predict there to be no zero in the A_{FB} distribution.

Figure 7.15 shows the expected A_{FB} distributions with 50 and 400 $B_d \rightarrow K^{*0} \mu\mu$ events after all the trigger and offline requirements. The solid line in the figure corresponds to the Monte Carlo generated distribution.

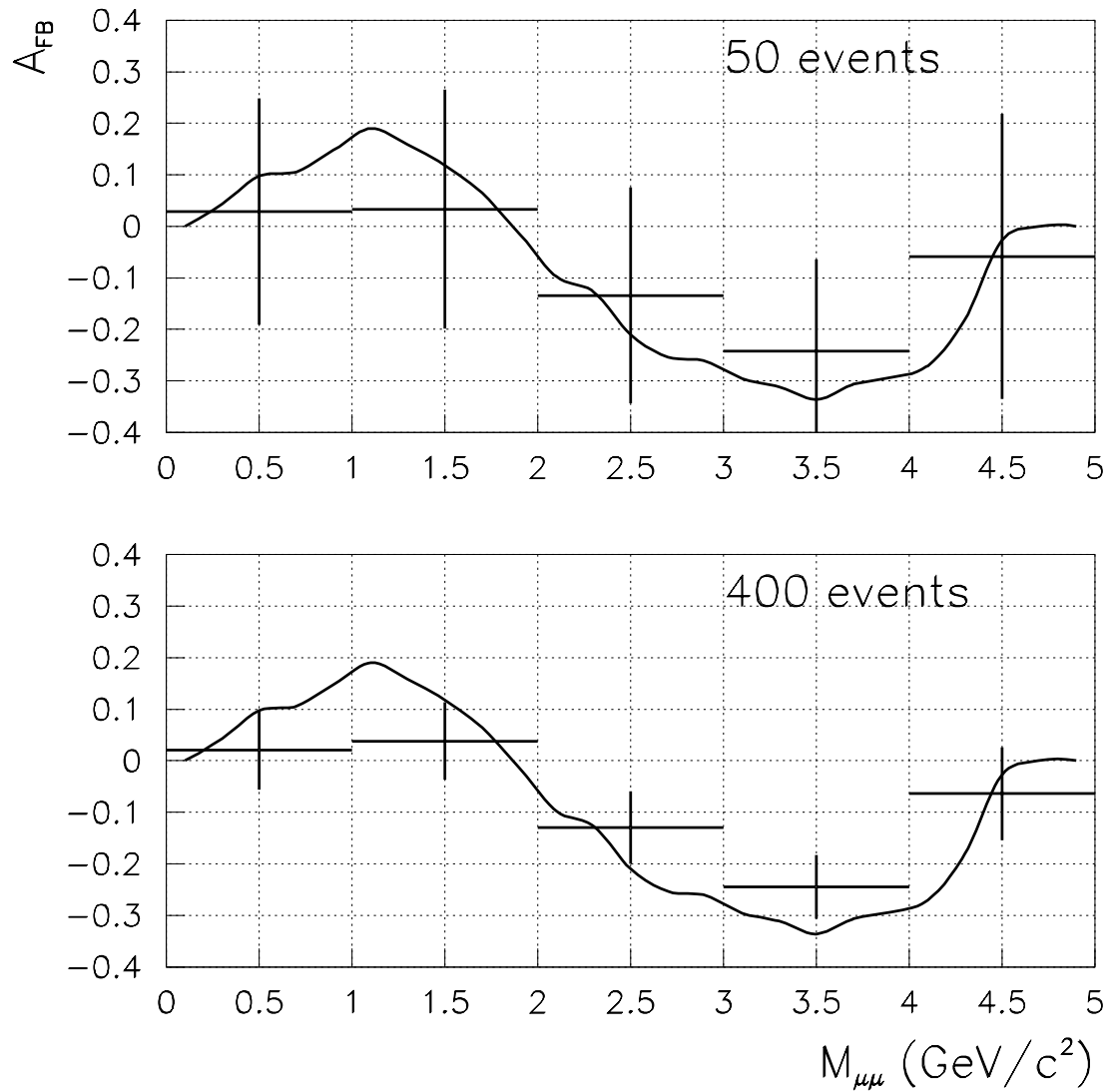


Figure 7.15: A_{FB} with 50 and 400 events of the $B_d \rightarrow K^{*0} \mu\mu$ signal and $S/B = 1$.

Asymmetry in Background Events

Figure 7.16 shows the A_{FB} distribution as a function of $M_{\mu\mu}$ for the background, estimated from the same dataset as the Run 1 $B_d \rightarrow K^* \mu\mu$ search [140]. We define four background regions,

- non- b SR : (non- b -like B mass signal region event),
- non- b SB : (non- b -like B mass side-band event),
- B mass b SR : (b -like B mass signal region event),
- B mass b SB : (b -like B mass side-band event),

where the cuts are defined as,

- non- b -like : prompt; specifically L_{XY} , $d_0(\mu)$, $d_0(K)$, and $d_0(\pi) < 1\sigma$,
- b -like : displaced; specifically $L_{XY} > 2\sigma$, and $d_0(\mu)$, $d_0(K)$, and $d_0(\pi) > 1\sigma$,
- signal region : $|M_{B_d} - M_{\mu\mu K\pi}| < 100 \text{ MeV}/c^2$,
- side-band : $100 \text{ MeV}/c^2 < |M_{B_d} - M_{\mu\mu K\pi}| < 600 \text{ MeV}/c^2$.

In the above σ indicates the r.m.s. uncertainty of each quantity. There is no significant forward-backward asymmetry in any of the background samples.

Extraction of A_{FB} Zero Point

To extract the zero-point of the asymmetry with respect to $M_{\mu\mu}$, we define the significance of A_{FB} as

$$\mathcal{S} = \frac{N_F - N_B}{\sqrt{N_F + N_B + N_{BG}}}. \quad (7.82)$$

We define a likelihood function to extract the zero position:

$$\mathcal{L} = \mathcal{S}(M_{\mu\mu} < M) - \mathcal{S}(M_{\mu\mu} > M) = \mathcal{S}^- - \mathcal{S}^+. \quad (7.83)$$

The likelihood is expected to be maximal at a mass M_0 where $A_{FB}(M_0) = 0$. Figure 7.17 shows the A_{FB} and likelihood distributions in a Monte Carlo sample of 10000 signal events and no background events. We repeated the same analysis for the case of 50 (400) signal events and a 1:1 signal-to-background ratio under the assumption there is no background asymmetry. The results are shown in Figure 7.18. The histograms show the distribution of M_0 values for 1000 trials with signal sizes of 50 and 400 events. The points are results for a generated samples with no forward-backward asymmetry. Therefore, it appears that it will be difficult to extract the asymmetry zero point after only 2 fb^{-1} in Run IIa, but the prospects are much more promising for 15 fb^{-1} in Run IIb. However, more work needs to be done on defining an asymmetry significance.

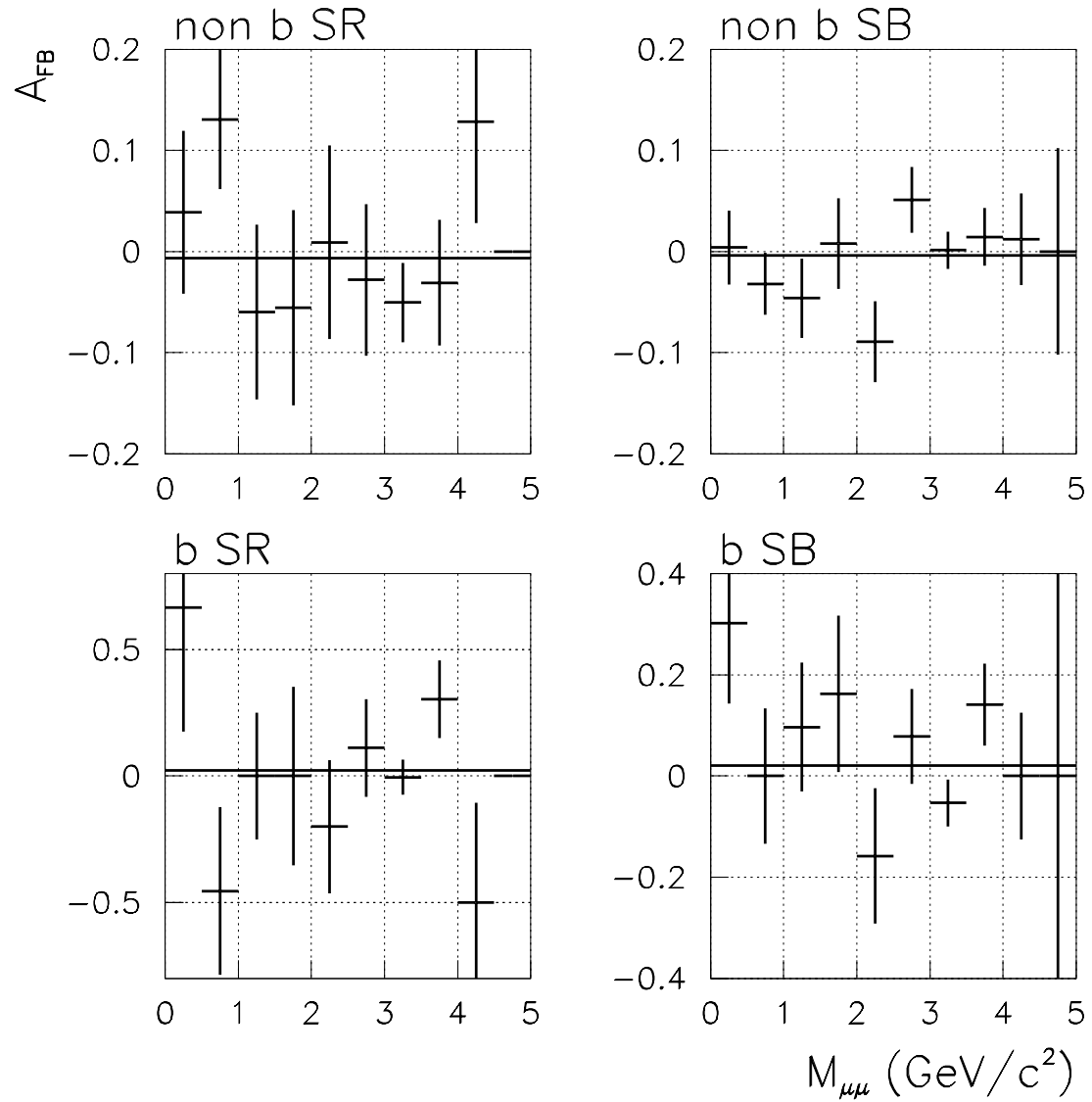


Figure 7.16: The forward-backward asymmetry for the background events obtained from the Run 1 data.

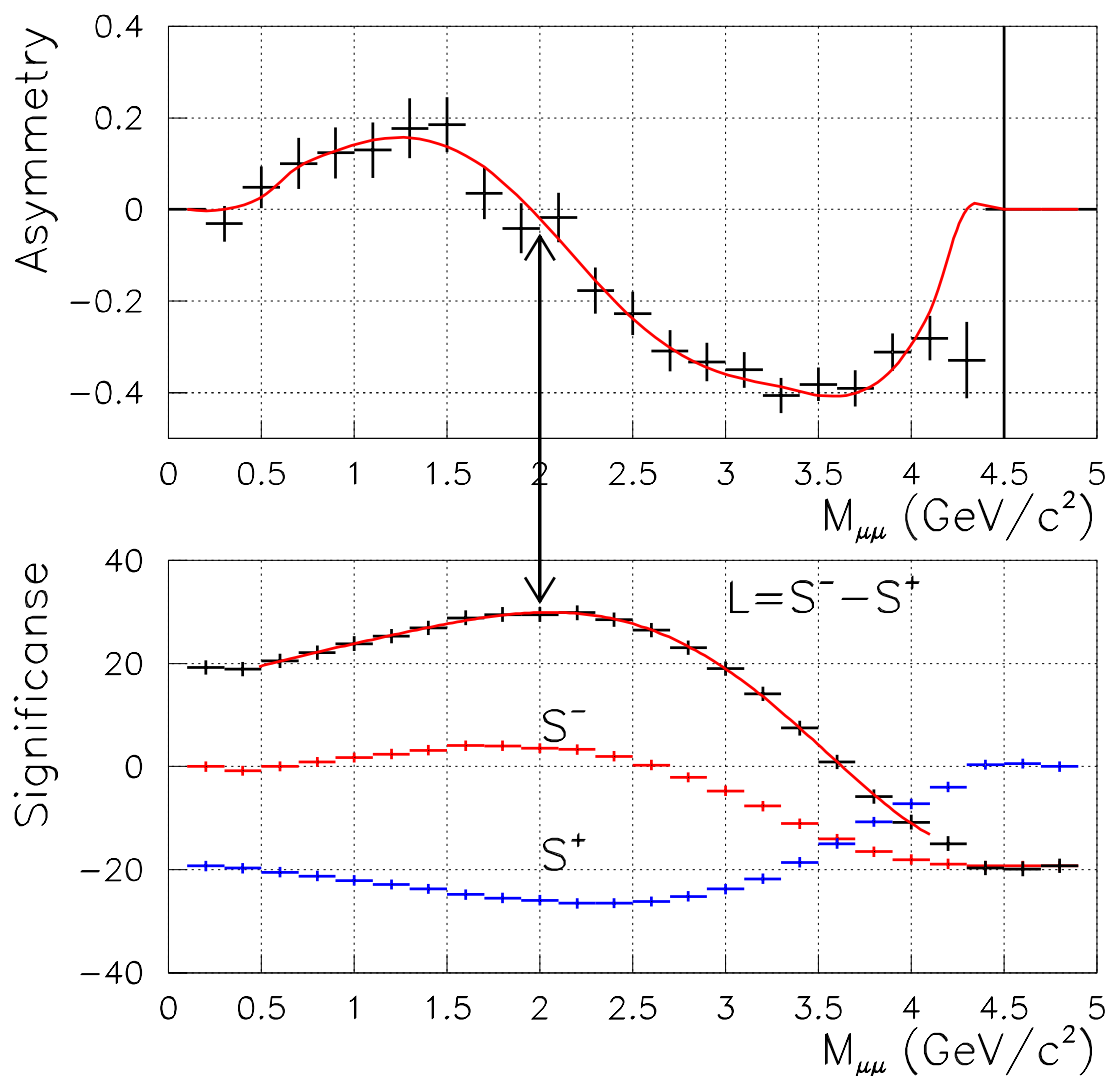


Figure 7.17: The forward-backward asymmetry in Ref [141], and a likelihood function for extracting the asymmetry zero-point M_0 .

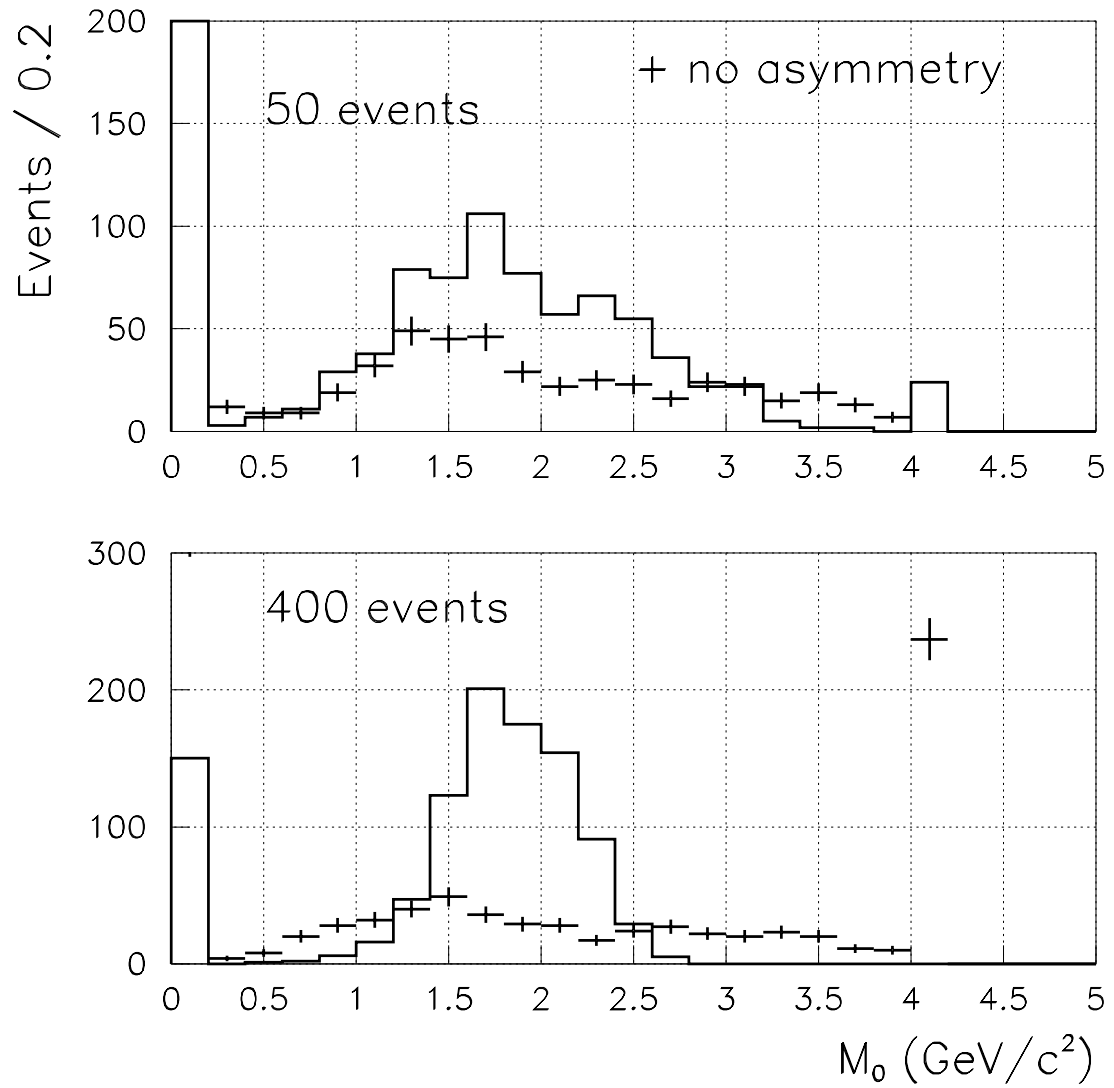


Figure 7.18: A_{FB} and M_0 with 1000 $B_d \rightarrow K^* \mu \mu$ events and $S/B = 1$.

7.2.2.4 $B \rightarrow \mu^+ \mu^-$

The dimuon triggers are also useful to study the two-body decay $B_{d(s)} \rightarrow \mu^+ \mu^-$. Since the Standard Model predicts the branching fraction of $B_d \rightarrow \mu^+ \mu^-$ to be much lower than the reach of CDF in Run II, we give an expected “single-event sensitivity” instead of the signal yield. Single-event sensitivity is defined as branching ratio for which we would expect to observe one event in 2 fb^{-1} .

The sensitivity is obtained by using the same procedure as the $B_d \rightarrow \mu\mu K^{*0}$ decays. The result of the Run 1 analysis is [140], b

$$\mathcal{S}(B_d \rightarrow \mu\mu) = (2.0 \pm 0.5) \times 10^{-7} \quad (7.84)$$

$$\mathcal{S}(B_s \rightarrow \mu\mu) = (6.0 \pm 1.6) \times 10^{-7}. \quad (7.85)$$

The Run II expectation is obtained by scaling the Run 1 sensitivity for the same trigger selections as CDF plans to use for $B^0 \rightarrow \mu^+ \mu^- K^{*0}$. Combining the results for the two trigger paths, we find the sensitivities to be

$$\mathcal{S}(B_d \rightarrow \mu\mu) = 3.5 \times 10^{-9} \times \frac{2 \text{ fb}^{-1}}{\int \mathcal{L} \text{ (fb}^{-1}\text{)}} \quad (7.86)$$

$$\mathcal{S}(B_s \rightarrow \mu\mu) = 1.0 \times 10^{-8} \times \frac{2 \text{ fb}^{-1}}{\int \mathcal{L} \text{ (fb}^{-1}\text{)}}. \quad (7.87)$$

Given the Standard model prediction B_d and B_s branching fractions of 1.5×10^{-10} and 3.5×10^{-9} respectively, we would expect a few $B_s \rightarrow \mu\mu$ signal in 15 fb^{-1} of Run IIb.

7.2.2.5 Summary

We have examined the sensitivity of Run II CDF for the four rare-decay modes $B_{d(s)} \rightarrow K^{*0} \gamma$, $\Lambda_b \rightarrow \Lambda \gamma$, $B_d \rightarrow K^{*0} \mu\mu$, and $B_{d(s)} \rightarrow \mu\mu$. The expected signal yields are obtained by scaling the results of the Run 1 analyses:

$$N(B_d \rightarrow K^{*0} \gamma) = (170 \pm 50) \times \frac{\int \mathcal{L}}{2 \text{ fb}^{-1}} \times \frac{Br(B_d \rightarrow K^{*0} \gamma)}{4.5 \times 10^{-5}}, \quad (7.88)$$

$$N(B_s \rightarrow K^{*0} \gamma) = (12 \pm 4) \times \frac{\int \mathcal{L}}{2 \text{ fb}^{-1}} \times \frac{Br(B_d \rightarrow K^{*0} \gamma)}{4.5 \times 10^{-5}}, \quad (7.89)$$

$$N(\Lambda_b \rightarrow \Lambda \gamma) = (4.0 \pm 1.7) \times \frac{\int \mathcal{L}}{2 \text{ fb}^{-1}} \times \frac{Br(\Lambda_b \rightarrow \Lambda \gamma)}{4.5 \times 10^{-5}}, \quad (7.90)$$

$$N(B_d \rightarrow K^{*0} \mu\mu) = (59 \pm 12) \times \frac{\int \mathcal{L}}{2 \text{ fb}^{-1}} \times \frac{Br(B_d \rightarrow K^{*0} \mu\mu)}{1.5 \times 10^{-6}}, \quad (7.91)$$

$$\mathcal{S}(B_d \rightarrow \mu\mu) = 3.5 \times 10^{-9} \times \frac{2 \text{ fb}^{-1}}{\int \mathcal{L}}, \quad (7.92)$$

$$\mathcal{S}(B_s \rightarrow \mu\mu) = 1.0 \times 10^{-8} \times \frac{2 \text{ fb}^{-1}}{\int \mathcal{L}}. \quad (7.93)$$

We also studied the forward-backward asymmetry in the $B_d \rightarrow K^{*0} \mu \mu$ decay and showed some ideas to extract the zero position of the A_{FB} distribution.

7.2.3 Rare Decays at BTeV

Because the Tevatron produces more than 10^{11} b hadrons per year, we should be able to observe some of these decays and to set stringent limits on others. The precise vertexing of the BTeV silicon pixel detector will allow us to easily differentiate b decays from non- b backgrounds in the Tevatron environment. We present the expected sensitivities from studies of some of these decay channels.

7.2.3.1 The Exclusive Channel $B^0 \rightarrow K^{*0} \mu^+ \mu^-$

Since we expect large backgrounds under the signal, an understanding of these backgrounds is critical to understanding our sensitivity. The various sources of background are:

- b -events where portions of the two b hadrons in the event appear to form a vertex downstream of the production point. In approximately 1% of all $b\bar{b}$ events both B hadrons decay semileptonically producing two real muons. In addition, there is a charged kaon in at least one of the b 's over 90% of the time.
- Minimum bias events where three particles conspire to fake a secondary vertex and two of the particles either decay downstream of the magnet or make hadronic showers which leave a signal in the muon detector (hadron punch-through).
- Charm events with one or more real muons and kaons.
- More generally, any admixture of b , charm, minimum bias events, primary interactions and secondary decays, combined with hadronic punch-through.
- Decays from single B mesons where two charged pions fake muons.

The basic weapons to combat these backgrounds are:

- Excellent discrimination between the primary and secondary vertex, which eliminates backgrounds from minimum bias events and from the underlying event within a true b event. Tracks which are not part of the b vertex are easily rejected by requiring a non-zero vertex fit probability, as shown in Fig. 7.19(a). Also, the normalized decay length (L/σ_L), shown in Fig. 7.19(c), provides additional discrimination against background.
- Excellent mass resolution (of order 17 MeV) on the final state, as shown in Fig. 7.20.
- Excellent “point-back” resolution of the reconstructed b candidate with respect to the primary vertex. This will help to reject vertices that have been artificially pieced together from particles from the two separate b 's in the event. The normalized B impact parameter (b_B/σ_{b_B}) with respect to the primary vertex is quite different for signal and background events, as shown in Fig. 7.19(b).

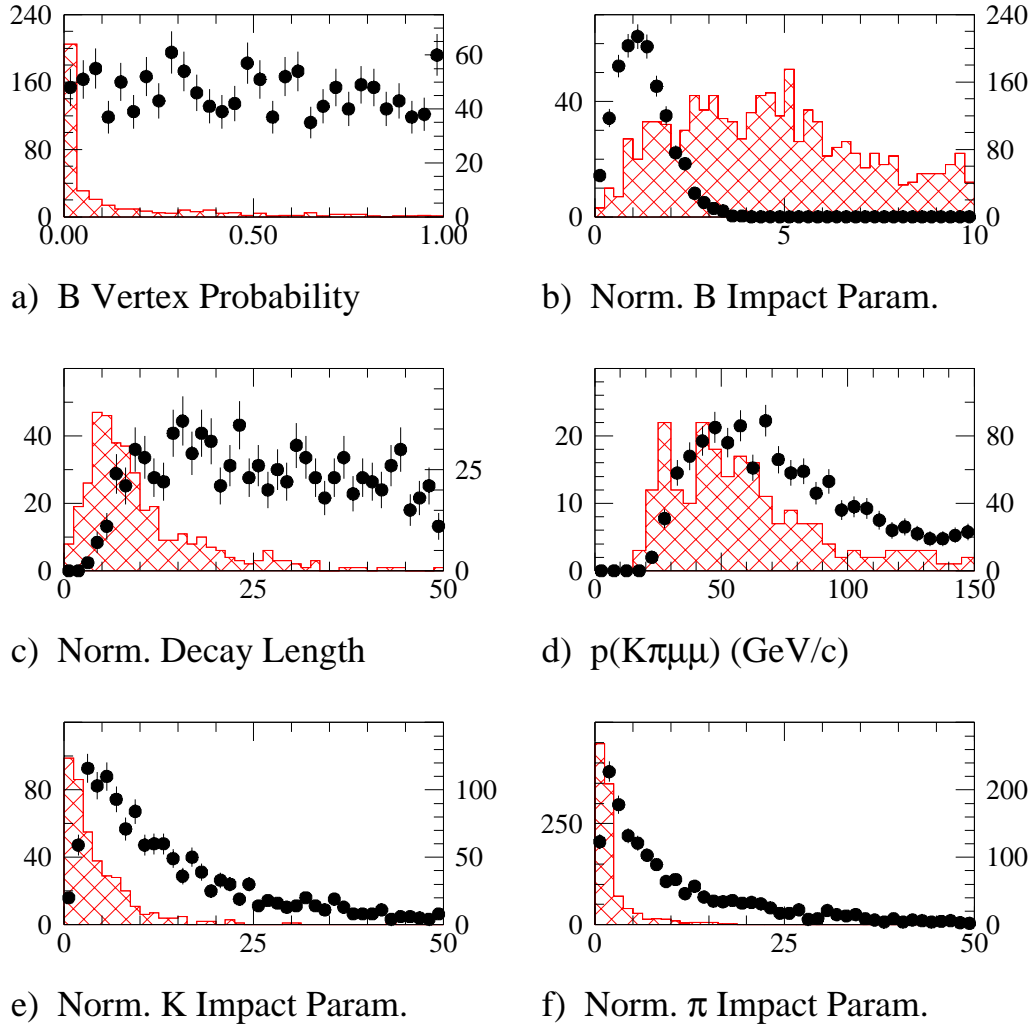


Figure 7.19: Distributions of cut variables for signal (points) and $b\bar{b}$ background (hatched) MCFAST events.

- The ability to reject combinations which include tracks that are from the primary vertex or other vertices in the event, by cutting on the impact parameter of the track with respect to that vertex. Figures 7.19(e) and (f) show the normalized impact parameter of the kaon and pion with respect to the primary vertex (b_K/σ_{b_K} and b_π/σ_{b_π}).

In addition, the signal-to-background depends on the quality of both the muon detector and the particle identification.

$B^0 \rightarrow K^{*0}\mu^+\mu^-$ events were selected using the following criteria:

- Two muons of opposite charge, each with momentum greater than 5 GeV/c. Both muon tracks were required to have at least one hit in the muon chambers.

- K track momentum greater than $3 \text{ GeV}/c$. The kaon track was also required to have at least one hit in the forward drift chamber between the RICH and calorimeter. Perfect π/K separation and 100% efficiency for reconstructing the Cherenkov photons of tracks which traverse the RICH is assumed.
- Good primary vertex with probability greater than 0.01.
- Good b vertex with probability greater than 0.01.
- Decay length greater than 7σ .
- B impact parameter with respect to the primary vertex less than 2.5σ .
- K impact parameter with respect to the primary vertex greater than 2.5σ .
- π impact parameter with respect to the primary vertex greater than 2.5σ .
- B momentum greater than $20 \text{ GeV}/c$.
- $|m(K\pi) - m_{K^*0}| < 50 \text{ MeV}/c^2$.
- Cut $100 \text{ MeV}/c^2$ about the J/ψ and ψ' nominal masses to remove regions dominated by $B \rightarrow \psi K^*$ and $B \rightarrow \psi' K^*$, which interfere with the signal.

Of 4.4 pb^{-1} of MCFAST $b\bar{b}$ background events generated (about one million events), nine pass the selection criteria. For 2 fb^{-1} of data (one year of running at a luminosity of $2 \times 10^{32} \text{ cm}^{-2} \text{ s}^{-1}$), this would correspond to 4090 events in the range $4.7 \text{ GeV}/c^2 < m(K\pi\mu\mu) < 5.7 \text{ GeV}/c^2$, shown in Fig. 7.20. The width of the B^0 mass peak obtained from the MCFAST signal Monte Carlo sample is $17 \text{ MeV}/c^2$. Thus, we can expect about 280 background events from semileptonic $b\bar{b}$ decays under the B^0 mass peak, as shown in Table 7.8. Considering that we expect about 2240 signal events, this corresponds to a signal to background ratio of about 8.

We did not include the decay $B^- \rightarrow \psi K^-$ as a background. That decay is large compared to the rare decay being considered here and will interfere with the rare decay and distort the dimuon mass distribution in the vicinity of $3 \text{ GeV}/c^2$. This, however, is a physics contribution and will certainly be observed and studied based on a mass cut on the dimuon. In fact, this state can be used to calibrate the efficiency of the analysis and can be used as a normalization for a measurement of the relative branching fraction.

A sample of 2 fb^{-1} of signal MCFAST Monte Carlo events were generated according to the Standard Model prediction for A_{fb} and Q^2 [141]. Figure 7.21 shows the distributions of A_{fb} and number of events as a function of $m(\mu^+\mu^-)$ for this sample, after all cuts have been applied. With our estimated signal to background, we should be able to easily observe and measure the position of a zero in the asymmetry if it exists, or make a strong case for non-Standard Model physics, if it does not.

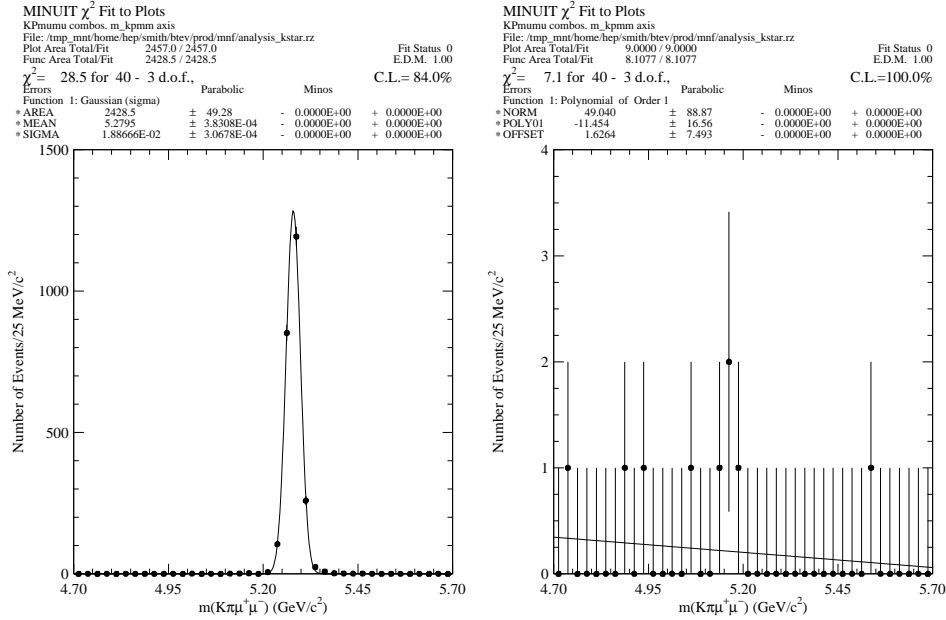


Figure 7.20: Distributions of tagged $B^0 \rightarrow K^{*0} \mu^+ \mu^-$ signal (left) and 4.4 pb^{-1} of $b\bar{b}$ background (right) MCFAST events.

Integrated Luminosity	2 fb^{-1}
$b\bar{b}$ Cross Section	$100 \mu\text{b}$
Number of $b\bar{b}$ Pairs Produced	2×10^{11}
$N_{B^0} + N_{\bar{B}^0}$ Produced	1.4×10^{11}
Est. $\mathcal{B}(B^0 \rightarrow K^{*0} \mu^+ \mu^-)$	$(1.5 \pm 0.6) \times 10^{-6}$
$\mathcal{B}(K^{*0} \rightarrow K^+ \pi^-)$	0.67
Number of Signal Events Produced	1.4×10^5
ϵ_{trig}	80%
ϵ_{cuts}	2.0%
Number of Signal Events	2240
Number of Background in Signal Box	280
Signal/Background	8

Table 7.8: Estimate of sensitivity to $B^0 \rightarrow K^{*0} \mu^+ \mu^-$ for an integrated luminosity of 2 fb^{-1} . Only backgrounds from $b\bar{b}$ semileptonic decays were included in this study.

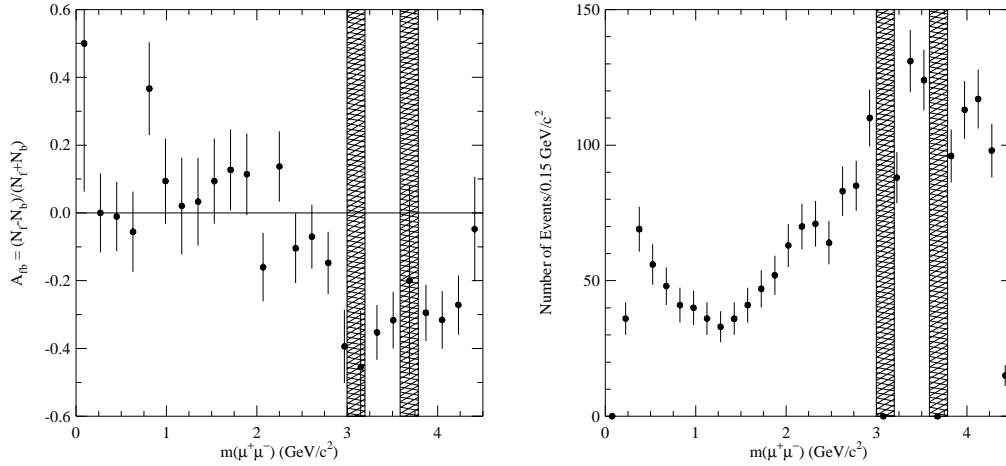


Figure 7.21: Expected forward-backward asymmetry (left) and number of events (right) as a function of $m(\mu^+\mu^-)$ for signal events after one year of running. No background is included in these plots.

7.2.3.2 The Exclusive Channel $B^+ \rightarrow K^+\mu^+\mu^-$

While the channel $B^+ \rightarrow K^+\mu^+\mu^-$ is not as rich as $B^0 \rightarrow K^{*0}\mu^+\mu^-$, in that the asymmetry A_{fb} is expected to be small within the Standard Model and beyond the Standard Model, a measurement of the decay rate is still a sensitive probe of new physics. In particular, measurement of the differential decay rate will provide input to determine the magnitude and sign of the Wilson coefficients C_7 , C_9 , C_{10} .

Most of the backgrounds to this channel are the same as those listed for the $B^0 \rightarrow K^{*0}\mu^+\mu^-$ analysis in Section 7.2.3.1. Events for this study were selected using nearly the same criteria as the $B^0 \rightarrow K^{*0}\mu^+\mu^-$ analysis:

- K track momentum greater than $4 \text{ GeV}/c$. The kaon track was also required to have at least one hit in the forward drift chamber between the RICH and calorimeter. Perfect π/K separation and 100% efficiency for reconstructing the Cherenkov photons is assumed.
- Two muons with momentum greater than $5 \text{ GeV}/c$. Both muon tracks were required to have at least one hit in the muon chambers.
- Good primary vertex with probability greater than 0.01.
- Good b vertex with probability greater than 0.01.
- Decay length greater than 7σ .
- B impact parameter with respect to the primary vertex less than 2.5σ .
- K impact parameter with respect to the primary vertex greater than 2.5σ .

- B momentum greater than 20 GeV/ c .
- Cut 100 MeV/ c^2 about the J/ψ and ψ' nominal masses to remove regions dominated by $B \rightarrow \psi K^*$ and $B \rightarrow \psi' K^*$, which interfere with the signal.

We have not simulated all sources of background. Our estimates indicate that the most serious background is from events with pairs of b 's, each of which undergoes semileptonic decay. The background contribution was estimated by applying the selection criteria to a sample of 2.5 million MCFAST semileptonic $b\bar{b}$ events, corresponding to a luminosity of 10 pb $^{-1}$. Of these events, 41 passed the selection cuts and fall within a 1 GeV/ c^2 window centered on the B^+ nominal mass. Extrapolating to an integrated luminosity of 2 fb $^{-1}$, we expect about 8200 events in this window. Assuming a uniform distribution across the B mass window (this is conservative, since it is actually falling, as shown in Fig. 7.22), one can expect about 560 events within the 2σ of the B^+ mass.

The overall efficiency for this state, with cuts designed to achieve good background rejection, is about 3.0%. Table 7.9 gives a calculation of the yield obtained for an integrated luminosity of 2 fb $^{-1}$. We include in this calculation a triggering efficiency of 80% for those events which satisfy all the analysis cuts. This is consistent with what we expect to get from the dimuon trigger (70%) 'or-ed' with the vertex trigger which recovers almost half of what the muon trigger failed to accept. The number of signal events passing the trigger and all selection criteria is approximately 1680. This gives an impressive signal-to-background ratio of 3.

The reason that BTeV can achieve excellent signal-to-background is due in a large part to a powerful particle identification system. For example, the version of the CDF detector described in the CDF II Technical Design Report [126], lacks particle identification for tracks above 1 GeV/ c . So although CDF expects a signal of 100-300 $B^+ \rightarrow K^+ \mu^+ \mu^-$ events in Run II for that version of the detector, they would be exposed to background from all pions in the event conspiring with the muons to create background. It is unlikely that CDF's signal-to-background in Run II (0.1 in Run I) will approach that expected at BTeV. In BTeV, because of the RICH, only the kaons can contribute to the background and there are fewer of them.

7.2.3.3 The Inclusive Decay $b \rightarrow s\ell^+\ell^-$

Studies are underway to determine if the BTeV detector will provide enough background rejection to make a competitive measurement of inclusive $b \rightarrow s\ell^+\ell^-$. The method under study is similar to that used by CLEO [127] [128], in which a kaon and 0-4 pions are combined with the dilepton pair. For the purposes of this study, no neutral pion candidates are allowed in the combination.

The ability to precisely reconstruct b vertices in BTeV will be instrumental in removing combinations involving non- b daughters.

Unlike the exclusive modes, an inclusive measurement would provide a *model independent* determination of the Wilson coefficients. It is important to avoid restricting this

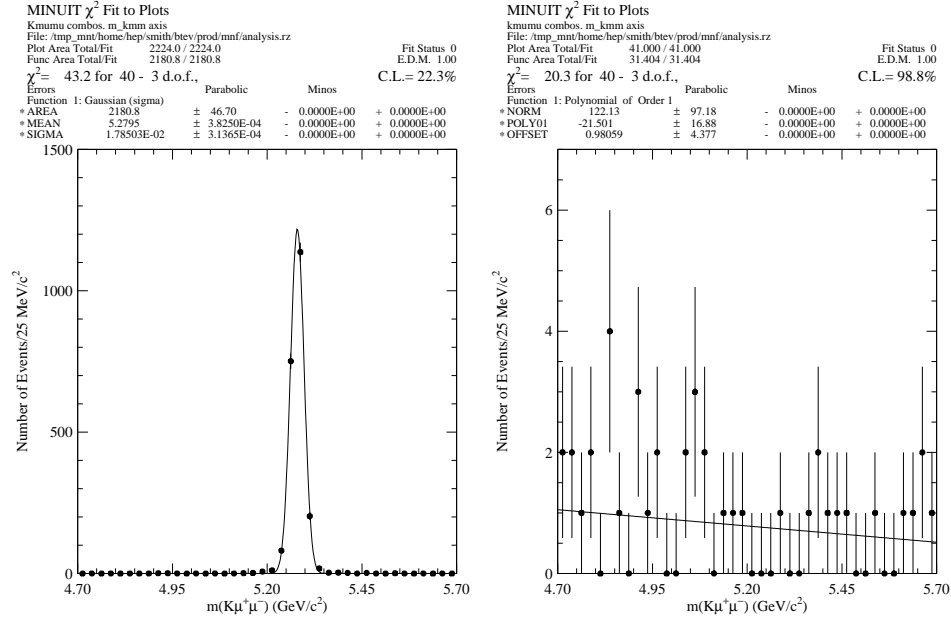


Figure 7.22: Distributions of $B^+ \rightarrow K^+ \mu^+ \mu^-$ signal (left) and 10 pb^{-1} of $b\bar{b}$ background (right) events.

measurement to only the high $m(\ell^+ \ell^-)$ region above the ψ^1 , as this introduces model dependence.

7.3 Summary of Rare Decays

Rare b decays provide detailed tests of the flavor structure of the SM at the loop level, and as such provide a complementary probe of new physics to that of direct collider searches. While radiative $b \rightarrow s\gamma$ decays are sensitive only to the magnitude of the Wilson coefficient C_7 , the semileptonic rare decays $b \rightarrow s\ell^+ \ell^-$ and the purely leptonic decays $B_{d,s} \rightarrow \ell^+ \ell^-$ are sensitive to additional operators, and so further constrain new physics.

Inclusive decays are in general cleaner theoretically than exclusive, while experimentally the difficulty is in the opposite order. Because of the difficulty of inclusive measurements, theoretical techniques to handle exclusive modes in a model-independent fashion are extremely important. There has been much recent theoretical interest in the large energy limit (LEL) of QCD, which simplifies exclusive heavy-light decays in the limit that the decay products are produced at large recoil. This has particular application to $B \rightarrow K^* \ell^+ \ell^-$ decays. In particular, the position of the zero in the forward-backward asymmetry in this decay has been shown to be model-independent. We look forward to additional advances in the theoretical understanding of the LEL.

In Run IIa, the radiative b decays $B_d \rightarrow K^{*0} \gamma$, $B_s \rightarrow K^{*0} \gamma$ and $\Lambda_b \rightarrow \Lambda \gamma$ are expected to be measured, while the purely leptonic decays $B_d \rightarrow \mu^+ \mu^-$ and $B_s \rightarrow \mu^+ \mu^-$ are not expected to be visible at the SM level. Probably the most important decay studied in this

Integrated Luminosity	2 fb^{-1}
$b\bar{b}$ Cross Section	$100 \mu\text{b}$
Number of $b\bar{b}$ Pairs Produced	2×10^{11}
Number of B^+/B^- Produced	1.4×10^{11}
Est. $\mathcal{B}(B^+ \rightarrow K^+ \mu^+ \mu^-)$	$(4.0 \pm 1.5) \times 10^{-7}$
Number of Signal Events Produced	5.6×10^4
Trigger Efficiency	80%
Selection Cut Efficiency	3.0%
Number of Background Events in Signal Box	560
Number of Signal Events	1680
Signal/Background	3

Table 7.9: Estimate of sensitivity to $B^+ \rightarrow K^+ \mu^+ \mu^-$ for an integrated luminosity of 2 fb^{-1} .

section for Run II is $B \rightarrow K^* \ell^+ \ell^-$. While this decay should be seen at 2 fb^{-1} , precision study (particularly of the zero in the forward-backward asymmetry) will require larger integrated luminosity. The inclusive measurement $b \rightarrow X_s \ell^+ \ell^-$ is most easily seen for large dimuon mass (above the $\psi(2S)$), but in this region the theory breaks down, and so the measurement is of limited interest. BTeV is currently studying the feasibility of building up an inclusive measurement for lower dimuon invariant mass from exclusive measurements involving a kaon and 0-4 pions.

7.4 Semileptonic Decays: Theory

7.4.1 Introduction

Semileptonic decays have long been used to determine elements of the CKM matrix. Examples are the determination of $|V_{ud}|$ from nuclear β -decay, $|V_{us}|$ from K_{l3} decays, and $|V_{cb}|$ from $B \rightarrow D^{(*)} \ell \bar{\nu}$ [86]. In every one of these three cases a flavor symmetry (isospin, SU(3) flavor, and HQS, respectively) greatly simplifies the theoretical understanding of the hadronic matrix element in question. In the symmetry limit, and at zero recoil, current conservation ensures that the matrix element is exactly normalized. While the deviations from the symmetry limit may be difficult to calculate, they tend to be small. Hence, the overall theoretical uncertainty on the decay process is under control. Given good experimental measurements, the associated CKM element can be reliably determined.

For semileptonic decays of b flavored hadrons to light mesons flavor symmetries are not sufficient to constrain the hadronic matrix elements. Ultimately, theoretical predictions based on lattice QCD will allow for an accurate determination of $|V_{ub}|$ from measurements of exclusive decays. Currently, the best determination of $|V_{ub}|$ comes from measurements of the inclusive decay spectrum of $b \rightarrow u \ell \bar{\nu}$ [86]. However, the kinematic cuts which are necessary to eliminate the huge charm background introduce additional theoretical difficulties, similar

to those discussed in Section 7.1.2.2. As a result, theoretical uncertainties, which are not well known, currently dominate the determination of $|V_{ub}|$ [86].

It is important that the Tevatron experiments fully explore their accessible range of exclusive semileptonic B (and B_s) decays to light hadrons. While semileptonic B decays will also be measured at the B factories, the hadronic environment has the advantage that not only B meson decays but also B_s and Λ_b decays may be studied. In particular, measurements of semileptonic B_s and Λ_b decays can provide additional information on the parameters of the heavy quark and chiral expansions. For example, a measurement of the decay $\Lambda_b \rightarrow \Lambda_c \ell \bar{\nu}$, can test HQET predictions at $\mathcal{O}(1/m_{b,c})$. Measurements of B_s decays provide tests of SU(3) symmetry violations.

Since inclusive semileptonic decays are notoriously difficult to study at hadron colliders, we focus our discussion in this section on exclusive decays. In Section 7.4.2 we first review the determination of $|V_{cb}|$ from $B \rightarrow D^{(*)} \ell \bar{\nu}$ decays, and then discuss the decay $\Lambda_b \rightarrow \Lambda_c \ell \bar{\nu}$. Section 7.4.3 contains our discussion of semileptonic B decays to light hadrons.

7.4.2 Decays to Charm Flavored Final States

7.4.2.1 $B \rightarrow D^{(*)} \ell \bar{\nu}$

As discussed in Chapter 1, heavy quark symmetry allows all the form factors, which appear in semileptonic $B \rightarrow D^{(*)}$ decay, to be related, at leading order in $1/m_{b,c}$, to a single universal function, the Isgur-Wise function $\xi(w)$. Corrections to these relations have been calculated to $\mathcal{O}(1/m_{b,c}^2)$ and $\mathcal{O}(\alpha_s^2)$. See, for example, Ref. [142].

We can write the differential decay rate as

$$\begin{aligned} \frac{d\Gamma(B \rightarrow D^{*} \ell \bar{\nu})}{dw} &= \frac{G_F^2 |V_{cb}|^2}{48\pi^3} (m_B - m_{D^*})^2 m_{D^*}^3 \sqrt{w^2 - 1} (w + 1)^2 \\ &\times \left(1 + \frac{4w}{w + 1} \frac{m_B^2 - 2wm_B m_{D^*} + m_{D^*}^2}{(m_B - m_{D^*})^2} \right) \mathcal{F}(w)^2 \end{aligned} \quad (7.94)$$

where the corrections to the symmetry limit are included in the form factor $\mathcal{F}(w)$. At zero recoil $\mathcal{F}(1)$ coincides with the Isgur-Wise function up to perturbative and $\mathcal{O}(1/m_{b,c}^2)$ corrections, which can be parametrized as follows [144]:

$$\mathcal{F}(1) = \eta_A \left(1 + \delta_{1/m^2} \right) . \quad (7.95)$$

η_A contains the perturbative QCD (and QED) corrections which have been calculated to $\mathcal{O}(\alpha_s^2)$ [143]. δ_{1/m^2} contains the power corrections, which start at $\mathcal{O}(1/m_{b,c}^2)$ for this case. The power corrections must be calculated from nonperturbative methods. They have been estimated from a number of different approaches, which include non-relativistic quark models and QCD sum rules. Once the perturbative and nonperturbative corrections are included, Ref. [144] gives the value

$$\mathcal{F}(1) = 0.91 \pm 0.04 , \quad (7.96)$$

where the error is dominated by the uncertainty in the nonperturbative corrections. The uncertainty in Eq. (7.96) leads to a theoretical error on V_{cb} which is similar in size to the current experimental error. Hence, a significant reduction of the uncertainty on V_{cb} will require a more accurate theoretical calculation of $\mathcal{F}(1)$.

The $B \rightarrow D^{(*)}\ell\bar{\nu}$ transition has also been studied in lattice QCD calculations. The first calculations concentrated on the slope of the Isgur Wise function [145]. At that point, the errors on the form factors were too large to be competitive with the results shown above. Since the experimental results have to be extrapolated to zero recoil, theoretical predictions of the slope can help reduce the error associated with the extrapolation.

Ref. [146] introduces a new method based on ratios of matrix elements, which exploits heavy quark flavor symmetry to calculate the form factors at zero recoil with high precision. The ratios from which the form factors are obtained become exactly equal to unity in the flavor symmetry limit, where all errors cancel. Away from the symmetry limit, the errors are proportional to $\mathcal{F}(1) - 1$ (instead of $\mathcal{F}(1)$). As a result, as shown in Ref. [146], the statistical and systematic errors on $\mathcal{F}(1)$ are small, 2 – 3%. The results are obtained in the quenched approximation. Given a sufficient computational effort, the prospects for improved theoretical predictions of $\mathcal{F}(1)$ are excellent.

The form factors in semileptonic B_s decay are related to those in B decay via SU(3). The leading SU(3)-breaking chiral corrections to the Isgur-Wise function were calculated in Ref. [85].

7.4.2.2 $\Lambda_b \rightarrow \Lambda_c \ell \bar{\nu}$

Semileptonic $\Lambda_b \rightarrow \Lambda_c$ decays, which cannot be studied at the $\Upsilon(4S)$, not only provide an alternate means to obtain $|V_{cb}|$, but more importantly provide a test of the heavy quark expansion at subleading order.

The most general expressions for the matrix element of the vector and axial vector currents between Λ_b and Λ_c states are

$$\begin{aligned} \langle \Lambda_c(v', s') | \bar{c} \gamma^\mu b | \Lambda_b(v, s) \rangle &= \bar{u}(v', s') [g_1 \gamma^\mu + g_2 v^\mu + g_3 v'^\mu] u(v, s) \\ \langle \Lambda_c(v', s') | \bar{c} \gamma^\mu \gamma_5 b | \Lambda_b(v, s) \rangle &= \bar{u}(v', s') [g_1 \gamma^\mu + g_2 v^\mu + g_3 v'^\mu] u(v, s) \end{aligned} \quad (7.97)$$

where the states have been labelled with their four-velocities instead of their momenta, and the form factors F_i and G_i are functions of $w \equiv v \cdot v'$. At leading order in $1/m_c$ and α_s all six form factors are related to a universal form factor,

$$\begin{aligned} f_1(w) = g_1(w) = -f_2(w) = -g_2(w) &= \xi_\Lambda(w) \\ f_3(w) = g_3(w) &= 0 \end{aligned} \quad (7.98)$$

where $\xi_\Lambda(1) = 1 + O(\alpha_s(m_c))$.

Because the light degrees of freedom in a Λ_Q baryon are in a spin 0 state, the subleading corrections to the heavy quark limit take a simpler form than for mesons [148]. In contrast

with $B \rightarrow D^{(*)}$ decay, in which three new form functions and one constant (in addition to the Isgur-Wise function) are required to specify the form factors at $O(1/m_{b,c})$, the form factors for $\Lambda_b \rightarrow \Lambda_c$ transitions are determined at $O(1/m_{b,c})$ in terms of the Isgur-Wise function and one additional parameter,

$$\bar{\Lambda}_\Lambda = m_{\Lambda_b} - m_b + O(1/m_b^2) = m_{\Lambda_c} - m_c + O(1/m_c^2) \simeq 700 \text{ MeV}. \quad (7.99)$$

Since m_b may be determined in a number of ways (such as Upsilon sum rules [150], moments of spectra in inclusive B decays [151] and lattice calculations of the $\bar{b}b$ spectrum [152]), precision measurements of the $\Lambda_b \rightarrow \Lambda_c \ell \bar{\nu}$ form factors provide a stringent test of HQET at subleading order.

Including corrections up to $O(1/m_{b,c})$ in the heavy quark expansion, the form factors (7.97) satisfy the relations [148]

$$\begin{aligned} f_1(w) &= \left[1 + \left(\frac{\bar{\Lambda}_\Lambda}{2m_c} + \frac{\bar{\Lambda}_\Lambda}{2m_b} \right) \right] \xi_\Lambda(w), \\ f_2(w) = g_2(w) &= -\frac{\bar{\Lambda}_\Lambda}{m_c} \left(\frac{1}{1+w} \right) \xi_\Lambda(w), \\ f_3(w) = -g_3(w) &= -\frac{\bar{\Lambda}_\Lambda}{m_b} \left(\frac{1}{1+w} \right) \xi_\Lambda(w), \\ g_1(w) &= \left[1 - \left(\frac{\bar{\Lambda}_\Lambda}{2m_c} + \frac{\bar{\Lambda}_\Lambda}{2m_b} \right) \left(\frac{1-w}{1+w} \right) \right] \xi_\Lambda(w). \end{aligned} \quad (7.100)$$

Thus, measuring the form factors in $\Lambda_b \rightarrow \Lambda_c$ decay provides a stringent test of the subleading corrections to HQET. Complete differential distributions for these decays are given in Ref. [149], including the effects of Λ_b polarization.

An important background to $\Lambda_b \rightarrow \Lambda_c$ semileptonic decay comes from Λ_b decays to excited charmed hadrons, which then decay via emission of a soft photon or pion to a Λ_c . At leading order in the heavy quark expansion this branching fraction would be predicted to be small, since the light degrees of freedom in an excited baryon are orthogonal to those in a Λ_b in the heavy quark limit, but, as discussed in Ref. [153], there are large $O(\Lambda_{\text{QCD}}/m_c)$ corrections to this statement (note that because $\bar{\Lambda}$ for baryons is roughly twice that in mesons, $1/m_c$ effects are expected to be correspondingly larger in baryons). These authors considered the HQET expansion for semileptonic Λ_b decays to the spin 1/2 $\Lambda_c(2593)$ and its spin symmetry partner the spin 3/2 $\Lambda_c(2625)$. Using large N_c arguments to determine the corresponding matrix elements, they estimated the branching fraction to these two states to be

$$\frac{\Gamma(\Lambda_b \rightarrow (\Lambda_c^*(2593) + \Lambda_c^*(2625))\ell\bar{\nu}_\ell)}{\Gamma(\Lambda_b \rightarrow X\ell\bar{\nu}_\ell)} \sim 25 - 33\%. \quad (7.101)$$

Decays from excited baryons are therefore expected to provide a significant background to semileptonic $\Lambda_b \rightarrow \Lambda_c$ decay.

To date, most of the lattice QCD calculations of beauty systems have concentrated on the meson sector. Lattice QCD calculations of $\Lambda_b \rightarrow \Lambda_c l \nu$ do not yet exist. However, it should be straightforward to extend the lattice analysis of $B \rightarrow D^{(*)} l \nu$ decays described in the previous section to the baryon decay $\Lambda_b \rightarrow \Lambda_c l \nu$.

7.4.3 $B \rightarrow \pi(\rho)\ell\bar{\nu}$

The best determination of $|V_{ub}|$ comes at present from the measurements of the inclusive decay spectrum of $b \rightarrow u\ell\bar{\nu}$ [86]. However, in order to reduce the huge charm background, one has to impose kinematic cuts on the charged lepton energy, for example. Because such cuts restrict the available final state phase space, they can introduce large nonperturbative corrections in the OPE, or cause the OPE to break down entirely. Kinematic cuts in different variables, such as the hadronic invariant mass [154] or the q^2 spectrum [155], have been proposed in order to reduce the theoretical uncertainties, which currently dominate the errors on $|V_{ub}|$. This work together with improved experimental measurements of the inclusive $b \rightarrow u\ell\bar{\nu}$ decay at the B factories will lead to a better determination of $|V_{ub}|$.

Here, we explore the potential of accurate determinations of $|V_{ub}|$ via exclusive decays. In contrast to the cases discussed in the previous section, in the case of exclusive heavy hadron decays to light hadrons flavor symmetries alone do not provide sufficient constraints on the hadronic matrix elements (and form factors). Heavy quark spin and flavor symmetries and SU(3) symmetry yield relations among the form factors for $B \rightarrow \pi(\rho)\ell\bar{\nu}$, $D \rightarrow \pi(\rho)\ell\bar{\nu}$, $D \rightarrow K^{(*)}\ell\bar{\nu}$, $B \rightarrow K^{(*)}\ell^+\ell^-$, $B \rightarrow K^{(*)}\gamma$, and related B_s and D_s decays. The expected corrections to these relations vary from a few to 20 %. This is discussed in more detail in Section 7.1.3.3. If we want to get absolute predictions for the form factors, we must rely on nonperturbative methods such as lattice QCD.

A number of improved lattice QCD calculations of the exclusive semileptonic decay $B \rightarrow \pi\ell\bar{\nu}$ have recently become available [27]. At present, the uncertainties in the lattice QCD calculations are still large; the errors on the form factors are roughly 15 – 20% (see Section 7.1.3.2). Reducing these theoretical errors will require a significant effort and the commitment of sufficient computational resources to such calculations. Ultimately, lattice QCD calculations will provide accurate predictions of the hadronic form factors in the high recoil momentum region. In order to use these predictions for determinations of $|V_{ub}|$, we need experimental measurements of partial differential decay rates, with matching precision.

7.5 Semileptonic Decays: Experiment

7.5.1 Semileptonic Decays at CDF

7.5.1.1 Introduction

In this report, we describe CDF's prospects for study of semileptonic decays. Specifically, we focus on the decay of the Λ_b baryon which is not produced at the $e^+e^- B$ factories. The primary interest is total and differential decay rates. These measurements are limited by statistical uncertainties. Therefore, our studies have largely focussed on trigger strategies to optimize event yields versus trigger bandwidth. We have considered the possibility of measuring the differential decay rate $(1/\Gamma)d\Gamma/dQ^2$. Semileptonic B decay events are also useful as a control sample for study of tagging methods or as a backup sample for measuring B_s - \bar{B}_s flavor oscillations. However, except for a discussion of possible trigger selections, we

leave discussion of these topics to other sections of the Workshop report.

The strategy for extracting semileptonic decay events is to take advantage of the high purity of lepton triggers as well as the significant impact parameters of B decay daughters. CDF's three-level trigger system in Run II will provide the tools necessary to maintain the trigger rate at a manageable level while maintaining a high efficiency for B -decay events. Specifically, the eXtremely Fast Tracker (XFT) will offer a significant improvement for the Run II trigger over the Run I trigger by providing tracking information in Level 1. This capability enables a track to be matched to an electromagnetic calorimeter cluster for improved electron identification or to be matched to a track segment in the muon system for better muon identification as well as a track-only trigger. In Level 2 the Silicon Vertex Tracker (SVT) will add SVX information to the XFT tracks and provide impact parameter information and thus provide the possibility of a displaced-track trigger.

7.5.1.2 Physics Goals

The semileptonic decay of heavy baryons can be described by five form factors. However, in Heavy Quark Effective Theory (HQET) these reduce to a single universal form factor in next-to-leading order. This is to be contrasted to meson decays in which the form factors reduce to a single form factor only at leading order. Measuring the differential decay rate as a function of the momentum transfer Q^2 in Λ_b decays can provide stringent tests of HQET. Because Q^2 is the mass of the lepton-neutrino pair, we must know the neutrino momentum. With the possibility of using 3D vertex reconstruction in Run 2, we can find the Λ_b direction and derive the neutrino momentum up to a quadratic ambiguity. This is described in more detail in Section 7.5.1.6 where we describe the potential for measuring the differential decay rate $(1/\Gamma)d\Gamma/dQ^2$ in $\Lambda_b \rightarrow \Lambda_c \ell \nu$ decays. In the Run I Λ_b lifetime analysis, 197 ± 25 semileptonic $\Lambda_b \rightarrow \Lambda_c \ell \nu$, $\Lambda_c \rightarrow p K \pi$, were partially reconstructed [156]. We use the cuts and yield from that analysis to provide a basis for Run II yields.

Semileptonic decays may also provide a good sample for measuring B_s mixing for lower values of x_s . Using semileptonic decays provides a fall-back position if the yield is high and the all-hadronic trigger can not collect enough data. Two possibilities exist for studying B_s mixing through semileptonic decay channels. The lepton may be used to tag the event and then one must fully reconstruct the away-side B_s , or Same-Side-Tagging, Jet-Charge or Soft-Lepton tagging may be used to measure x_s from the "first wiggle" in $B_s \rightarrow D_s \ell \nu X$ decays. 360 events were reconstructed in Run I in the 8 GeV inclusive lepton trigger data through the decay $B_s \rightarrow D_s \ell \nu X$ where $D_s \rightarrow \phi \pi$ or KK^{*0} . Details of the expected time resolution and x_s reach are discussed in the report of Working Group 3. Because the neutrino momentum is unknown, mixing measurement using semileptonic decays suffer from poor resolution of the decay time. The all-hadronic decay $B_s \rightarrow D_s \pi$, where $D_s \rightarrow \phi \pi$ or KK^{*0} and the B_s is fully reconstructed, offers the prospect for the greatest reach in Δm_s . Therefore, we have studied the prospect of a trigger on a tagging lepton and an opposite-side displaced track which could come from a hadronic B_s decay.

7.5.1.3 Simulations

To study the efficiency of the possible trigger selections for the signals of interest, we use a simple parametric Monte Carlo simulation to compare the Run II geometric and kinematic acceptance to that of published Run I physics analyses. We use the measured yields for normalization. In our Monte Carlo studies, we generate single b quarks according to next-to-leading-order QCD. The B hadrons that result after Peterson ($\epsilon = 0.006$) [157] fragmentation smearing are forced to decay to modes of interest using the CLEO Monte Carlo QQ [158]. To model detector performance, we apply Gaussian smearing to the generated quantities in these Monte Carlo events.

We assume that the offline track-reconstruction and analysis-cut efficiencies will be the same as in Run I. Since we determine our yields relative to Run I, we do not correct for these effects. The part of the detector and the trigger that is substantially different from Run I is the silicon detector (SVXII). We model the SVXII as 5 concentric cylinders at the mean radii of the 5 layers. We account for the gaps between silicon sensors and assume that there is an additional 2% hit inefficiency per layer.

In this study we want to compare the acceptance for decays in the reconstruction fiducial. Therefore, we require all charged particles in a final state to have transverse momentum P_T exceeding $0.5 \text{ GeV}/c$ and to leave the COT drift chamber at its outside radius. Furthermore, after accounting for geometry and expected hit efficiency, we require all tracks to have hits in 4 of 5 SVX layers, and if a track is to be considered fiducial for the SVT, it must be of $P_T > 2 \text{ GeV}/c$ and have hits in the 4 inner layers. We also require electrons and muons to project to the fiducial regions of the central calorimeter and muon detectors, respectively. We also model the trigger efficiencies with parameterizations.

Since the output of the trigger is dominated by backgrounds, it is not possible to determine trigger rates from pure Monte Carlo samples. Instead, we simulate the performance of the Run II trigger system using data taking Run I using trigger thresholds significantly lower than were used in normal operation and below the cuts we intend to apply in Run II. We model the performance of the Run II trigger electronics using a version of the Run II simulations modified for the Run I detector configurations. The instantaneous luminosities of the test runs correspond to 0.4 to $1.4 \times 10^{32} \text{ cm}^{-2} \text{ s}^{-1}$ with 36-bunch operation, allowing us to model the change in trigger performance as a function of instantaneous luminosity. We correct the results for the increased muon and silicon detector acceptances.

7.5.1.4 Selection Criteria

There are various event properties that can be examined in the Level 1 and Level 2 trigger systems. Because the Level 1 bandwidth is large and there is substantial overlap with other proposed trigger selections, we propose using only a single-lepton selection in Level 1 which limits systematic effects. For Level 2, we want to take advantage of the decay properties of b hadrons, especially the long lifetime. The SVT allows us to select displaced tracks. We can also take advantage of b production and decay kinematics to select tracks associated with the lepton in the Level 2 trigger. Our proposed trigger signature is a lepton with a

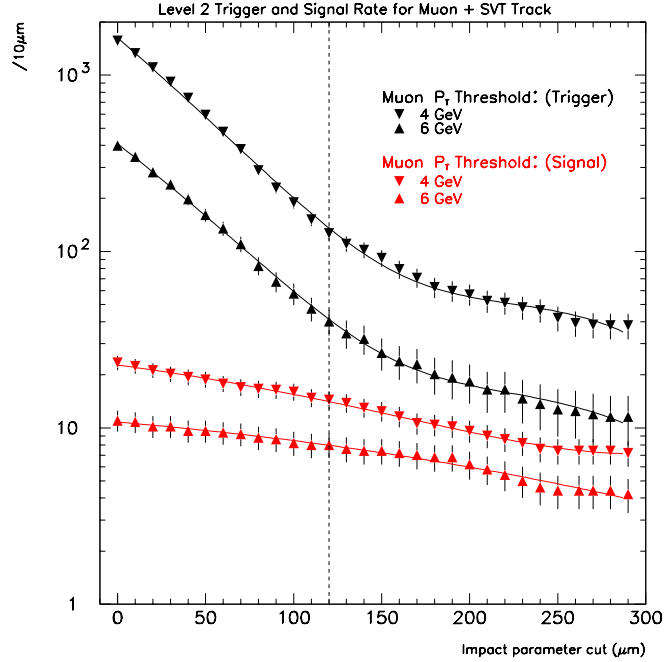


Figure 7.23: Dependence of the trigger rate on the impact parameter cut on tracks found by the SVT for the muon-trigger test data (top two curves) and the $b\bar{b} \rightarrow \Lambda_b X \rightarrow \Lambda_c \mu\nu$ Monte Carlo (bottom two curves). The vertical scale is arbitrary. The dashed line shows an impact parameter cut of $120 \mu\text{m}$.

displaced track. Additional handles include the angle between the lepton and the displaced track found by SVT $\Delta\phi(\ell, SVT)$ and the transverse mass M_T of the lepton track pair. ($M_T^2 \simeq p_{T,1} p_{T,2} (1 - \cos \Delta\phi)/c^2$) For tracks coming from the decay of a single B , we expect the angle to be small and the two-particle mass to be less than the B mass.

Figure 7.23 shows the dependence of Level 2 trigger rate on the impact parameter cut applied to tracks found by SVT in events with trigger muons for the test-run data and for the Monte Carlo simulations of the benchmark channel the $b\bar{b} \rightarrow \Lambda_b X \rightarrow \Lambda_c \mu\nu, \Lambda_c \rightarrow pK\pi$ mode. The trigger rate falls sharply with impact parameter up to about $120 \mu\text{m}$. Above $150 \mu\text{m}$, the decrease in trigger rate is approximately equal to that for the signal, indicating a background of real semileptonic B -decay events. Therefore cutting on impact parameter beyond $150 \mu\text{m}$ will not increase purity. For consistency with other CDF selections, we expect to cut at $120 \mu\text{m}$. Figure 7.24 shows the distributions of $\Delta\phi$ versus transverse mass for events in test run data in which a track has been found by the SVT simulation with $|d_0| > 120 \mu\text{m}$. Requiring $\Delta\phi < 90^\circ$ and $M_T < 5 \text{ GeV}/c^2$ gives substantial background reduction without loss of the semileptonic-decay signal. For the proposed trigger selection with a $4 \text{ GeV}/c$ cut on lepton momentum, we expect a trigger cross section of $53 \pm 8 \text{ nb}$ for muons and $90 \pm 36 \text{ nb}$ for electrons. At a luminosity of $10^{32} \text{ cm}^{-2} \text{ s}^{-1}$ (*i.e.* $100 \mu\text{b}^{-1} \text{ s}^{-1}$) this corresponds to a rate of $14 \pm 4 \text{ Hz}$ out of a total Level 2 trigger budget of 300 Hz . Note that this trigger rate is about a factor of 3 lower than would be achieved with an inclusive 8 GeV lepton sample as was used in Run I.

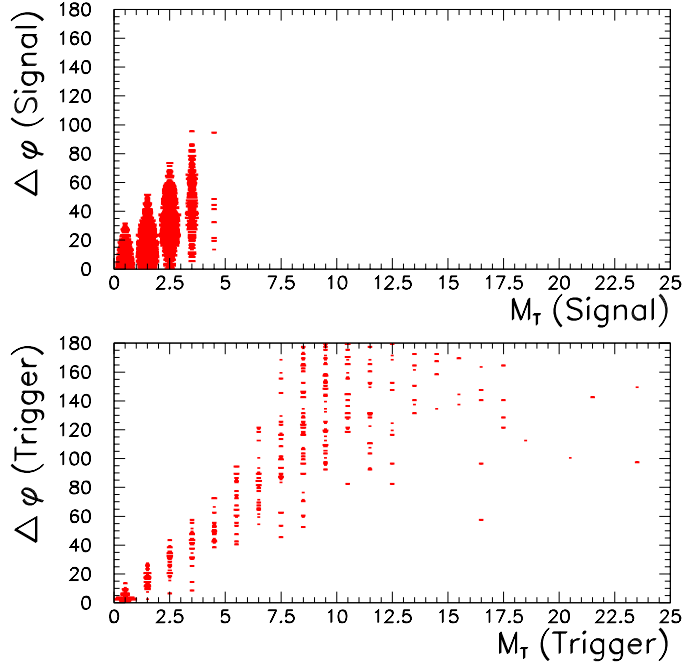


Figure 7.24: The distributions of $\Delta\phi(\mu, SVT)$, and $M_T(\mu, SVT)$ for the test-run data (bottom plot) and the $b\bar{b} \rightarrow \Lambda_b \rightarrow \Lambda_c \mu \nu$ signal (top plot) after impact parameter cut.

We have also considered the effectiveness of a trigger using a lepton and a displaced track in order to extract a sample of B decays that can be fully reconstructed and have an away-side lepton tag. Our benchmark process for this type of event is $B_s \rightarrow D_s \pi, D_s \rightarrow \phi \pi$ or KK^{*0} . As with the lepton and displaced track from the decay of a single B , the effectiveness of a cut on the impact parameter does not improve beyond $|d_0| \simeq 150 \mu\text{m}$ and is independent of the muon P_T . The $\Delta\phi(\mu, SVT)$ and M_T distributions for simulation of the benchmark process are compared to the trigger background from the simulation on the test data in Figure 7.25 after requiring $|d_0| > 120 \mu\text{m}$. The requirements $\Delta\phi(\mu, SVT) > 90^\circ$ and $M_T > 5 \text{ GeV}/c^2$ reduce backgrounds with only a small reduction in the signal. For the proposed trigger selection with a $4 \text{ GeV}/c$ cut on lepton momentum, we expect a trigger cross section of $48 \pm 8 \text{ nb}$ for muons and $120 \pm 40 \text{ nb}$ for electrons. At a luminosity of $10^{32} \text{ cm}^{-2} \text{ s}^{-1}$ this corresponds to a rate of $16 \pm 4 \text{ Hz}$.

7.5.1.5 Signal Rate Expectations

To complete the study, we evaluate the various trigger criteria in terms of the expected Run II event yield. Monte Carlo samples are generated for the semileptonic decays of interest and passed through the trigger scenarios. The number of Run II events expected is based on the ratio of the acceptance for the proposed Run II semileptonic triggers and the Run I semileptonic trigger scaled by acceptance and efficiency ratios.

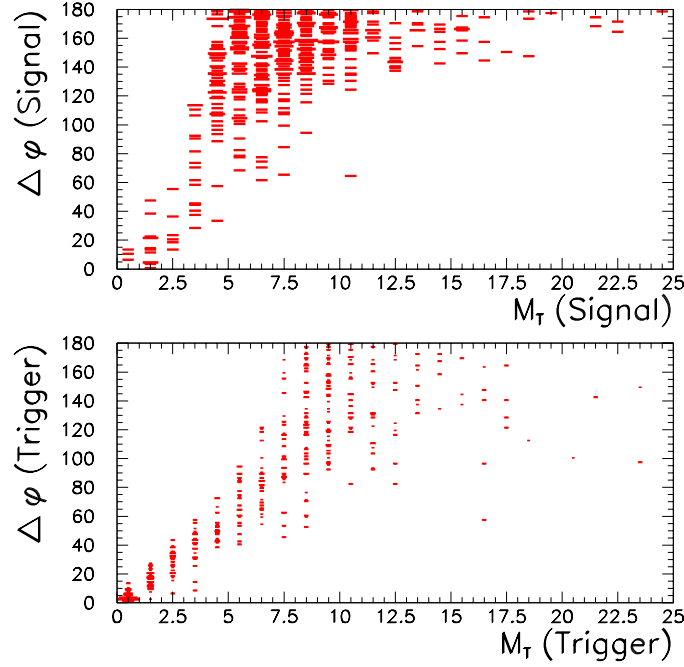


Figure 7.25: Distributions of $\Delta\phi(\mu, SVT)$, and $M_T(\mu, SVT)$ for the test-run data (bottom plot) and the $b\bar{b} \rightarrow B_s X \rightarrow D_s \pi$ signal (top plot).

The Run I acceptance A_I is the acceptance for the Run I 8 GeV inclusive lepton trigger. The Run II acceptance A_{II} corresponds to the Run II trigger of interest. To account for the Run I trigger efficiency, the Monte Carlo events were required to pass a trigger model based on the Run I Level-2 inclusive lepton trigger efficiency [159] [160]. There are additional factors which affect the number of events expected in Run II. The SVX acceptance will be greater in Run II: $A_{(SVXII)} = 1.4 \times A_{(SVXI)}$. In addition, we assume the total acceptance gained by the central muon-system upgrade to be a factor of 1.4. The increase in the instantaneous luminosity in Run II also increases the number of expected events, we assume the ratio between Run I and Run II to be:

$$\mathcal{L}_{II}/\mathcal{L}_I = 2 \text{ fb}^{-1}/100 \text{ pb}^{-1} = 20. \quad (7.102)$$

To normalize our sample with the Run I events sample, the same offline selection cuts are applied. For $\Lambda_b \rightarrow \Lambda_c \ell \nu$ decay the cuts are:

- $P_T(K, \pi, p) \geq (0.7, 0.6, 1.5) \text{ GeV}/c$;
- $3.5 \leq M(\ell\Lambda_c) \leq 5.6 \text{ GeV}/c^2$;
- $P_T(\Lambda_c) \geq 5.0 \text{ GeV}/c$.

We also require the kaon, pion and proton to be within a cone of 0.8 in η - ϕ space. The decay channel $B_s \rightarrow D_s \pi$ has not been reconstructed so we only estimate the efficiency of

the lepton + track trigger selection relative to the all-hadronic trigger [161]. This estimate does not include the reduction in yield from “analysis” cuts.

The number of events expected in Run II N_{II} with respect to the number of events reconstructed in Run I N_I for each decay channel is calculated using the following relation:

$$\frac{N_{II}}{N_I} = \frac{A_{II}}{A_I} \cdot \frac{\mathcal{L}_{II}}{\mathcal{L}_I} \cdot A_{(SVXII)}. \quad (7.103)$$

The expected yield for $\Lambda_b \rightarrow \Lambda_c \ell \nu$ decays with the same-side 4 GeV/ c lepton plus displaced-track selection described above is 25000 in 2 fb^{-1} of Run II. For $B_s \rightarrow D_s \ell \nu$ decays, we expect 33000 events.

The yield of $B_s \rightarrow D_s \pi$ decay events from the opposite-side 4 GeV lepton trigger selection described above is 106 events in 2 fb^{-1} without correction for reconstruction and analysis cut efficiencies. This number can be directly compared to the yield of 10600 expected under the same assumptions from required two displaced tracks with $P_T > 2 \text{ GeV}/c$ as described in Proposal P-909 [161]. Although tagging dilutions and efficiencies are outside the scope of this section, it is clear that including the tagging lepton as the primary trigger element is an inferior procedure to a trigger on particles of the signal decay.

7.5.1.6 Q^2 Spectrum

As discussed in Section 2, semileptonic decays of B baryons present the possibility of measuring the momentum transfer Q^2 in Λ_b decays. To study the feasibility of such a measurement, we generate $\Lambda_b \rightarrow \Lambda_c \ell \nu$ decays. For $\Lambda_b \rightarrow \Lambda_c \ell X$, where X is not observed, we can describe the kinematics using the following energy and momentum conservation rules:

$$\begin{aligned} E_{\Lambda_b} &= E_{\Lambda_c} + E_X; \\ p_X &= |p_X|^2 = |p_{\Lambda_b} - p_{\Lambda_c}|^2 = p_{\Lambda_b}^2 + p_{\Lambda_c}^2 - 2p_{\Lambda_b} p_{\Lambda_c} \cos \theta. \end{aligned} \quad (7.104)$$

This method is described in more detail in [162]. In our toy Monte Carlo sample, we use P_{Λ_b} , P_{Λ_c} , and P_ℓ and 3D-vertex and kinematic constraints to reconstruct P_ν . The Q^2 distributions from the Monte Carlo event generator, after kinematic cuts, and after detector smearing as well as the reconstructed Q^2 distribution are shown in Figure 7.26. The resolution of the Q^2 reconstruction is shown in Figure 7.27 (top plot). The ratio of the generated Q^2 distribution to the physical solution gives the reconstruction efficiency and is shown in Figure 7.27.

As a check of our the ability to measure the Q^2 distribution in Run II, we perform a simple Monte Carlo experiment. We generate two independent samples of $\Lambda_b \rightarrow \Lambda_c \ell \nu$. One sample is used to make a generator level Q^2 distribution. The other sample is normalized to the expected Run II yield. Kinematic and resolution smearing were applied to the normalized sample. The Q^2 distribution is calculated after correcting for the reconstruction efficiency. The generated and reconstructed distribution is shown in Figure 7.28. This shows that given the number of expected events in Run II we can reasonably expect to reconstruct the Q^2 distribution. However, there are higher-order Λ_b decays which complicate the reconstruction.

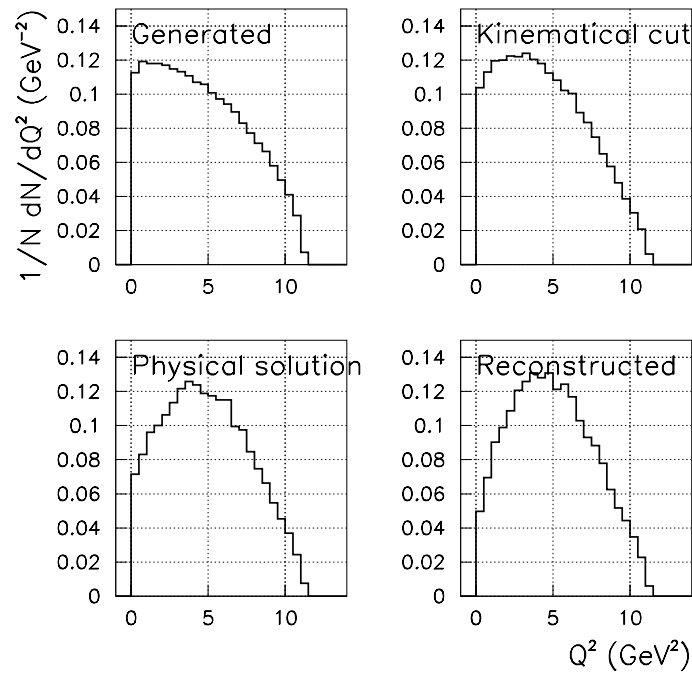


Figure 7.26: Monte Carlo simulation of the Q^2 distribution. The generated distribution is shown in the top left. The distribution after the kinematic cuts is in the top right. The distribution after the detector resolution has been applied is shown in the lower right. The distribution using the kinematic constraints and 3D-vertexing is shown in the lower right.

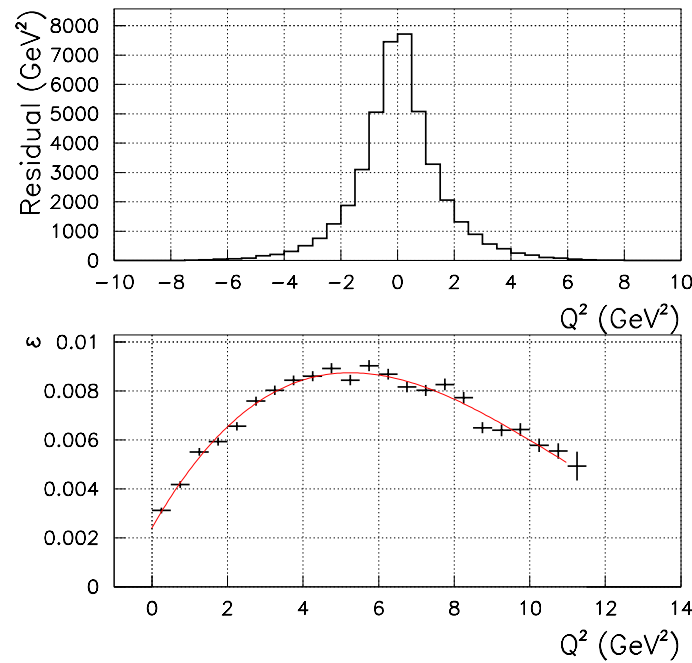


Figure 7.27: The resolution of the reconstructed Q^2 distribution is shown in the top plot. The reconstruction efficiency is shown in the bottom plot.

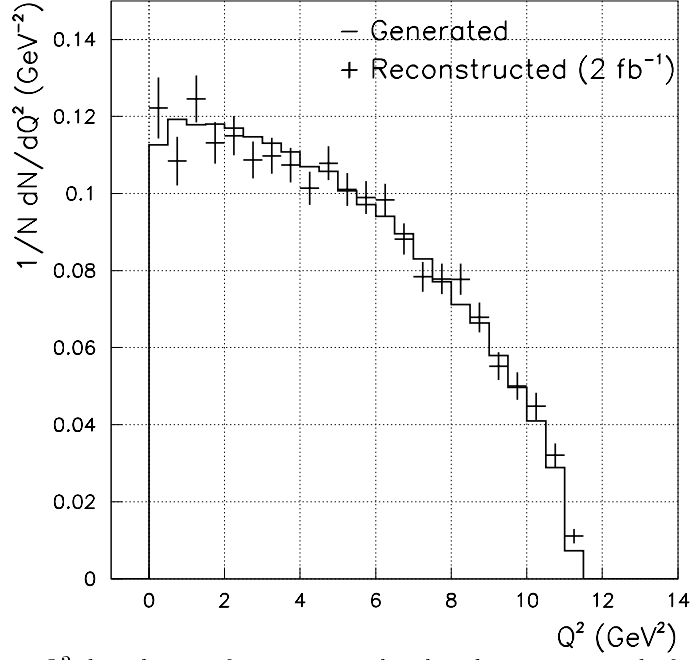


Figure 7.28: Q^2 distribution for generator level and reconstructed after correcting for efficiency.

Higher-order Contamination

The branching ratio for semileptonic Λ_b decays to higher-order baryons may not be negligible and can contaminate the decay channel of interest. We investigate the kinematic properties of these higher-order decays to determine a method to reject these events efficiently. Presumably the dominant source of contamination is decays with a Λ_c and two pions. The possible states are:

$$\begin{aligned} \Lambda_b &\rightarrow [\Sigma_c \pi^+]_{I=0} \ell \bar{\nu}_\ell \\ &\quad \swarrow \Lambda_c^+ \pi^- \\ &\quad \searrow p K^- \pi^+ \end{aligned} \quad (7.105)$$

$$\begin{aligned} \Lambda_b &\rightarrow [\Sigma_c^{++} \pi^-]_{I=0} \ell \bar{\nu}_\ell \\ &\quad \swarrow \Lambda_c^+ \pi^+ \\ &\quad \searrow p K^- \pi^+ \end{aligned} \quad (7.106)$$

$$\begin{aligned} \Lambda_b &\rightarrow \Lambda_c^+ \pi^+ \pi^- \ell \bar{\nu}_\ell \\ &\quad \swarrow p K^- \pi^+ \end{aligned} \quad (7.107)$$

$$\begin{aligned} \Lambda_b &\rightarrow [\Sigma_c^+ \pi^0]_{I=0} \ell \bar{\nu}_\ell \\ &\quad \swarrow \Lambda_c^+ \pi^0 \\ &\quad \searrow p K^- \pi^+ \end{aligned} \quad (7.108)$$

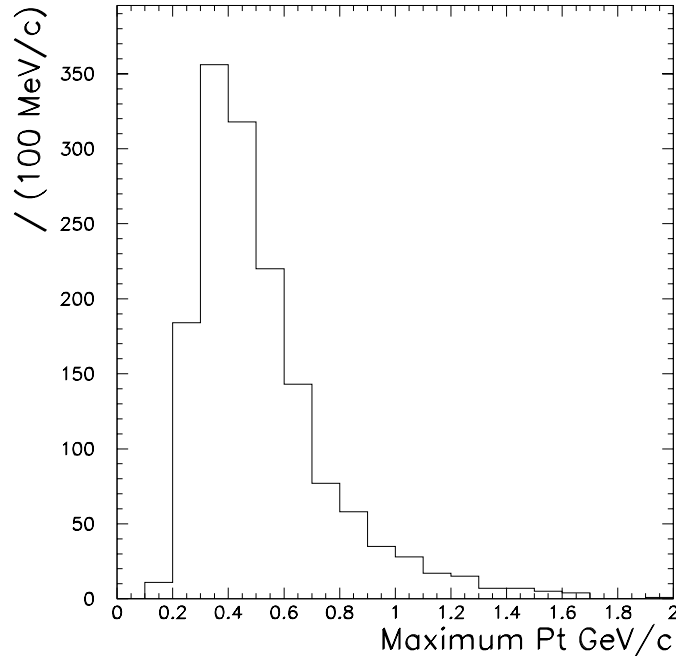


Figure 7.29: Distribution of the maximum P_T of π 's from higher order decays.

The Λ_b channels (7.105)–(7.107) contain charged pions and can potentially be identified while channel (7.108) will be impossible to see. However, if we can identify events from mode (7.107) we can use them with proper normalization subtract the effect of mode (7.108).

To study rejection methods, we generate a sample of the decays which have additional charged pions and apply trigger requirements and the offline cuts detailed in Section 7.5.1.5. In addition, we require that the pions from higher order decays be within a cone in η - ϕ of 0.8 centered on the Λ_c direction. The P_T distribution of these charged pions from higher-order decays is shown in Figure 7.29. Estimating that the minimum P_T which will be reconstructed is 0.3 GeV/c, then approximately 75% of the charged higher order pions will be reconstructed.

In addition to the extra decay pions, we also study tracks coming from primary interaction which might be confused with Λ_b -daughter tracks and cause too many events to be rejected. To model these tracks we generate a Monte Carlo sample using PYTHIA tuned to reflect prompt particle distributions in CDF B events [163]. For events that pass the same trigger and offline requirements as in the trigger study, we compare the impact parameter of the three categories of tracks: Λ_c -daughter tracks, charged pions from higher-order decays and tracks from the primary vertex. The impact-parameter significance (d/σ_d) with respect to the primary vertex and to the Λ_b -decay vertex for the three categories of tracks is shown in Figure 7.30. If we reject events with an additional track associated with the Λ_c -lepton vertex The requirement that the impact parameter significance ($d_0^{\Lambda_b}/\sigma_{d_0}^{\Lambda_b} < 2$), random associations with primary tracks would cause about 10% of the good ($\Lambda_b \rightarrow \Lambda_c, \ell, \nu$) events to be eliminated, but would tag almost 100% of the higher order decays. Thus a small fraction

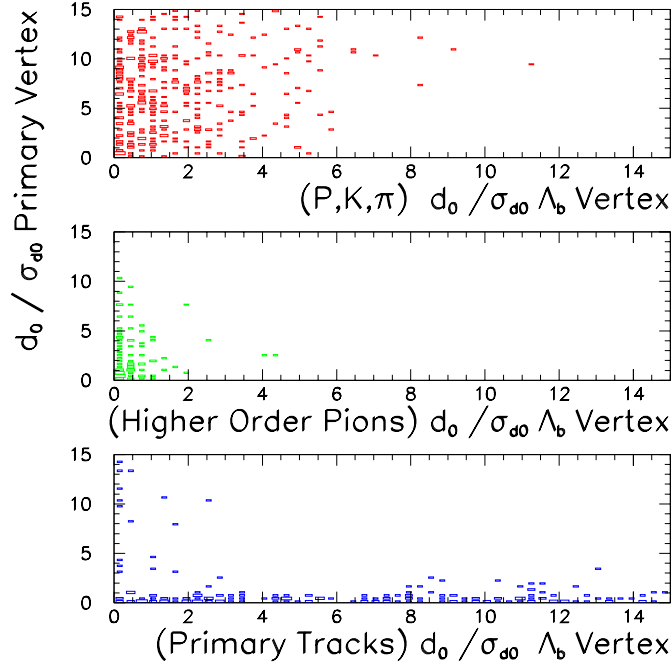


Figure 7.30: Comparison of impact parameter significance of all 3 categories of tracks (protons, kaons and pions) from Λ_c (top plot), higher order pions (middle plot), and tracks from primary vertex (bottom plot) with respect to Λ_b vertex and the Primary Vertex. All tracks must be within a cone of $\Delta R < 0.8$ with $P_T > 0.3$ GeV/c.

of the time real $\Lambda_b \rightarrow \Lambda_c, \ell, \nu$ events will be thrown out but the remaining events will be a relatively pure sample free of higher order Λ_b decays. This coupled with demonstrated ability to calculate the missing neutrino momentum leaves us optimistic about measuring Q^2 in Run II.

7.5.1.7 Summary

We have shown that a lepton + displaced track trigger can produce substantial samples of semileptonic b hadron decays for study and fits well within CDF's overall trigger budget for Run II. We expect ~ 25000 Λ_b decays in 2 fb^{-1} . We have shown that a measurement Q^2 decay in Λ_b decay using the impact parameter information to reject tracks from higher order decays and the primary vertex is feasible. We recognize that fact that further studies are needed to solidify this claim.

7.5.2 Estimating the BTeV Potential for Semileptonic Decays

Using techniques developed for fixed-target charm experiments (including E691 [164], E687 [165], and E791 [166,167]) we demonstrate that BTeV has the necessary capability to extract

information from semileptonic decays. Given the large number of b -hadrons reconstructed by BTeV, the semileptonic reach will be extraordinary.

7.5.2.1 Signal and Background

The signal and background were generated using the MCFast Monte Carlo program. A full description of this program can be found elsewhere [168,169]. MCFast is designed to be a fast and accurate detector simulation with speed and flexibility achieved through parameterization. The MCFast tracing includes the effect of magnetic fields, multiple Coulomb scattering, bremsstrahlung, dE/dx , decays in flight, pair conversions and secondary hadronic interactions. The simulation assumed a luminosity of $2 \times 10^{32} \text{ cm}^{-2} \text{ s}^{-1}$ and included multiple interactions per event. The muon identification code used in this analysis starts by making an acceptance cut. Potential muon tracks must have momentum greater than 5 GeV/ c . All tracks are projected through the three muon stations using the track parameters determined from the Kalman filter. If the projection misses any of the stations the track is thrown out. If the track is associated with a muon particle it is identified as a muon. If the track is not a muon then a misidentification probability is determined and a random number is generated to determine if the particle is misidentified as a muon.

The misidentification probability decreases as the momentum increases and decreases as the radius increases. The misidentification rate varies from 7% for 5 GeV/ c tracks near the beam to 0.2% for 50 GeV/ c tracks at the outer edge of the muon system. The misidentification rate (away from the central region) is loosely based on the measured misidentification rate from the FOCUS experiment. FOCUS is a fixed-target charm experiment which used a ~ 180 GeV photon beam at a rate of approximately 10 MHz. BTeV and FOCUS have similar muon rates and momenta. The BTeV detector has two advantages over the FOCUS muon system. The BTeV detector has much finer granularity and the shielding is magnetized which, by allowing a momentum measurement, provides another handle to distinguish real muons from fakes.

The signal modes analyzed were $B^0 \rightarrow D^{*-}(\bar{D}^0(K^+\pi^-, K^+\pi^-\pi^-\pi^+)\pi^-)\mu^+\nu$ and $\Lambda_b^0 \rightarrow \Lambda_c^-(pK^-\pi^+)\mu^+\nu$. In each case, $\sim 120,000$ events were simulated. Three sources of background were simulated: minimum bias events, charm events, and generic b events (without the signal mode). The cross sections for minimum bias, charm, and b events obtained from Pythia [170] are shown in Table 7.10 along with the predicted numbers of events from one year (10^7 s) of running at a luminosity of $2 \times 10^{32} \text{ cm}^{-2} \text{ s}^{-1}$.

Clearly it is impossible to simulate 10^{14} events given the current state of computing; simulating more than 10^8 events is prohibitive. Therefore we try to estimate the background based on a simulation of 4.2 million minimum bias events, 4.8 million $c\bar{c}$ events, and 1.5 million $b\bar{b}$ events. Given the large number of produced b -hadrons we can certainly make stringent cuts and still retain a large sample of events. Unfortunately, using these stringent cuts eliminates nearly all of our (limited) background which makes it difficult to determine the significance or signal-to-noise ratio of the signal. Since the signals analyzed require detached vertices, reconstructed charm particles, and muons, we assume that the background will be dominated by c and b events, not minimum bias events. Therefore, we

Species	Quark cross section (mb)	Hadron fraction	Branching Ratio	Total produced for 2 fb ⁻¹
Min bias	75	100%	100%	1.5×10^{14}
Charm	0.75	100%	100%	1.5×10^{12}
generic b	0.10	100%	100%	2.0×10^{11}
$B^0 \rightarrow D^* \mu \nu$	0.10	75%	0.35%	5.3×10^8
$\Lambda_b \rightarrow \Lambda_c \mu \nu$	0.10	10%	0.20%	4.0×10^7

Table 7.10: Production cross sections and expected generation rates for signal and background. Cross sections for $b\bar{b}$ production are estimated from D0 data. The minimum bias cross section is taken to be the $p\bar{p}$ total cross section at 2 TeV. The charm cross section is assumed to be 1% of the minimum bias cross section. Branching ratios are from Ref. [171] except $\Lambda_b \rightarrow \Lambda_c \mu \nu$ which is estimated at 4%.

can safely tighten our cuts enough to eliminate all of the minimum bias events which were simulated.

Using these cuts keeps 4 (1) $c\bar{c}$ and 26 (13) $b\bar{b}$ events for the $B^0 \rightarrow D^*(D^0(K\pi, K3\pi)\pi)\mu\nu$ ($\Lambda_b \rightarrow \Lambda_c(pK\pi)\mu\nu$) decay mode. Figure 7.31 shows the result of scaling the signal and background events to an integrated luminosity of 2 fb⁻¹ and distributing the background events evenly through the mass plot. The yield, significance, signal-to-background, and efficiency is tabulated in Table 7.11. These results include a conservative trigger efficiency (50%) which is what is expected from the detached vertex trigger. A detached muon trigger is also planned which will increase the trigger efficiency.

Decay mode	Efficiency	Yield	$S/\sqrt{S+B}$	S/B
$B^0 \rightarrow D^*(D^0(K\pi, K3\pi)\pi)\mu\nu$	0.44%	2,300,000	1,430	21
$\Lambda_b \rightarrow \Lambda_c(pK\pi)\mu\nu$	0.31%	120,000	210	1.0

Table 7.11: Efficiency, expected yields, signal-to-background, and significance for an integrated luminosity of 2 fb⁻¹. Efficiency includes acceptance, trigger efficiency, reconstruction efficiency and cut efficiency. Significance and signal-to-background are calculated by integrating over a $\pm 2\sigma$ region around the mass peak.

7.5.2.2 Semileptonic Reach

To determine the form factors associated with a particular semileptonic decay we would like to have all the kinematic information associated with the decay chain. The most important quantity is q^2 which is the square of the virtual W mass; i.e. the invariant mass of the lepton and neutrino. Reconstructing the momentum vector is not a trivial exercise, however. The technique used to reconstruct the neutrino momentum, pioneered by E691 and used by E687 and E791 among others [164–167], is particularly suited to BTeV as it requires good vertex resolution compared to the vertex separation. The production and decay vertex of the b -hadron gives the b -hadron momentum vector direction. The neutrino momentum perpendicular to the b -hadron momentum vector is easily measured

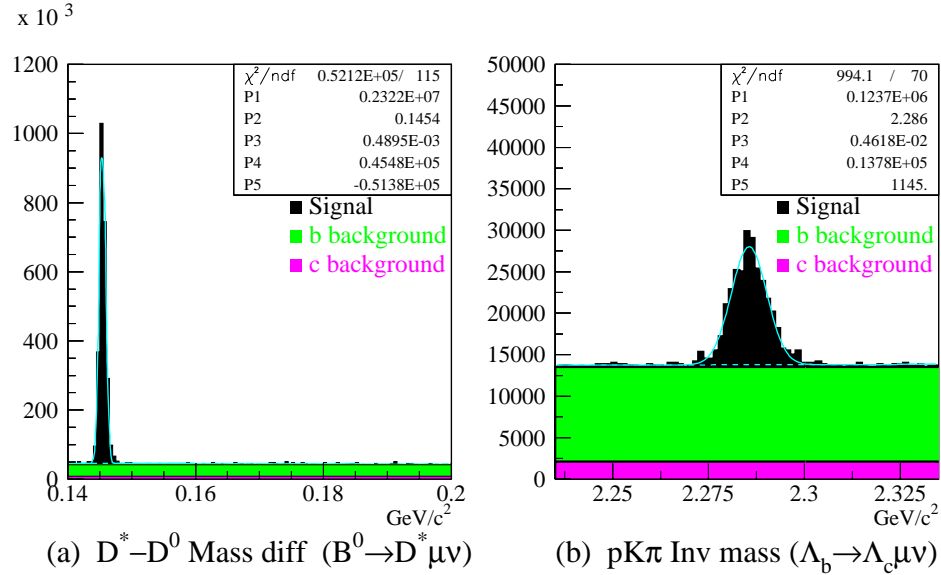


Figure 7.31: (a) $D^* - D^0$ Mass difference distribution for $B^0 \rightarrow D^*(D^0(K\pi, K3\pi)\pi)\mu\nu$ signal events and $b\bar{b}$ and $c\bar{c}$ background events. (b) $pK\pi$ invariant mass distribution for $\Lambda_b \rightarrow \Lambda_c(pK\pi)\mu\nu$ signal events and $b\bar{b}$ and $c\bar{c}$ background events. In both plots, the background events have been spread evenly through the mass range.

because it must balance all of the other decay products. The neutrino momentum parallel to the b -hadron momentum can be determined (up to a quadratic ambiguity) by assuming the invariant mass of the b -hadron. We pick the low momentum solution for the parallel component of the neutrino momentum as Monte Carlo studies indicate this is correct more often.

The most recent published results using this method come from E791 [167]. Using a 500 GeV/c π^- beam, they reconstruct over 6,000 $D^+ \rightarrow \bar{K}^{*0} \ell \nu$ decays. From this sample they obtain form factor measurements of $r_V = V(0)/A_1(0) = 1.87 \pm 0.08 \pm 0.07$ and $r_2 = A_2(0)/A_1(0) = 0.73 \pm 0.06 \pm 0.08$. From the 3,000 muon decays, they also measure $r_3 = A_3(0)/A_1(0) = 0.04 \pm 0.33 \pm 0.29$. Defining the q^2 resolution as the RMS of the generated q^2 minus the reconstructed q^2 divided by q_{max}^2 , E791 had a q^2 resolution of 0.17. From the MCFast simulation with the standard selection criteria and reconstructing the neutrino momentum as described above, BTeV has a q^2 resolution of approximately 0.14 as shown in Fig. 7.32. With 6,000 events, the E791 results give smaller errors than most lattice QCD calculations. With a similar q^2 resolution and 100 times more data, BTeV will also be able to challenge theoretical predictions or provide values which can be input into other calculations.

One additional difficulty in extracting information from these semileptonic decays comes from b semileptonic decays into charm excited states which decay into the state being investigated. For example, in the decay $\Lambda_b^0 \rightarrow \Sigma_c^+ \mu \nu$, the Σ_c^+ can decay to $\Lambda_c^+ \pi^0$. Assuming the π^0 is lost, this event will be reconstructed as a signal $\Lambda_b^0 \rightarrow \Lambda_c^+ \mu \nu$ event and the neutrino reconstruction (which assumes the invariant mass of the $\Lambda_c^+ \mu \nu$ is equal to the Λ_b^0) will be

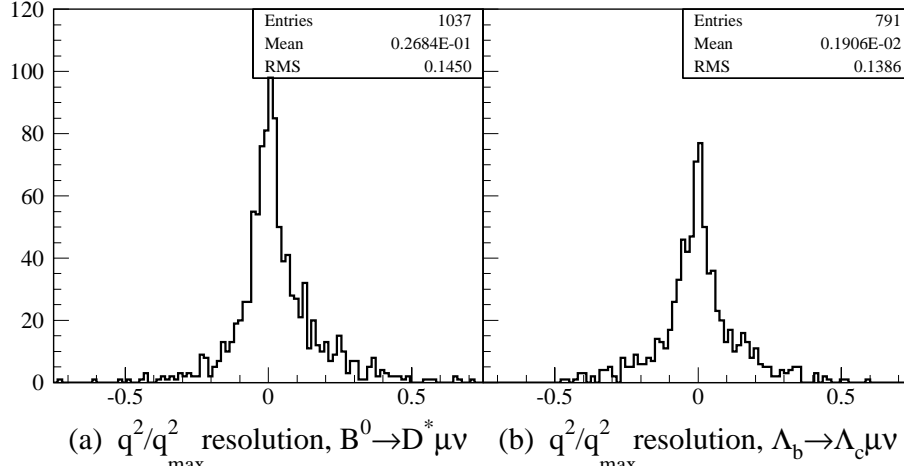


Figure 7.32: q^2/q^2_{\max} resolution for (a) $B^0 \rightarrow D^*(D^0(Kn\pi)\pi)\mu\nu$ and (b) $\Lambda_b \rightarrow \Lambda_c(pK\pi)\mu\nu$.

inaccurate. The q^2 resolution for these events is shown in Fig. 7.33a. Assuming an equal mixture of $\Lambda_b \rightarrow \Lambda_c$ and $\Lambda_b \rightarrow \Sigma_c$ decays gives the q^2 resolution shown in Fig. 7.33b. This shows a resolution only slightly degraded (0.14 to 0.15) but with a bias equal to 1/3 of the RMS. BTeV has excellent π^0 reconstruction capabilities [169] which should make it possible to measure the relative branching ratios and correct for this bias.

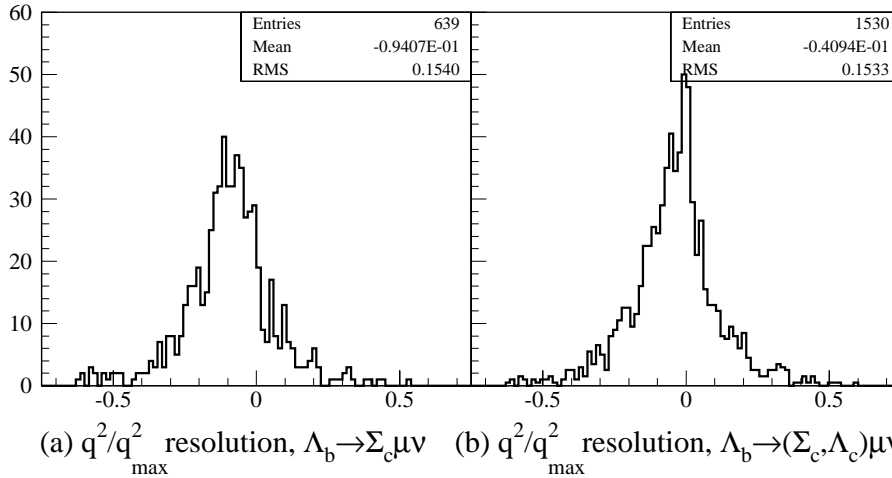


Figure 7.33: q^2/q^2_{\max} resolution for (a) $\Lambda_b \rightarrow \Lambda_c(pK\pi)\mu\nu$ where the Λ_c comes from a Σ_c and (b) $\Lambda_b \rightarrow \Lambda_c(pK\pi)\mu\nu$ where half of the Λ_c 's come from Σ_c 's and half come directly from Λ_b 's.

Since BTeV has a very efficient vertex trigger at Level 1, the semieleptonic decays can also be studied. Even though the acceptance of the ECAL is much smaller than that of the muon detectors we expect significant numbers of reconstructed decays in the electronic modes which can be used for systematic studies as well as just increasing the statistics.

7.5.2.3 Summary

This study only provides a cursory look at some of the semileptonic physics available with BTeV. There are many other semileptonic decay modes of b -hadrons which are well within the grasp of BTeV. These decay modes include $B \rightarrow \rho \ell \nu$ to determine V_{ub} and B_s semileptonic decay modes to check SU(3). In addition, BTeV will have many semileptonic charm decays available for study.

7.6 Summary of Semileptonic Decays

The study of exclusive semileptonic decays complements the studies on CP violation and mixing discussed in Chapters 6 and 8, since semileptonic decays can, in principle, provide determinations of CKM elements such as $|V_{ub}|$ and $|V_{cb}|$.

For any useful comparison between theory and experiment, we need experimental measurements of q^2 (and other) distributions. This is a challenging task especially in a hadron collider environment, because it requires the reconstruction of the neutrino momentum. Studies at both, CDF and BTeV, have established the feasibility of neutrino momentum reconstruction and subsequent measurement of q^2 distributions with good resolution.

The decay $\Lambda_b \rightarrow \Lambda_c \ell \bar{\nu}$ is of particular interest. It can only be studied at hadron colliders and provides information on the parameters of the heavy quark expansion at sub-leading order.

Tevatron experiments should explore the full range of semileptonic decays, including B and B_s meson decays to light hadrons. It is important to have measurements of many different semileptonic heavy-to-light decays, with as high an accuracy as possible, for two reasons. First, these measurements can provide tests of heavy flavor and SU(3) symmetry relations. Second, we should expect significant improvements in theoretical predictions of exclusive heavy-to-light form factors, based for example, on lattice QCD, in the time frame for Run II, and certainly by the time BTeV comes on line. These measurements will help to establish the reliability of lattice QCD calculations, and of the corresponding determinations of CKM elements, such as $|V_{ub}|$, from them.

References

- [1] G. Buchalla, A.J. Buras, and M.E. Lautenbacher, *Rev. Mod. Phys.* **68**, 1125 (1996).
- [2] A.J. Buras *et.al.*, *Nucl. Phys.* **B424**, 374 (1994); A.J. Buras and M. Münz, *Phys. Rev.* **D52**, 186 (1995); M. Misiak, *Nucl. Phys.* **B393**, 3 (1993); **Erratum**, *Nucl. Phys.* **B439**, 461 (1995).
- [3] G. Buchalla, G. Hiller and G. Isidori, *Phys. Rev.* **D63**, 014015 (2001).
- [4] M. Voloshin and M. Shifman, *Sov. J. Nucl. Phys.* **41**, 120 (1985); J. Chay, H. Georgi and B. Grinstein, *Phys. Lett.* **B247**, 399 (1990); A.V. Manohar and M.B. Wise, *Phys. Rev.* **D49**, 1310 (1994); T. Mannel, *Nucl. Phys.* **B413**, 396 (1994); I.I. Bigi, N.G. Uraltsev and A.I. Vainshtein, *Phys. Lett.* **B293**, 430 (1992); I.I. Bigi, M. Shifman, N.G. Uraltsev and A.I. Vainshtein, *Phys. Rev. Lett.* **71**, 496 (1993); B. Blok, L. Koyrakh, M. Shifman and A.I. Vainshtein, *Phys. Rev.* **D49**, 3356 (1994); **Erratum**, *Phys. Rev.* **D50**, 3572 (1994); A. Falk, M. Luke, and M.J. Savage, *Phys. Rev.* **D49**, 337 (1994).
- [5] M. A. Shifman, proceedings of the workshop on Continuous Advances in QCD, Minneapolis 1994 (held in Minneapolis, MN, 18-20 Feb 1994), p. 249, [hep-ph/9405246](#).
- [6] N. Isgur, [hep-ph/9809279](#).
- [7] T. Inami and C.S. Lim, *Prog. Theor. Phys.* **65**, 29 (1981).
- [8] R. D. Dikeman, M. Shifman and N. G. Uraltsev, *Int. J. Mod. Phys.* **A11**, 571 (1996). C. Bauer, *Phys. Rev.* **57**, 5611 (1998) [**Erratum-ibid.** **D60**, 099907 (1998)]; A. L. Kagan and M. Neubert, *Eur. Phys. J. C* **7**, 5 (1999).
- [9] M. Misiak and M. Münz, *Phys. Lett.* **B344**, 308 (1995); K. Chetyrkin, M. Misiak and M. Münz, *Phys. Lett.* **B400**, 206 (1997) [**Erratum-ibid.** **B425** (1997) 414].
- [10] K. Adel and Y.-P. Yao, *Phys. Rev.* **D49**, 4945 (1994); C. Greub and T. Hurth, *Phys. Rev.* **D56**, 2934 (1997).
- [11] A. Ali and C. Greub, *Z. Phys.* **C49**, 431 (1991); *Phys. Lett.* **B259**, 182 (1991); *Phys. Lett.* **B361**, 46 (1995); N. Pott, *Phys. Rev.* **D54**, 938 (1996).
- [12] C. Greub, T. Hurth, and D. Wyler, *Phys. Lett.* **B380**, 385 (1996); *Phys. Rev.* **D54**, 3350 (1996).
- [13] M. B. Voloshin, *Phys. Lett.* **B397**, 275 (1997); A. K. Grant, A. G. Morgan, S. Nussinov and R. D. Peccei, *Phys. Rev.* **D56**, 3151 (1997); Z. Ligeti, L. Randall and M. B. Wise, *Phys. Lett.* **B402**, 178 (1997);
- [14] A. Czarnecki and W. Marciano, *Phys. Rev. Lett.* **81**, 277 (1998); P. Gambino and U. Haisch, *JHEP* 0009 (2000) 001; P. Gambino and U. Haisch, *JHEP* 0110 (2000) 020.
- [15] P. Gambino and M. Misiak, *Nucl. Phys.* **B611**, 338 (2001).

- [16] CLEO Collaboration, T.E. Coan *et al.*, *Phys. Rev. Lett.* **84**, 5283 (2000); CLEO Collaboration, S. Ahmed *et al.*, [hep-ex/9908022](#); ALEPH Collaboration, R. Barate *et al.*, *Phys. Lett.* **B429**, 169 (1998); CLEO Collaboration, M.S. Alam *et al.*, *Phys. Rev. Lett.* **74**, 2885 (1995); CLEO Collaboration, R. Amar *et al.*, *Phys. Rev. Lett.* **71**, 674 (1993).
- [17] A Kagan and M. Neubert, *Eur. Phys. J.* **C7**, 5 (1999); A.K. Leibovich, I.Z. Rothstein, *Phys. Rev.* **D61**, 074006 (2000).
- [18] C.W. Bauer, S. Fleming, and M. Luke, *Phys. Rev.* **D63**, 014006 (2001);
- [19] A. Kapustin and Z. Ligeti, *Phys. Lett.* **B55**, 318 (1995); C. Bauer, *Phys. Rev.* **D57**, 5611 (1998), E: **D60**, 099907 (1999).
- [20] A. Ali and C. Greub, *Phys. Lett.* **B287**, 191 (1992); G. Ricciardi, *Phys. Lett.* **B355**, 313 (1995).
- [21] A. Ali, G. Giudice and T. Mannel, *Z. Phys.* **C67**, 417 (1995); P. Cho, M. Misiak and D. Wyler, *Phys. Rev.* **D54**, 3329 (1996); T. Goto *et al.*, *Phys. Rev.* **D55**, 4273 (1997); G. Buchalla and G. Isidori, *Nucl. Phys.* **B525**, 333 (1998).
- [22] C. Huang, W. Liao, and Q. Yan, *Phys. Rev.* **D59**, 011701 (1999); J. Hewett and J. D. Wells, *Phys. Rev.* **D55**, 5549 (1997); E. Lunghi, A. Masiero, I. Scimemi, and L. Silvestrini, *Nucl. Phys.* **B568**, 120 (2000).
- [23] A.J. Buras and M.Münz, *Phys. Rev.* **D52**, 186 (1985).
- [24] Y. Nir, *Phys. Lett.* **221**, 184 (1989).
- [25] A. Ali, G. Hiller, L. T. Handoko and T. Morozumi, *Phys. Rev.* **D55**, 4105 (1997); A. Ali and G. Hiller, *Phys. Rev.* **D58**, 074001 (1998).
- [26] C. W. Bauer and C. N. Burrell, *Phys. Lett.* **B469**, 248 (1999), *Phys. Rev.* **D62**, 114028 (2000).
- [27] A. El-Khadra, A. Kronfeld, P. Mackenzie, S. Ryan, J. Simone, *Phys. Rev.* **D64**, 014502 (2001); S. Aoki *et al.*, *Nucl. Phys. B (Proc. Suppl.)* **94**, 329 (2001).
- [28] S. Collins *et al.*, *Phys. Rev.* **D64**, 055002 (2001).
- [29] N. Isgur and M. B. Wise, *Phys. Rev.* **D42**, 2388 (1990).
- [30] N. Isgur and M. B. Wise, *Phys. Lett.* **B232**, 113 (1989); *Phys. Lett.* **B237**, 527 (1990).
- [31] G. Burdman and J. F. Donoghue, *Phys. Lett.* **B270**, 55 (1991).
- [32] H. Politzer and M. B. Wise, *Phys. Lett.* **B206**, 681 (1988).
- [33] G. Burdman, Z. Ligeti, M. Neubert and Y. Nir, *Phys. Rev.* **D49**, 2331 (1994).
- [34] Z. Ligeti and M. B. Wise, *Phys. Rev.* **60**, 117506 (1999).

- [35] Z. Ligeti, I.W. Stewart and M.B. Wise, *Phys. Lett.* **B420**, 1998 (359).
- [36] M. Dugan and B. Grinstein, *Phys. Lett.* **B255**, 583 (1991).
- [37] J. Charles *et al.*, *Phys. Rev.* **D60**, 014001 (1999).
- [38] G. Burdman, *Phys. Rev.* **D57**, 4254 (1998).
- [39] U. Aglietti and G. Corbo, *Int. J. Mod. Phys.* **A15**, 363 (2000).
- [40] M. Beneke and T. Feldmann, *Nucl. Phys.* **B592**, 3 (2001).
- [41] C. W. Bauer, S. Fleming, D. Pirjol and I. W. Stewart, *Phys. Rev.* **D63**, 114020 (2001).
- [42] A. Ali, P. Ball, L. Handoko, and G. Hiller, *Phys. Rev.* **D61**, 074024 (2000).
- [43] G. Burdman and G. Hiller, *Phys. Rev.* **D63**, 113008 (2001).
- [44] M. Beneke, T. Feldmann and D. Seidel, [hep-ph/0106067](#).
- [45] S. W. Bosch and G. Buchalla, [hep-ph/0106081](#).
- [46] M. Bauer, B. Stech and M. Wirbel, *Z. Phys.* **C29**, 637 (1985).
- [47] J. G. Körner and G. A. Schuler, *Z. Phys.* **C38**, 511 (1987).
- [48] P. Ball and V. M. Braun, *Phys. Rev.* **D55**, 5561 (1997).
- [49] D. Melikhov, N. Nikitin and S. Simula, *Phys. Lett.* **B410**, 210 (1997).
- [50] N. Isgur and N. Scora, *Phys. Rev.* **52**, 2783 (1995).
- [51] D. Melikhov and B. Stech, *Phys. Rev.* **62**, 014006 (2000).
- [52] B. Stech, *Phys. Lett.* **B354**, 447 (1995).
- [53] J. M. Soares, *Phys. Rev.* **D54**, 6837 (1996).
- [54] G. Burdman and J. Kambor, *Phys. Rev.* **D55**, 2817 (1997); G. Burdman, proceedings of the International Conference on B Physics and CP Violation (Honolulu, Hawaii, 24-28 Mar 1997), p.402, [hep-ph/9707410](#).
- [55] C. G. Boyd, B. Grinstein and R. Lebed, *Phys. Rev. Lett.* **74**, 4603 (1995); *Nucl. Phys.* **B461**, 493 (1996); *Phys. Rev.* **D56**, 6895 (1997); C. G. Boyd and R. Lebed, *Nucl. Phys.* **B485**, 275 (1997); L. Lellouch, *Nucl. Phys.* **B479**, 353 (1996).
- [56] C. Caso *et.al.* (PDG Collaboration), *Eur. Phys. J.* **C3**(1998)1.
- [57] F. Krüger and L.M. Sehgal, *Phys. Lett.* **B380**, 199 (1996).
- [58] A. Ali, T. Mannel and T. Morozumi, *Phys. Lett.* **B273**, 505 (1991).
- [59] A. Ali and G. Hiller, *Phys. Rev.* **D60**, 034017 (1999).

- [60] K. Abe *et al.* [Belle Collaboration], [hep-ex/0107072](#).
- [61] K. Abe *et al.* [BELLE Collaboration], [hep-ex/0109026](#).
- [62] B. Aubert *et al.* [BABAR Collaboration], [hep-ex/0107026](#).
- [63] S. Anderson *et al.* (CLEO Collaboration), CLNS 01/1739, [hep-ex/0106060](#).
- [64] S. Glenn *et al.* (CLEO Collaboration), *Phys. Rev. Lett.* **80**, 2289 (1998).
- [65] G. Burdman, *Phys. Rev.* **52**, 6400 (1995).
- [66] A. Ali and G. Hiller, *Eur. Phys. J.* **C8**, 619 (1999).
- [67] F. Krüger and L.M. Sehgal, *Phys. Rev.* **D55**, 2799 (1997).
- [68] C. Greub, H. Simma and D. Wyler, *Nucl. Phys.* **B434**, 39 (1995); A. L. Kagan and M. Neubert, *Phys. Rev.* **D58**, 094012 (1998).
- [69] F. Krüger and J.C. Romão, *Phys. Rev.* **D62**, 034020 (2000).
- [70] E. Lunghi and I. Scimemi, *Nucl. Phys.* **B574**, 43 (2000).
- [71] M.S. Alam *et al.* (CLEO Collaboration), *Phys. Rev. Lett.* 74(1995)2885;
S. Ahmed *et al.* (CLEO Collaboration), CLEO CONF 99–10 ([hep-ex/9908022](#)).
- [72] A. Ali, V.M. Braun, and H. Simma, *Z. Phys.* **C63**, 437 (1994); L. Del Debbio *et al.*, *Phys. Lett.* **B416**, 392 (1998); S. Narison, *Phys. Lett.* **B327**, 354 (1994); P. Ball and V.M. Braun, *Phys. Rev.* **D58**, 094016 (1998); C. Bernard, P. Hsieh, and A. Soni, *Phys. Rev. Lett.* **72**, 1402 (1994); K. C. Bowler *et al.*, *Phys. Rev.* **D51**, 4955 (1995).
- [73] S. Veseli, M.G. Olsson, *Phys. Lett.* **B367**, 309 (1996); A. Ali, T. Ohl, and T. Mannel, *Phys. Lett.* **B298**, 195 (1993); T. Altomari, *Phys. Rev.* **D37**, 677 (1988).
- [74] E. Golowich and S. Pakvasa, *Phys. Rev.* **D51**, 1215 (1995); N.G. Deshpande, X.-G. He, and J. Trampetic, *Phys. Lett.* **B367**, 362 (1996).
- [75] B. Grinstein and D. Pirjol, *Phys. Rev.* **D62**, 093002 (2000).
- [76] D. Atwood, B. Blok, and A. Soni, *Int. J. Mod. Phys.* **A11**, 3743 (1996); J.F. Donoghue, E. Golowich, and A.A. Petrov, *Phys. Rev.* **D55**, 2657 (1997).
- [77] T. Mannel and S. Recksiegel, *J. Phys.* **G24**, 979 (1998).
- [78] G. Hiller and A. Kagan, [hep-ph/0108074](#).
- [79] T. Inami and C. S. Lim, *Prog. Theor. Phys.* **65**, 297 (1981) [Erratum **65**, 1772 (1981)].
- [80] B. Grzadkowski and P. Krawczyk, *Z. Phys.* **C18**, 43 (1983).
- [81] P. Krawczyk, *Z. Phys.* **C44**, 509 (1989).
- [82] G. Buchalla, A. J. Buras and M. Lautenbacher, *Rev. Mod. Phys.* **68**, 1125 (1996).

- [83] G. Buchalla and A. J. Buras, *Nucl. Phys.* **B398**, 285 (1993); *Nucl. Phys.* **B400**, 225 (1993);
- [84] M. Misiak and J. Urban, *Phys. Lett.* **B451**, 161 (1999).
- [85] E. Jenkins and M. J. Savage, *Phys. Lett.* **B281**, 331 (1992).
- [86] D. Groom *et al.*, *Eur. Phys. J.* **C15**, 1 (2000.)
- [87] A. Ali Khan *et al.* [CP-PACS Collaboration], *Phys. Rev.* **D64**, 034505 (2001).
- [88] S. Glenn *et al.* (CLEO Collaboration), *Phys. Rev. Lett.* **80**, 2289 (1998); B. Abbott *et al.* (DØ Collaboration), *Phys. Lett.* **B223**, 419 (1998); C. Albajar *et al.* (UA1 Collaboration), *Phys. Lett.* **B262**, 163 (1991). Also, a recent search in exclusive channels: T. Affolder *et al.* (CDF Collaboration), *Phys. Rev. Lett.* **83**, 3378 (1999).
- [89] S. Bertolini *et al.*, *Nucl. Phys.* **B353**, 591 (1991).
- [90] P. Cho, M. Misiak and D. Wyler, *Phys. Rev.* **D54**, 3329 (1996).
- [91] J.L. Hewett and J.D. Wells, *Phys. Rev.* **D55**, 5549 (1997).
- [92] T. Goto *et al.*, *Phys. Rev.* **D55**, 4272 (1997); T. Goto, Y. Okada and Y. Shimizu, *Phys. Rev.* **D58**, 094006 (1998).
- [93] M. Ciuchini *et al.*, *Nucl. Phys.* **B534**, 3 (1998).
- [94] E. Lunghi, A. Masiero, I. Scimemi and L. Silvestrini, *Nucl. Phys.* **B568**, 120 (2000).
- [95] Oscar Vives and Antonio Masiero, Lectures given by A. Masiero at the International School on Subnuclear Physics (Erice, Italy, 29 August–7 September 1999) hep-ph/0003133.
- [96] A. Masiero and H. Murayama, *Phys. Rev.* **83**, 907 (1999).
- [97] A. J. Buras and R. Buras, *Phys. Lett.* **B501**, 223 (2001); M. Dine, E. Kramer, Y. Nir and Y. Shadmi, *Phys. Rev.* **D64**, 116005 (2001).
- [98] C.-S. Huang, W. Liao, Q.-S. Yan and S.-H. Zhu, *Phys. Rev.* **D63**, 114021 (2001)[Erratum-*ibid.* **D64**, 059902 (2001)]; C.-S. Huang and Q.-S. Yan, *Phys. Lett.* **B442**, 209 (1998); C.-S. Huang, W. Liao and Q.-S. Yan, *Phys. Rev.* **D59**, 011701 (1999); C. Hamzaoui, M. Pospelov and M. Toharia, *Phys. Rev.* **D59**, 095005 (1999); K. S. Babu and C. Kolda, *Phys. Rev. Lett.* **84**, 228 (2000); P. H. Chankowski and L. Slawianowska, *Phys. Rev.* **D63**, 054012 (2001); A. Dedes, H.K. Dreiner, U. Nierste, *Phys. Rev. Lett.* **87**, 251804 (2001).
- [99] K. Hagiwara, K. Hikasa, R. D. Peccei and D. Zeppenfeld, *Nucl. Phys.* **B282**, 253 (1997).
- [100] *A Combination of Preliminary Measurements of Triple Gauge Boson Coupling Parameters measured by the LEP Experiments*, the LEP electroweak working group, LEPEWWG/TGC/2000-01.

- [101] F. Abe *et al.*, the CDF collaboration, *Phys. Rev. Lett.* **78**, 4536 (1997); S. Abachi *et al.*, the D0 collaboration, *Phys. Rev. Lett.* **78**, 3634 (1997); B. Abbott *et al.*, the D0 collaboration, contributed to the XVIII International Symposium on Lepton-Photon Interactions, Hamburg, Germany, July 28 - August 1, 1997.
- [102] S. Chia, *Phys. Lett.* **B240**, 465 (1990).
- [103] K. Numata, *Z. Phys.* **C52**, 691 (1991).
- [104] T. Rizzo, *Phys. Lett.* **B315**, 571 (1993).
- [105] X.-G. He and B. McKellar, *Phys. Lett.* **B320**, 168 (1994).
- [106] X.-G. He, *Phys. Lett.* **B319**, 327 (1993).
- [107] G. Baillie, *Z. Phys.* **C61**, 667 (1994).
- [108] G. Burdman, *Phys. Rev.* **D59**, 035001 (1998).
- [109] X.-G. He, *Phys. Lett.* **B460**, 405 (1999).
- [110] R. D. Peccei and X. Zhang, *Nucl. Phys.* **B337**, 269 (1990); R. D. Peccei, S. Peris, and X. Zhang, *Nucl. Phys.* **B349**, 305 (1991).
- [111] E. Malkawi and C.-P. Yuan, *Phys. Rev.* **D50**, 4462 (1994).
- [112] K. Fujikawa and A. Yamada, *Phys. Rev.* **D49**, 5890 (1994); F. Larios, M. A. Pérez, and C.-P. Yuan, *Phys. Lett.* **B457**, 334 (1999).
- [113] O. J. P. Éboli, M. C. Gonzalez-García, and S. F. Novaes, *Phys. Lett.* **B415**, 75 (1997).
- [114] G. Burdman, M. C. Gonzalez-García, and S. F. Novaes, *Phys. Rev.* **D61**, 114016 (2000).
- [115] C. T. Hill, *Phys. Lett.* **B345**, 483 (1995); K. Lane and E. Eichten, *Phys. Lett.* **B352**, 382 (1995); K. Lane, *Phys. Rev.* **D54**, 2204 (1996).
- [116] S. Glashow and S. Weinberg, *Phys. Rev.* **D15**, 1958 (1977).
- [117] W. S. Hou, *Phys. Lett.* **B296**, 179 (1992); D. Chang, W. S. Hou and W. Y. Keung, *Phys. Rev.* **D48**, 217 (1993).
- [118] W. S. Hou and R. S. Willey, *Phys. Lett.* **B202**, 591 (1988); B. Grinstein, M. J. Savage and M. B. Wise, *Nucl. Phys.* **B319**, 271 (1989); T. M. Aliev, M. Savci and A. Ozpineci, *Phys. Lett.* **B410**, 216 (1997).
- [119] D. Atwood, L. Reina and A. Soni, *Phys. Rev.* **D55**, 3156 (1997); T. M. Aliev and I. O. Iltan, *Phys. Lett.* **B451**, 175 (1999).

- [120] M. J. Savage, *Phys. Lett.* **B266**, 135 (1991); W. Skiba and J. Kalinowski, *Nucl. Phys.* **B404**, 3 (1993); Y.-B. Dai, C.-S. Huang and H.-W. Huang, *Phys. Lett.* **B390**, 257 (1997); H. E. Logan and U. Nierste, *Nucl. Phys.* **B586**, 39 (2000); C.-S. Huang, W. Liao, Q.-S. Yan and S.-H. Zhu, *Phys. Rev.* **D63**, 114021 (2001), [Erratum-ibid **D64** 059902 (2001)] ; C. Bobeth *et al.*, *Phys. Rev.* **D64**, 074014 (2001).
- [121] A. Longhitano, *Phys. Rev.* **D22**, 1166 (1980); A. Longhitano, *Nucl. Phys.* **B188**, 118 (1981). For a more recent presentation see T. Appellequist and G. Wu, *Phys. Rev.* **D48**, 3235 (1993).
- [122] J. Bernabéu, D. Comelli, A. Pich and A. Santamaria, *Phys. Rev. Lett.* **78**, 2902 (1997).
- [123] G. Burdman, *Phys. Lett.* **B409**, 442 (1997).
- [124] B. Balaji, *Phys. Rev.* **D52**, 1699 (1996).
- [125] D. Kominis, *Phys. Lett.* **B358**, 312 (1995); G. Buchalla, G. Burdman, C. T. Hill and D. Kominis, *Phys. Rev.* **D53**, 5185 (1996).
- [126] “The CDF II Detector Technical Design Report”, CDF collaboration, FERMILAB-Pub-96/390-E (1996).
- [127] CLEO Collaboration, M.S. Alam *et al*, *Phys. Rev. Lett.* **74**, 2885, (1995).
- [128] CLEO Collaboration, S. Glenn *et al*, *Phys. Rev. Lett.* **80**, 2289 (1998).
- [129] B. Abbott *et al.*, D0 Collaboration, *Phys. Lett.* **B423**, 419 (1998).
- [130] O. Baer and N. Pott, *Phys. Rev.* **D 55**, 1684 (1997).
- [131] M. Mangano, P. Nason and G. Ridolfi, *Nucl. Phys.* **B373**, 295 (1992).
- [132] F. Abe *et al.*, CDF Collaboration, *Phys. Rev. Lett.*, **76**, 4675 (1996).
- [133] F. Abe *et al.*, CDF Collaboration, *Phys. Rev. Lett.*, **79**, 572 and 578 (1997).
- [134] *Triggers for B Physics Studies in Run II*, F. Stichelbaut, M. Narain and A. Ziemiński, D0 note 3354 (December 1997).
- [135] K. Kordas, *et al.* CDF Note 3771.
- [136] A. B. Wicklund, CDF Note 4354.
- [137] M. Tanaka, *et al.* CDF Note 4804.
- [138] T. Affolder *et al.* [CDF Collaboration], *Phys. Rev. Lett.* **84**, 1663 (2000).
- [139] M. Tanaka, *et al.* CDF Note 5125.
- [140] T. Affolder *et al.* [CDF Collaboration], *Phys. Rev. Lett.* **83**, 3378 (1999); W. Erdmann, *et al.* CDF Note 4517.
- [141] C. Greub, A. Ioannisian and D. Wyler, *Phys. Lett.* **B346**, 149 (1995).

- [142] A. V. Manohar and M. B. Wise, “Heavy quark physics,” *Cambridge Monographs on Particle Physics, Nuclear Physics, and Cosmology, Vol. 10*.
- [143] A. Czarnecki, *Phys. Rev. Lett.* **76**, 4124 (1996); A. Czarnecki and K. Melnikov, *Nucl. Phys.* **B505**, 65 (1997).
- [144] P. F. Harrison and H. R. Quinn [BABAR Collaboration], “The BaBar physics book: Physics at an asymmetric B factory,” SLAC-R-0504 *Papers from Workshop on Physics at an Asymmetric B Factory (BaBar Collaboration Meeting), Rome, Italy, 11-14 Nov 1996, Princeton, NJ, 17-20 Mar 1997, Orsay, France, 16-19 Jun 1997 and Pasadena, CA, 22-24 Sep 1997*.
- [145] C. Bernard, Y. Shen and A. Soni, *Phys. Lett.* **B317**, 164 (1993); UKQCD Collaboration (K.C. Bowler *et al.*), *Phys. Rev.* **D52**, 5067 (1995); T. Bhattacharya and R. Gupta, *Nucl. Phys. B* (Proc. Suppl.)**42**, 935 (1995); *Nucl. Phys. B* (Proc. Suppl.)**47**, 481 (1996); J. Mandula and M.C. Ogilvie, *Nucl. Phys. B* (Proc. Suppl.)**34**, 480 (1994); T. Draper and C. McNeile, *Nucl. Phys. B* (Proc. Suppl.)**47**, 429 (1996); C. Bernard *et al.*, *Nucl. Phys. B* (Proc. Suppl.)**63**, 374 (1998); J. Christensen, T. Draper and C. McNeile, *Nucl. Phys. B* (Proc. Suppl.)**63**, 377 (1998); S. Hashimoto and H. Matsu-furu, *Phys. Rev.* **D54**, 4578 (1996.)
- [146] S. Hashimoto, *et al.*, *Phys. Rev.* **D61**, 014502 (2000); J. Simone, *et al.*, *Nucl. Phys. B* (Proc. Suppl.)**83**, 334 (2000), hep-lat/9910026; S. Hashimoto, *et al.*, Fermilab-PUB-01-317-T, hep-ph/01110253.
- [147] A. Kronfeld, *Phys. Rev.* **D62**, 014505 (2000).
- [148] H. Georgi, B. Grinstein and M. B. Wise, *Phys. Lett.* **B252**, 456 (1990).
- [149] J. G. Korner and M. Kramer, *Phys. Lett.* **B275**, 495 (1992).
- [150] M. B. Voloshin, *Int. J. Mod. Phys. A*10 (1995) 2865; A. A. Penin and A. A. Pivovarov, *Phys. Lett.* **B435**, 413 (1998); K. Melnikov and A. Yelkhovsky, *Phys. Rev.* **D59**, 114009 (1999); A. H. Hoang, *Phys. Rev.* **D61**, 034005 (2000); M. Beneke and A. Signer, *Phys. Lett.* **B471**, 233 (1999); A. H. Hoang, hep-ph/0008102.
- [151] Z. Ligeti, M. Luke, A.V. Manohar and M.B. Wise, *Phys. Rev.* **D60**, 034019 (1999); A. Kapustin and Z. Ligeti, *Phys. Lett.* **B355**, 318 (1995); M.B. Voloshin, *Phys. Rev.* **D51** (1995) 4934; A. F. Falk, M. Luke and M. J. Savage, *Phys. Rev.* **D53**, 6316 (1996); *Phys. Rev.* **D53**, 2491 (1996).
- [152] V. Gimenez, *et al.*, *JHEP* 0003 (2000) 018; S. Collins, hep-lat/0009040.
- [153] A. K. Leibovich and I. W. Stewart, *Phys. Rev.* **D57**, 5620 (1998).
- [154] A. Falk, Z. Ligeti, M. Wise, *Phys. Lett.* **B406**, 225 (1997).
- [155] C. Bauer, Z. Ligeti, M. Luke, *Phys. Lett.* **B479**, 395 (2000).
- [156] T. Miao, “Measurement of Λ_b Lifetime From $\Lambda_b \rightarrow \Lambda_c \ell \nu$ ”, CDF Note 3395 (1995).

- [157] C. Peterson *et al.*, Phys. Rev. **D 27**, 105 (1983); J. Chrin, A. Phys **C 36**, 163 (1987).
- [158] P. Avery, K. Read and G. Trahern, “QQ: A Monte Carlo Generator”, CLEO Internal Software Note CSN-212, Cornell University, 1985.
- [159] W. Taylor *et al.*, “Run 1B Level 2 CEM_8_CFT_7.5 and XCES Electron Trigger Efficiencies”, CDF Note 4691 (1998).
- [160] J. Done *et al.*, “Study of Level 2 Inclusive Muon Trigger Efficiency in Run 1B”, CDF Note 4017 (1999).
- [161] The CDF Collaboration “Update to Proposal P-909: Physics Performance of the CDF II Detector with An Inner Silicon Layer and A Time of Flight Detector”, (1999).
- [162] M. Tanaka “ B_s Mixing with Semileptonic Decays in Run II”, CDF Note 5290 (2000).
- [163] D. Vučinić, P. Sphicas, P. Maksimović, “Observation of B(2P) States in Semileptonic B Decays”, CDF Note 3852 (1998).
- [164] E691 Collaboration, J.C. Anjos *et al.*, Phys. Rev. Lett. **440**, 435 (1990).
- [165] E687 Collaboration, P.L. Frabetti *et al.*, Phys. Lett. **B307**, 262 (1993).
- [166] E791 Collaboration, E.M. Aitala *et al.*, Phys. Rev. Lett. **80**, 1393 (1998).
- [167] E791 Collaboration, E.M. Aitala *et al.*, Phys. Lett. **B440**, 435 (1998).
- [168] MCFast description: <http://www-pat.fnal.gov/mcfast.html>.
- [169] BTeV proposal:
http://www-btev.fnal.gov/public_documents/btev_proposal/index.html.
- [170] T. Sjöstrand, Computer Physics Commun. **82** (1994) 74.
- [171] Particle Data Group, D.E. Groom *et al.*, Eur. Phys. J. **C15**, 1 (2000).